

High Contrast Grating for Optical Sensing

*Tianbo Sun
Constance Chang-Hasnain, Ed.*



Electrical Engineering and Computer Sciences
University of California at Berkeley

Technical Report No. UCB/EECS-2017-170

<http://www2.eecs.berkeley.edu/Pubs/TechRpts/2017/EECS-2017-170.html>

December 1, 2017

Copyright © 2017, by the author(s).
All rights reserved.

Permission to make digital or hard copies of all or part of this work for personal or classroom use is granted without fee provided that copies are not made or distributed for profit or commercial advantage and that copies bear this notice and the full citation on the first page. To copy otherwise, to republish, to post on servers or to redistribute to lists, requires prior specific permission.

High Contrast Grating for Optical Sensing

By

Tianbo Sun

A dissertation submitted in partial satisfaction of the

requirements for the degree of

Doctor of Philosophy

in

Engineering – Electrical Engineering and Computer Sciences

in the

Graduate Division

of the

University of California, Berkeley

Committee in charge:

Professor Connie Chang-Hasnain, Chair

Professor Ming C. Wu

Professor Xiang Zhang

Fall 2015

High Contrast Gratings for Optical Sensing

© Copyright 2015

By Tianbo Sun

All rights reserved

Abstract

High Contrast Gratings for Optical Sensing

by

Tianbo Sun

Doctor of Philosophy in Engineering-Electrical Engineering and Computer Sciences

University of California, Berkeley

Professor Constance J. Chang-Hasnain, Chair

Integrated optoelectronics has seen its rapid development in the past decades. It has been expanded to many emerging applications beyond optical communication, including environmental sensing, healthcare and remote sensing, etc. This revolutionary progress greatly benefits from device level innovation.

High contrast gratings (HCG) is an emerging element in integrated optoelectronics. Compared to the other elements, HCG has a very rich properties and design flexibility. Two most extraordinary properties of HCG are broadband reflectivity and high quality factor resonance, which are highly desired to solve current challenges in the aforementioned applications.

In this dissertation, we will explore the physical origins of the extraordinary features of HCG, and discuss its applications in optical sensing. Various device innovation for optical sensing, such as HCG slow light hollow-core waveguide for gas sensing, HCG resonator for bio-medical sensing, flexible surface plasma sensor , fast optical phase array and HCG-graphene spatial light modulator for remoting sensing are demonstrated with HCG as the enabling elements. With this breadth of functionality, HCG demonstrate itself as a promising platform for integrated optical sensing.

To my parents

Table of contents

Abstract	1
Table of contents	ii
List of figures	iv
Acknowledgments	xi
Chapter 1 Introduction	1
1.1 Introduction to High Contrast Grating	1
1.2 Optical Sensing	2
1.3 Dissertation Overview.....	3
Chapter 2 High Contrast Grating Basics	5
2.1 Introduction	5
2.2 HCG broadband reflector	7
2.3 HCG high quality factor resonator	8
Chapter 3 Slow Light Hollow Waveguide for Optical Gas Sensor	10
3.1 Introduction	10
3.3 Two Dimensional HCG-HCW: Low Loss Slow Light	12
3.4 Three Dimensional HCG-HCW: Wave Guiding and Slow Light.....	16
3.5 Device fabrication and characterization	20
3.6 Application in gas sensing	23
3.7 Conclusion.....	24
Chapter 4 High Contrast Grating Resonator and Its Application in Optical Bio-sensing and Nonlinear Optics	26
4.1 Introduction	26
4.2 HCG resonator design, fabrication and characterization	27
4.3 Sensitivity of the HCG device to changes in refractive index	31
4.4 Quantitative analysis of antibody-antigen interactions using HCG devices	32
4.5 Quantitative analysis of Troponin I.....	34
4.5 Discussion	35
4.6 HCG assisted SPP Flexible Biosensor	36
4.6.1 Introduction	36
4.6.2 Optical Sensor Design	36
4.6.3 Fabrication Process.....	38

4.6.4 Preliminary measurement results.....	40
4.6.5 Future application in catheter bacteria detection.....	41
4.7 Four Wave Mixing inside HCG Resonator.....	43
4.7.1 Introduction	43
4.7.2 High contrast gratings resonator design and fabrication	43
4.7.3 Enhanced four-wave mixing experiment.....	45
4.7.4 Discussion.....	48
4.7.5 Summary.....	49
Chapter 5 High Contrast Grating Based Spatial Light Modulator for Optical Remote Sensing	50
5.1 High Contrast Grating Optical Phased Array	50
5.1.1 Introduction	50
5.1.2 HCG MEMS piston phase tuner.....	51
5.1.3 All pass filter approach.....	53
5.1.4 HCG based all pass filter	55
5.1.5 HCG based all pass filter array for beam steering.....	60
5.1.6 Discussion.....	62
5.1.7 Summary and future work	64
5.2 Spatial light modulator using graphene integration with high contrast grating resonator	70
5.2.1 Introduction	70
5.2.2 Graphene integrated with HCG resonator	72
5.2.3 Graphene Effect.....	72
5.2.4 Static response	74
5.2.5 High speed modulation.....	75
5.2.6 Conclusion	76
Chapter 6 Summary and Outlook.....	78
References	80

List of figures

- Figure 1. 1 Three operation region for gratings. High contrast grating operates at the near subwavelength regime. And only allows 0th order reflection/transmission. 2
- Figure 1. 2 Optical Sensor Market Shares in 2010 (From Optoelectronics Industry Development Association (USA))..... 3
- Figure 2. 1 Schematic showing that three regions are divided to solve HCG analytically. 5
- Figure 2. 2 Contour map shows HCG reflection as function of input wavelength λ and grating thickness tg (both parameters are normalized b the grating period Λ). White dashed lines outline the HCG modes (C) predicated using Eq. (2.1). Dual-modes region is where all the interesting phenomena - broadband reflection and high-Q resonance happen..... 7
- Figure 2. 3 Reflectivity contour plot compared with the two modes' DC-component "phase difference" at the HCG output plane. (a) HCG reflection as function of input wavelength λ and grating thickness tg . (b) Phase difference between two modes as function of input wavelength λ and grating thickness tg 8
- Figure 2. 4 High Q resonance happen when there is two mode anti-crossing. Left bottom figure show the mode pattern of a high Q resonance, in which case, resonance happen in the vertical direction along the grating thickness. Intensity enhancement is on the order of 107, indicating a super high Q resonance. 9
- Figure 3. 1 Schematic of 1D HCG-HCW. Grating thickness t_g , period Λ and duty cycle η determine the reflection response, phase response Φ_{HCG} , which in turn determine the loss and modal dispersion. In an HCG-HCW, light travels by zig-zag reflections at the parallel reflectors (HCG in this case). 11
- Figure 3. 2 (a) The dispersion relationship (ω - kz diagram) of metal cladding HCW with a core size $d=3\mu\text{m}$. (b) The dispersion relationship of HCG HCW (shown as blue curves) compared with that of the perfect electrical conductor waveguide (shown as black curves). The background color shows the additional phase shift provided by HCG reflectors. Mode transition for two HCG-HCW modes happens between two adjacent PEC modes with phase accumulation equal to π 13
- Figure 3. 3 The optimization of the waveguide loss and reduced group velocity by changing the core size d . The background color indicates the reflection of the HCG reflectors. When the ω - β intersects with the red region, the mode inside the hollow core is bounded by the HCG reflectors. (a) ω - β line for a HCG-HCW with core size $d = 3\mu\text{m}$ (b) core size $d = 2\mu\text{m}$ (c) core size $d = 1\mu\text{m}$ 14
- Figure 3. 4 FDTD simulation for 2D HCG waveguide operating with fundamental mode. White dashed line illustrates the HCG waveguide region. Light is mainly confined inside the hollow core..... 15

- Figure 3. 5 FDTD simulation for 2D HCG waveguide. (a) Loss, group index and group dispersion analysis for the 2D HCG-HCW. Within a bandwidth of 120GHz, the loss is $< 0.1\text{dB/cm}$ and group delay is >100 (b) 5ps pulse propagation along the waveguide at different time slices..... 15
- Figure 3. 6 (a) The schematic for 3D “cage” HCG-HCW. (b) The mode profile at the cross section of the waveguide with core size $10\mu\text{m} \times 8\mu\text{m}$. The white box indicates the area of Si grating. (c) The beam profile in the lateral and transverse directions. The cosine shape of the profile, resembling that of a metal waveguide, indicates that the mode is not formed by index guiding. E_x and E_y are intensity profiles along the x and y directions in (a). (d) Loss spectrum for HCG “cage” waveguide with a $10\mu\text{m} \times 8\mu\text{m}$ core. Lowest loss can be below 0.05dB/cm 17
- Figure 3. 7 The ω - kz diagram for a “cage” waveguide with core size $1\mu\text{m} \times 6\mu\text{m}$. The background color indicates that the mode strength inside the waveguide excited by dipoles. Only the mode supported by the waveguide will build up intensity and is shown in red in the map. Black dashed lines highlight the deep red region and indicate the mode dispersion curve. Again, the black solid curve is the dispersion relation from a metal waveguide with same core size shown as reference. 18
- Figure 3. 8 Field intensity as a function of time and propagation distance. Red lines serves as reference, indicating the position of light line. (b) Pulse in time domain monitored at $100\mu\text{m}$ and $200\mu\text{m}$. Group velocity can be calculated basing on the pulse propagation, $v_g \sim 1/30c$ 19
- Figure 3. 9 Fabrication steps for cage waveguide..... 21
- Figure 3. 10 The SEM images of the fabricated 3D cage waveguide. Five identical waveguides are fabricated side by side to form a compact array. 21
- Figure 3. 11 (a) Mode pattern taken at the output facet of an 11mm long waveguide by a IR camera. (b) Loss measurement for the same waveguide in the wavelength range 1535nm to 1575nm 22
- Figure 3. 12 Pulse propagation inside air (blue) and slow light hollow HCG cage waveguide (red). $\sim 260\text{ps}$ delay is observed, which indicates group delay $ng \sim 10$ is reached inside our device. (Lase wavelength is centered at 1552.8nm)..... 23
- Figure 3. 13 Schematic of HCG-HCW as a gas sensor. Required length is reduced by factor of group index. Detection speed (limited by diffusion time) is greatly improved due to the novel structure. 24
- Figure 4. 1 High Contrast Grating Resonator as a label-free biosensing platform. (a) Schematic of a surface normal coupled high contrast grating (HCG) resonator. (b) SEM image of gratings within a single fabricated HCG resonator. (c) Schematic of the principle of using HCG resonator as protein binding sensing platform. Red dashed curve shows resonance wavelength will red-shift due to the protein binding at HCG surface. (d) A single mode fiber probe is immersed in the fluid above the HCG surface to avoid surface reflections. (e) A reflection spectrum recorded for a device having the

configuration schematized in (d). A tunable laser centered at 1550nm is used as excitation source and is run in a continuous sweeping mode. The reflection power is recorded in real time and is synchronized to laser sweeping rate.	28
Figure 4. 2 Fabrication process for HCG resonator. Only two main steps are needed to generate an on-chip high Q HCG resonator, including optical lithography and Si RIE etching.	29
Figure 4. 3 (a) Free space measurement setup. Free space laser, detector, beam splitter and a 5x objective are used in the measurement. We try to use as few as components to minimize the application cost. (b) Fiber based measurement setup. Single mode fiber is used as probe. Laser is coupled in from a tunable laser and coupled out to a fiber-based detector through a circulator. Fiber is used here to probe device under sample solution to avoid the surface multiple reflection.	30
Figure 4. 4 HCG resonator mode pattern. (a) Top view of the resonance inside the HCG cavity excited by Gaussian beam with a $10\mu\text{m}$ spot size. A large mode overlap with the input beam contributes to a simple and efficient coupling of the input light. (b) Side view of the resonance (showing one period) inside the HCG cavity. The resonance is designed to have large mode exposure to surroundings, which contributes to the high sensitivity of the device.	31
Figure 4. 5 Refractive Index Sensing. (a) Reflection spectra when HCG resonator is immersed in liquids with different refractive index ranging from 1.494 to 1.506. (b) Resonance wavelength as function of the change in refractive index.	32
Figure 4. 6 Antigen binding assays on the HCG device. (a),(b) Schematic of using HCG resonator for a label-free protein binding assay. (c) Real time recording of the interaction of surface bound goat anti-rabbit IgG for different concentrations of antigen (rabbit IgG). The dashed lines are the corresponding fits to these curves. (d) Red dots show the resonance wavelength shift corresponding to different purified rabbit IgG concentrations added to a HCG resonator surface-coated with anti-rabbit IgG. The red dashed line is the fit to measured data. Blue dots show the result of non-specific test indicating that mouse IgG/anti-rabbit IgG having a much lower shift in the resonance wavelength. The black triangles show the response of the HCG sensor to the addition of rabbit IgG dissolved in goat serum. The bars indicate the error range for the 3 measurements.	34
Figure 4. 7 (a) Measurement results for troponin I molecule inside PBS (red dots) and serum (black triangles). The bars indicate the error range over 3 measurements. (b) HCG sensor array combined with fiber array for high throughput screening.	35
Figure 4. 8 Schematic of HCG-assisted SPP sensor	37
Figure 4. 9 (a) Reflection as function of working wavelength and grating thickness. Period is chosen to be 600nm in this case and duty cycle is 50%. Vertical dotted line represents the effective index of SPP mode. (b) Reflection spectrum for a sensor design with period = 600nm, duty cycle 50% and grating thickness = 149nm (horizontal dotted line (a)).	37

Figure 4. 10 (a) FDTD simulation showing the mode pattern of SPP mode. Intensity is enhanced at the metal surface to improve the surface sensitivity. (b) Reflection as function of wavelength and grating thickness. Two resonance lines indicate SPP resonance with surface binding thickness $tb= 0\text{nm}$ and 20nm 38

Figure 4. 11 (a) Reflection spectra with different layer thickness of material attached to the surface. (b) Function of the resonance wavelength as function of material layer thickness attached to the metal surface..... 38

Figure 4. 12 Fabrication process for HCG-assisted SPP sensor. 39

Figure 4. 13 Measurement setup schematic: broadband source (500nm to 800nm) is used to excite the SPP resonance. Spectrometer is used to collect the reflection spectrum. Resonance wavelength shift will give us information on the sensor surface changing. 40

Figure 4. 14 (a) Reflection spectrum at different concentration of glucose concentration. (b) Resonance wavelength shift as function of different glucose concentration. Resonance wavelength shifts 15nm when there is index difference ~ 0.15 41

Figure 4. 15 (a) Cross section (b) Three dimensional view of the biosensor tubing 42

Figure 4. 16 (a) Schematic of HCG resonator. In this particular design, resonance is coupled by a surface normal plan wave input with TE polarization. Grating thickness t_g , period Λ and duty cycle are important parameters to determine the resonance wavelength and quality factor. (b) Top view of SEM image of gratings within a single fabricated HCG resonator. (c) Measured reflection spectrum for the HCG resonator. Linewidth shows 210pm, indicating $Q \sim 7330$. An absolute reflectivity (normalized by gold mirror) of 87% was achieved at the peak indicating a very high coupling efficiency. 44

Figure 4. 17 Schematic of the FWM measurement setup..... 46

Figure 4. 18 (a) Reflection beam spectrum taken from the OSA; -19.5dB conversion efficiency is achieved in this configuration. (b) Conversion efficiency as function of signal power. The slope of the Log-Log plot is nearly 2, indicating the idler signal is generated from FWM. 46

Figure 4. 19 Wavelength detuning: (a) Signal detuning with pump fixed at resonance wavelength (1538.9nm). (b) Pump detuning with fixed signal laser..... 47

Figure 4. 20 Conversion efficiency as a function of signal detuning. Red dots are measurement results. Black dashed line is from numerical simulation using Eq. (4.1). 48

Figure 5. 1 Schematic of using HCG as a piston mirror for phase tuner. The HCG is connected to the substrate with a spring. HCG can be electrostatically actuated by capacitor structure. When the HCG has been displaced by a distance Δd , the reflection light experiences a phase delay of $\Delta\varphi = 2k_0\Delta d$ 51

Figure 5. 2 Linear relationship between $V2\pi$ and f_r for a Si based HCG reflector. 53

Figure 5. 3 (a) Reflection spectrum and reflection phase spectrum of a FP cavity. (b) Reflectivity and reflection phase versus the cavity length, at a fixed incident wavelength of 1550nm. 53

Figure 5. 4 $R1$ is the reflection from top mirror and $R2$ is the reflection from bottom mirror. (a) Reflection dip become shallower with increase of bottom mirror reflection. (b) Phase spectra with various bottom mirror reflection. 54

Figure 5. 5 Bottom mirror reflection is fixed at 0.997. Top mirror reflection is varied from 0.85 to 0.99. (a) Amplitude reflection spectra with various $R1$ value. (b) Phase reflection spectra with various $R1$ value. 55

Figure 5. 6 Schematic of an individual pixel of the optical phased array. The $\text{Al}_{0.6}\text{Ga}_{0.4}\text{As}$ HCG and 22 pairs of $\text{GaAs}/\text{Al}_{0.9}\text{Ga}_{0.1}\text{As}$ DBR serve as the top and bottom reflector of the Fabry-Perot etalon. The incident light is surface normal to the etalon, and polarized in parallel to the grating bar. λ , HCG period; s , grating bar width; t_g , HCG thickness; d , air gap between HCG and DBR. We design $\lambda=1150$ nm, $s=700$ nm, $t_g=450$ nm, and $d=700$ nm. 56

Figure 5. 7 SEM image of an 8x8 optical phased array. Each pixel is an HCG-APF, which can be individually electrically addressed by the fanned-out metal contacts. The pitch of the HCG mirror is ~ 33.5 μm . (b) Zoom-in view of the HCG mirror in a single pixel. The HCG mirror size (without the MEMS) is 20 μm by 20 μm 57

Figure 5. 8 (a) Reflection spectrum of an HCG-APF with different actuation voltages. As the reversed bias increases, the cavity length decreases, resulting in a blue-shift of the resonance wavelength. (b) Reflection phase shift versus applied voltage on a single HCG-APF of the phased array. $\sim 1.7 \pi$ phase shift is achieved within 10V actuation voltage range at a wavelength of 1550 nm; this corresponds to a displacement of ~ 50 nm of the HCG. The measured results are curve fitted to extract the reflectivity of the DBR and HCG. 58

Figure 5. 9 (a) Laser Doppler velocimetry measurement to characterize the mechanical resonance frequency of the HCG MEMS mirror. (b) Time resolved phase measurement of the HCG APF with a step voltage actuation signal. The blue dots are recorded in the experiment, and red traces are the simulated fitting curve from the second harmonic oscillator model. 59

Figure 5. 10 Comparison of the ringing between a single step and two step voltage control. In the two step voltage control case, the time interval between the two different steps is 1 μs , corresponding to half of the ringing period. The individual ringing from these two separate steps would have destructive interference, leading to an overall reduced ringing. 60

Figure 5. 11 Experimental setup to characterize the reflection phase of the HCG APF phased array, as well as the beam steering performance. WP, wave plate; pol. BS, polarization beam splitter; Obj., objective; pol., polarizer; TFOV, total field of view. 61

- Figure 5. 12 Image of an assembly of the optical phased array system. The chip is bonded on the chip carrier (a), which is hosted by a printed circuit board (b)..... 61
- Figure 5. 13 Beam steering experiment. (a) Near-field phase pattern created by the HCG-APF optical phased array. (b) The corresponding far-field pattern calculated by Fourier optics. (c) Experimentally measured far-field pattern, in reasonable good agreement with the calculation. The strong zeroth order beam is due to the relatively low filling factor of the phased array (~36%). The light that does not hit on the HCG-APF gets directly reflected without phase shift, contributing strongly to the zeroth order beam. The field of view of the image windows is $13^\circ \times 13^\circ$. The box in dashed line in (c) indicates the TFOV of the phased array ($9.14^\circ \times 9.14^\circ$). 62
- Figure 5. 14 (a) SEM image of the two-dimensional HCG mirror for HCG-APF array. (b) Beam steering experiment of the optical phased array using two-dimensional HCG as the top mirrors of the APF. Top panel, near-field phase pattern created by the HCG-APF optical phased array. Middle panel, the corresponding far-field pattern calculated by Fourier optics. Bottom panel, experimentally measured far-field pattern, in good agreement with the calculation. 64
- Figure 5. 15 (a) Schematic of a HCG lens. (b) SEM images for a 2D HCG lens. Devices are fabricated on SOI wafer, and the grating is sitting on oxide. 65
- Figure 5. 16 (a) Simulated intensity of reflected beam as a function of different position for 2D lens. Positions for HCG lens and Gaussian source are indicated in the figure. (b) Laser beam spot image at different position along the propagation. (c) Beam profile along the cross section. Red dots show the experimental measurement and blue curves show the simulation results..... 66
- Figure 5. 17 Spot Size vs, propagation distance for 2D lens. Different colour represents different wavelength. 66
- Figure 5. 18 Simulated intensity of reflected beam as a function of different position for 1D cylinder lens. Positions for HCG lens and Gaussian source are indicated in the figure. (b) Laser beam spot image at different position along the propagation. (c) Beam profile along the cross section. Red dots show the experimental measurement and blue curves show the simulation results. 67
- Figure 5. 19 (a) Spot Size vs. propagation distance for 1D cylinder lens. Different colour represents different wavelength. Black curves on the top gives the spot size in y direction. (b) Reflection spectra for gold mirror (red) and HCG reflective lens (black). Reflection for gold mirror is calibrated to be 98.5%. 68
- Figure 5. 20 (a) Combining optical phased array with HCG lens array to improve filling factor to nearly 100%. Schematic of lens array is shown in the right top corner. (b) FDTD simulation shows the HCG lens array performance. Left figure shows intensity pattern at focal plane. Right figure shows that after going through a single cell inside lens array. Majority of the energy will be focused into a $10\mu\text{m} \times 10\mu\text{m}$ region. 69

Figure 5. 21 (a) Schematic of changing fermi level of graphene by applying voltage to graphene through a capacitor structure. (b) Changing of fermi level will ‘turning on’ or ‘turning off’ optical transition at corresponding wavelength. 70

Figure 5. 22 Schematic of HCG graphene spatial light modulator. Light is directly coupled from surface normal direction. In this case, ion-gel is covered on top of device to uniformly gate the graphene. 71

Figure 5. 23 (a) FDTD simulation of top view of resonance mode pattern with a $10\mu\text{m}$ Gaussian beam as excitation source coming from surface normal. White bars indicate the grating area. Large mode overlap between resonance mode pattern and input source contributes to easy and efficient coupling. (b) Side view of the resonance inside one period is shown. White dashed line indicate the outlines of grating. Grating mode is specially designed to allow more mode exposure to the surface in order to achieve better graphene light interaction. Right side shows the cross section profile along the center of grating bar. 72

Figure 5. 24 Process flow of Graphene transfer. 73

Figure 5. 25 (a) SEM images of HCG cavity with and without graphene. Top image is the HCG cavity before graphene transfer. Bottom image shows the cavity after graphene transfer. Pinholes inside the graphene layer serve as an evidence that graphene is indeed on top of the cavity. Surprisingly, the pinholes didn’t affect the performance of the graphene as an effective absorber. (b) Reflection spectrum before (red curve) and after (green curve) graphene transfer. 12dB difference is achieved at 1572nm. Green curve is multiplied by 5 times and plotted with the red curve. 74

Figure 5. 26 (a) cavity reflection spectrum with various gate voltage from -2V to 0V. (b) Resonance wavelength as function of applied voltage. (c) Cavity linewidth as function of applied voltage. (d) Reflection at 1590nm in log scale as function of applied voltage. 75

Figure 5. 27 Side view and top view of dual layer graphene HCG spatial light modulator. 76

Figure 5. 28 (a) HCG resonator array fabricated on top one single SOI, with same device thickness, however different period and duty cycle. (b) Large working wavelength range, from 1460nm to 1660nm, covering 200nm. 77

Acknowledgments

First and foremost, I thank my advisor Professor Connie Chang-Hasnain for her continuous guidance, support and encouragement through my graduate school career. She not only show me the path to success, but always encourage me to challenge the best and myself. Without her, I would not reach this far. For that, I am forever grateful.

I also thank Professor Ming Wu, Professor Eli Yablonovitch, and Professor Xiang Zhang. Each has greatly influenced my academic growth during the past five years. I particular thank them for the review on this dissertation and serving on my qualifying exam committee.

My journey in Berkeley has never been alone. I thank very much for the accompany and help from a group of remarkable young researchers. I thank Dr. Forrest Sedgwick. As my first mentor in Berkeley, he helped me conquer the fear as a beginner. I owe my thanks to Dr. Weijian Yang for his patient guidance, training and help. I am particularly grateful to Dr. Chris Chase, Dr. Roger Chen, Dr. Devang Parekh, Dr. Yi Rao, Dr. Thai Thran, Dr. James Ferrara, Dr. Fanglu Lv, Dr. Wai Son Ko, Dr. Fan Ren and Adair Gerke for their wisdom and advice not only in research but also in life. I want to express my thanks to Li Zhu and Kun Li, who attended Berkeley together with me and have studied and worked together for the last five years. I would like to thank Vadim Karagodsky for his fundamental exploration of the HCG theory, which paved the road for many research not only for me but also for the whole group. Finally, I thank all the optoelectronics students who have been reliable source when discussion and help are needed.

It has been my great pleasure to have many collaborators across the world. I want to express my special thanks to Professor Gerard Marriott and Dr. Shu Kan in Bioengineering department at UC Berkeley; Professor Feng Wang and Dr. Jonghwan Kim in Physics department at UC Berkeley; Dr. Byung-wook Yoo in Prof. Ming Wu's group at UC Berkeley, Professor David Horsley, Dr. Trevor Chan and Dr. Mischa Megens at UC Davis, Professor Weiwei Hu at Perking University, Professor Fang Liu at Tsinghua University, Dr. Weimin Zhou at US Army Research, and Dr. Krishnan Parameswaran at PSI Inc. for the fruitful collaboration.

I thank the Marvell Nanolab staff for their support in device fabrication and characterization. In particular, I thank Dr. Bill Founders, Kim Chan, Neal Melton, Richelieu Hemphill, Marilyn Kushner and Ryan Rivers for their instant help when I met problem in the lab and for their kind forgiveness on my unintended mistakes.

For financially supporting me during my graduate studies, I thank DARPA SWEEPER and NSF.

Last but certainly not least, I must thank my family, which has shown tremendous patience, love, and support throughout my life. I especially thank my parents, and I feel utterly indebted for you. My love and special thank also go to Yang Bai, who supports,

encourages and loves me. Together we have been through difficulties and joys. And we will spend a life-long time in the future.

Chapter 1 Introduction

1.1 Introduction to High Contrast Grating

Optical gratings are fundamental devices with a long history. In the 1600s, James Gregory first discovered gratings by observing the diffraction of light through a bird's feather [1]. Since then, gratings have become an important components of many optical systems (i.e. grating coupler, monochromators, spectrometers and filters, etc.). Normally, traditional gratings are simply divided into two regimes: the diffraction grating regime, where the grating period (Λ) is larger than the input wavelength (λ); and the deep-subwavelength regime, where the grating period is much smaller than the input wavelength [2, 3]. However, there is a third, relatively less studied regime, where grating period is between the input wavelength inside grating material and inside surrounding media. In this special subwavelength regime, gratings behaves differently and exhibits many extraordinary features [4-26]. Recently, our group discovered a new near-wavelength grating structure in which the high-index medium is surrounded by low-index materials, refereed as a high-contrast gratings (HCG) [4-26], shown in Figure 1. 1. Among all the extraordinary features enabled by high contrast gratings structure, two are worth mentioning and serve as fundamental blocks for many devices described in this thesis. One is ultrabroadband high reflectivity ($>98.5\%$ over a wavelength range of $\Delta\lambda/\lambda > 35\%$). Another feature is high-quality-factor resonance inside grating layer (Quality factor (Q) $> 10^8$ can be obtained from design). The high index contrast, and subwavelength periodicity are two key features differentiated it from other gratings which are etched on a high index substrate without the additional index at the exiting plane and usually operate at diffraction regime. With these unexpected properties, HCGs establish a new platform for integrated optics and optical sensing.

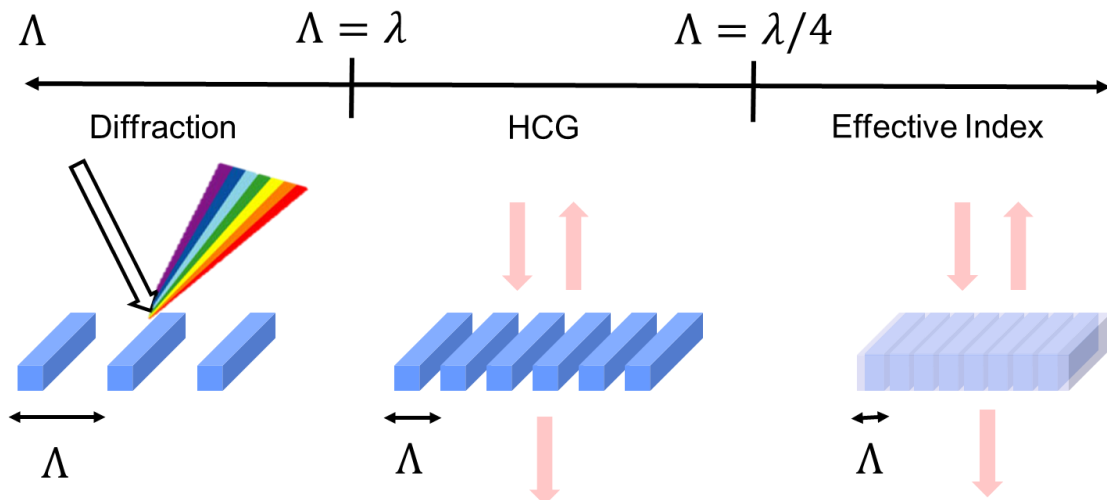


Figure 1. 1 Three operation region for gratings. High contrast grating operates at the near subwavelength regime. And only allows 0th order reflection/transmission.

1.2 Optical Sensing

In recent years, sensor has been widely used in many applications including industrial and daily-life applications. A growing number of industrial applications has been demonstrated, which run from process control to safety and security improvement, transportation, environment, structural failure monitoring and food quality. Also, sensors for health care, climate control and indoor detection of toxic substances are attracting more and more attentions and starting to appear in people's daily life [27].

Optical sensor has many unique properties which make itself a strong candidate for these existing and emerging applications. First, using light as a probe, optical sensor usually offers higher sensitivity to small changes in the surroundings. Secondly, there is a strong decrease in the price of most optical components, partially benefitting from the increasing diffusion of low-cost optical telecommunication components. Thirdly, recent progress in integrated photonics allows easy integration of many optical devices, together with microfluidic or electrical system, into one chip, which greatly increase the manufacturing ability and reduce the cost for single unit.

According to the analysis from the Optoelectronics Industry Development Association (USA), the market for optical sensors alone for 2010 exceeds 5 billion dollars, shown in Figure 1. 2. And this number is continuously increasing with new applications and new markets showing up every year [27].

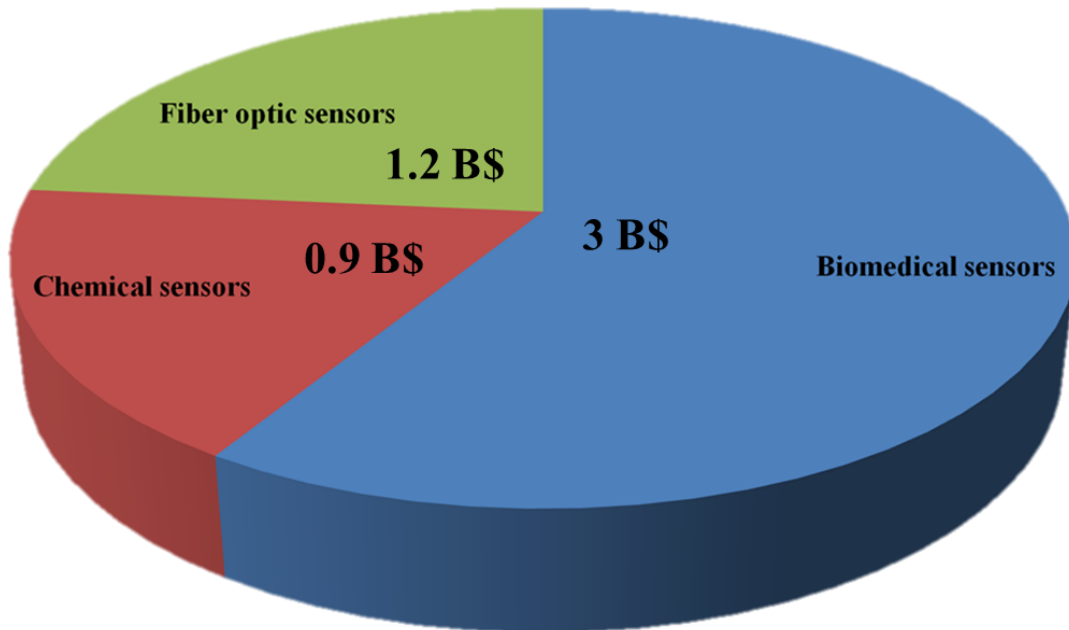


Figure 1. 2 Optical Sensor Market Shares in 2010 (From Optoelectronics Industry Development Association (USA)).

1.3 Dissertation Overview

Motivated by the extraordinary features of HCG and its huge potential in integrated optoelectronics, this dissertation devotes to demonstrating HCG as a platform for optical sensing.

In Chapter 2, we will briefly discuss the unique features of HCG, and the physical origins of these properties. We show that HCG can be easily designed using simple guidelines, rather than requiring heavy numerical simulation through the parameter space. Using top-down design algorithm, HCG can be designed to be a broadband high reflective mirror and high-quality factor resonator. The subsequent chapters explore various applications of HCG.

Chapter 3 reports a novel slow light hollow waveguide using HCG. The hollow waveguide using four HCG reflectors is designed, optimized and fabricated for slow light operation. Three dimensional light guiding and slow light effect are experimentally demonstrated. Propagation loss of 2dB/cm and slowing down factor ~ 5 are observed in the experiment. These experiments set up a slow light hollow waveguide platform, where compact gas/liquid sensors can be enabled. In particular, comparing with traditional guided-wave optical sensor, HCG slow light hollow waveguide sensor offers stronger light-mater interaction and unique structure for rapid detection. All these advantages make itself a promising platform for on-chip gas sensor.

Chapter 4 reveals HCG, an ultra-thin layer (\sim a few hundred nm) of semiconductor gratings, can be designed to generate strong resonance inside the thin grating layer. Unique resonance pattern of HCG resonators increases the light interaction with surrounding and also provide direct and efficient coupling with off-chip light source. In this chapter, we focus on demonstrating HCG resonator as platform for rapid and label-free detection of protein biomarkers in the following aspects: Scalable manufacture together with simple test setup enables the device as low-cost point of care solution. A complementary anti-rabbit/rabbit IgG are used to generate thermodynamic and kinetic data. In addition, the device is used to detect serum cardiac troponin I, a biomarker of cardiac disease to 100pg/ml (0.004nM) within 4 minutes, which is faster, easier than and as sensitive as current assays and demonstrates the potential as a point of care device in clinical applications. Furthermore, to meet the demand of wearable devices in various applications of healthcare, we explore the possibility of combining surface plasma with HCG to construct flexible biosensor platform,

In chapter 5, we focused on spatial light modulator for remote sensing application. First, an optical phased array using HCG all-pass filter is investigated. The all-pass-filter provides an efficient mechanism for phase tuning. Fast (MHz) optical beam steering using this phased array is experimentally demonstrated. Secondly, to further increase the

operation speed, a novel HCG-graphene spatial light modulator are demonstrated. One atomic layer Graphene is integrated with HCG resonator, where graphene absorption is tunable through applied voltage, and HCG resonator amplifies the absorption by the times of resonance quality factor. 12dB modulation depth is achieved within 2V and potentially GHz modulation speed is expected with simple geometry optimization.

Chapter 6 summaries the dissertation and discuss the outlook and future work for the further development of using HCG as optical sensor platform.

Chapter 2 High Contrast Grating Basics

2.1 Introduction

To better understand the physics behind HCG, we will explore the origin of these extraordinary properties. First, we can divide the space into three regions, separated by the HCG input plane $z = 0$ and output/exit plane $z = t_g$. In region I, $z < 0$, there are incoming plane wave and reflected waves. In region II, $0 < z < t_g$, the solutions are modes of a periodic array of slab waveguides. In region III, $z > t_g$, there exist only the transmitted waves [10]. This is shown in Figure 2. 1.

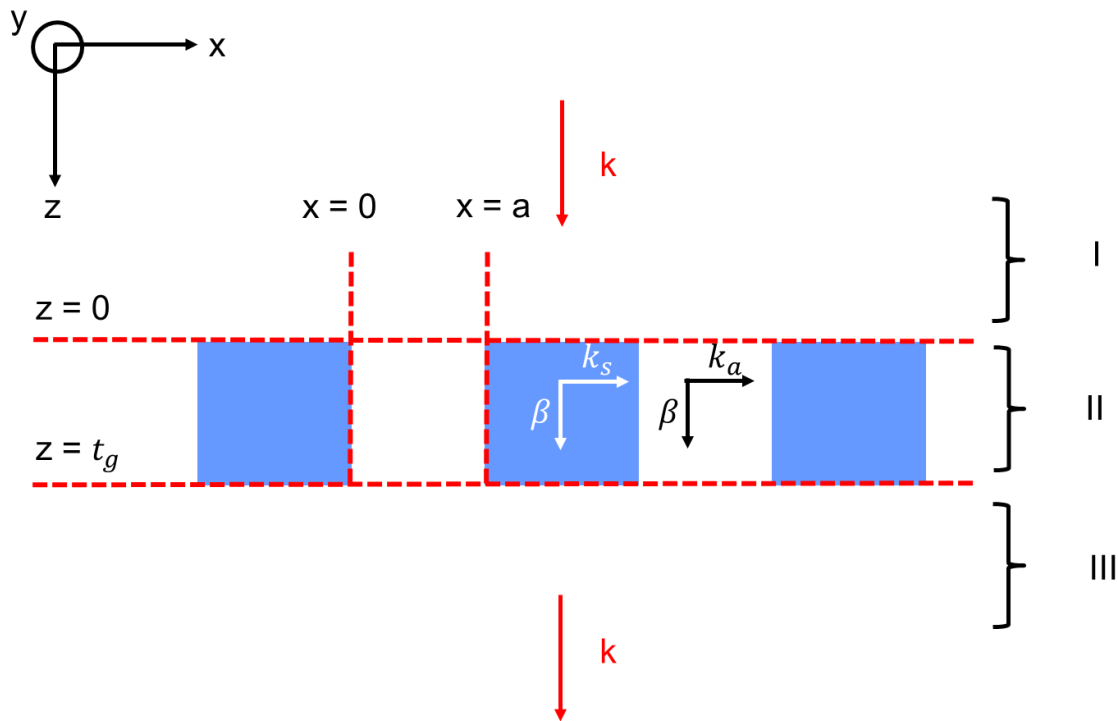


Figure 2. 1 Schematic showing that three regions are divided to solve HCG analytically.

The waveguide array structure in the x direction allows several propagating modes in region II. These modes are orthogonal and don't interact with each other while propagating. When the propagating modes meet the boundaries in the z direction (namely

the $z = 0$ and $z = t_g$ planes), these modes are confined and thus a cavity is formed in z direction. At these boundary planes, these array waveguide modes can couple to the plane waves in region I and II, and also can couple into each other due to abrupt change in boundaries. When these modes interfere with each other at the input/output planes, interesting phenomena will happen. From the perspective of a cavity, we can envision that ϕ and ρ matrices dominantly determine the HCG properties, where ϕ the propagation is factor for the modes inside regime II and ρ is the coupling matrix at the boundaries planes. Similar to a simple FP cavity, HCG support a self-sustainable mode (represented by a vector C) which satisfies the round-trip condition inside the cavity (region II in Figure 2. 1), thus:

$$C = \rho\phi\rho\phi C. \quad (2.1)$$

There are three unknowns inside Eq. (2.1), thus we need two more boundary condition to solve it: Plane wave in region I couples into C at the input plane; and C couples into plane wave (including higher order evanescent mode) in region II. These two boundary conditions together with Eq. (2.1) give us full solution to HCG structure.

Next, we plot the reflectivity of HCG as a contour map as function of wavelength and grating thickness (both parameters are normalized by period Λ) for a surface-normal incident TE-polarized light onto the HCG (TM polarization slightly different pattern, however similar principle). A well-organized ‘checkboard’ pattern is clearly shown in the dual-mode regime. White dashed lines outline the HCG modes (C) predicated using Eq. (2.1). We note that half of the ‘checkboard’ space shows high reflectivity (dark red in the color map). Also there is region where sharp transition in reflection happens at the joint point of each checkboard, indicating a strong resonance. We will devote this chapter to briefly discuss the physics behind these two important features. They will become the building fundament ion for all the device discussed in this thesis. We won’t go through any detail of the analytical treatment here since it is beyond the scope of this thesis. Reference 10 provide a thorough review on this problem.

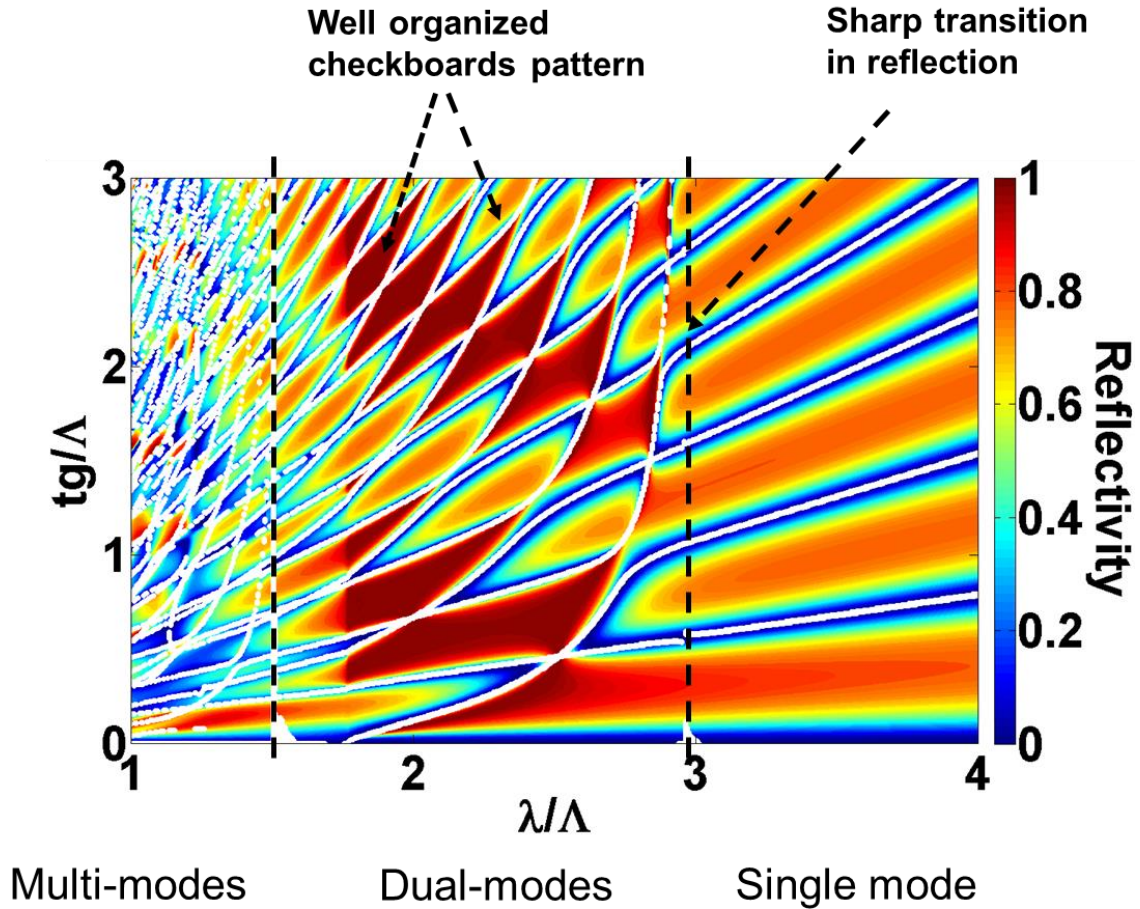


Figure 2. 2 Contour map shows HCG reflection as function of input wavelength λ and grating thickness t_g (both parameters are normalized by the grating period Λ). White dashed lines outline the HCG modes (C) predicted using Eq. (2.1). Dual-modes region is where all the interesting phenomena - broadband reflection and high-Q resonance happen.

2.2 HCG broadband reflector

As we discussed in the previous paragraph, the HCG can be designed to exhibit a wide dual-mode regime. Intuitively, if the two modes have complete destructive interference at the HCG output plane, the transmission will then vanish, yielding 100% reflectivity. This is clearly proven by comparing the reflection map with map showing the phase difference between the two modes. It is seen that the ‘checker-board’ pattern aligns well with the two modes’ phase difference contour. When the phase difference equaling π , they tend to cancel each other in the transmission, yielding a high reflection. At the two modes’ region, except at the resonance lines where the input plane wave is strongly coupled into one of the modes. Thus the two modes’ phase difference dominantly determines the reflectivity contour. Again for more detailed analysis, please find more information in reference 10.

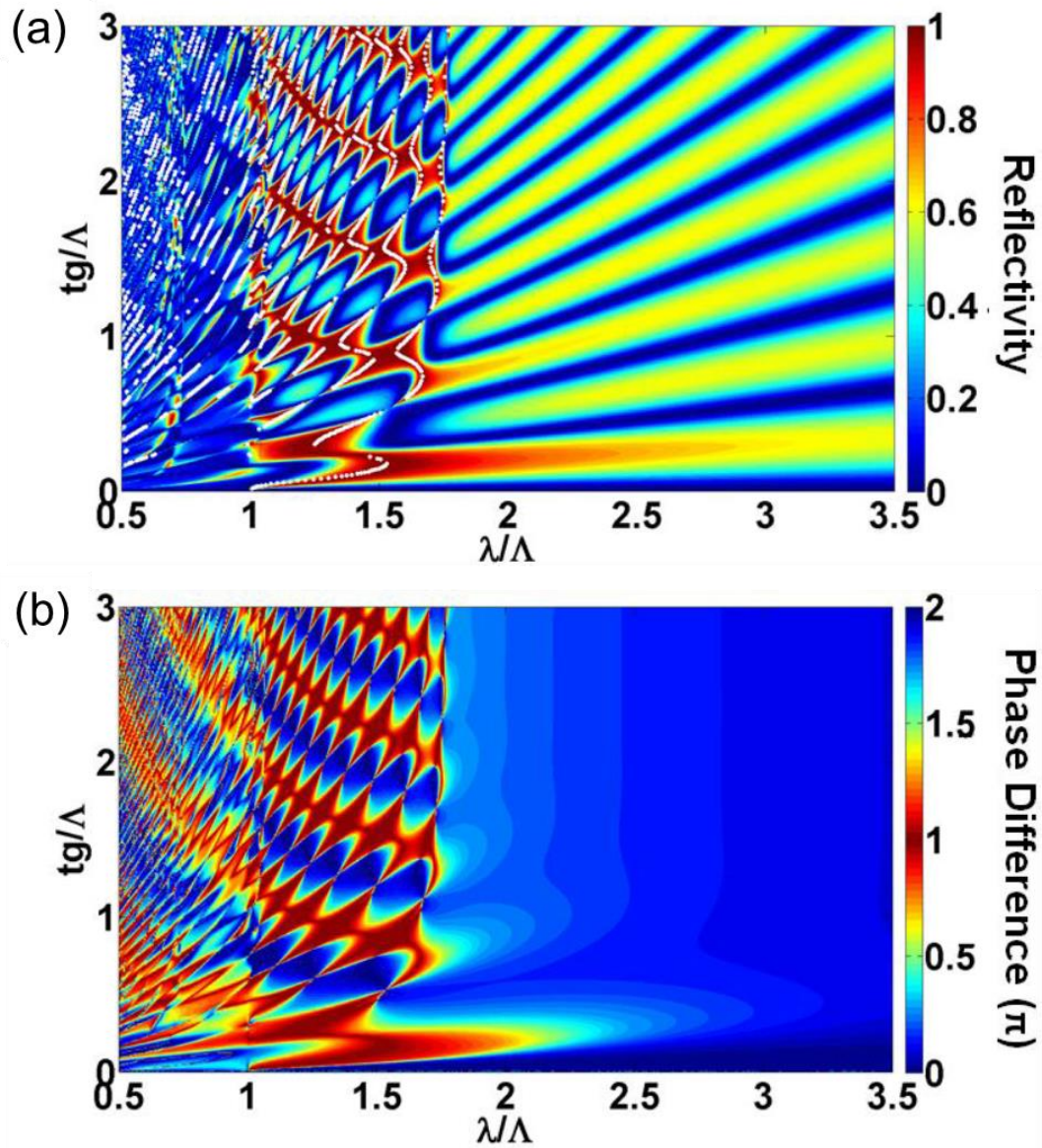


Figure 2. 3 Reflectivity contour plot compared with the two modes' DC-component "phase difference" at the HCG output plane. (a) HCG reflection as function of input wavelength λ and grating thickness t_g . (b) Phase difference between two modes as function of input wavelength λ and grating thickness t_g .

2.3 HCG high quality factor resonator

Unlike other gratings, HCG devices have high refractive index contrast at both the entrance and exit planes. The large refractive index contrast between the grating plane and its surrounding results in a strong coupling between grating modes at both exit and entrance

boundaries. By choosing appropriate grating period and duty cycle, a HCG design supporting only two modes can easily be obtained. Next with the right thickness, these two grating modes can be made to interfere constructively at the entrance and exit boundaries, resulting in a high-Q resonator with light propagating in the direction normal to the grating plane [20, 25]. We summarize the basic principle in the following: Eq. (2.1) provides an intuitive illustration of the resonance nature. Each self-sustainable modes defined in Eq. (2.1) will have an intrinsic Q associated, and this can be calculated a general formula:

$$Q = \frac{2\pi n_g t_g}{\lambda} \left| \frac{r}{1-r^2} \right|. \quad (2.2)$$

where t_g is the thickness of the grating, λ is the wavelength of the incident light, n_g is the group index, and r represents the eigenvalues of matrix $\rho\phi$. The supermode with highest Q will dominate and represent the Q value of the entire structure [16]. In Figure 2. 4, we show that high Q resonance happen when there is two mode anti-crossing. Left bottom figure show the mode pattern of a high Q resonance, in which case, resonance happen in the vertical direction along the grating thickness. Intensity enhancement is on the order of 10^7 , indicating a super high Q resonance.

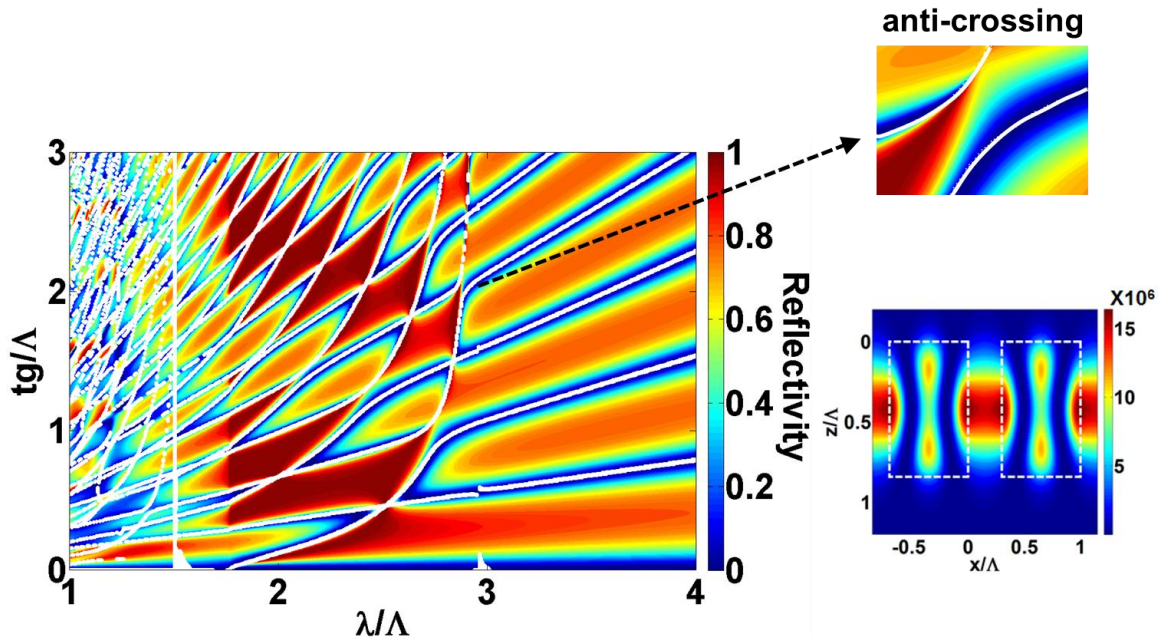


Figure 2. 4 High Q resonance happen when there is two mode anti-crossing. Left bottom figure show the mode pattern of a high Q resonance, in which case, resonance happen in the vertical direction along the grating thickness. Intensity enhancement is on the order of 10^7 , indicating a super high Q resonance.

Chapter 3 Slow Light Hollow Waveguide for Optical Gas Sensor

3.1 Introduction

Conventional light guiding is usually achieved by index guiding, where light is confined inside a high-refractive-index solid core surrounded by low-refractive-index cladding. However, many emerging applications including mid-IR laser surgery [28], gas-based nonlinear optics [29, 30] and gas/fluid sensing [31-35] require the opposite scheme: guiding light through a hollow core waveguide (HCW) [36]. In particular, the hollow core simultaneously serves as channel for light and substance to be probed with the light, greatly increasing light-matter interaction and enabling a compact and sensitive detection platform. Recently, chip-scale hollow core waveguides sensors have received intense investigation due to both their potential for integration with electric/photonic circuits and their scalable, cost-effective manufacturability [37, 38, 39].

Highly reflective mirrors are essential to realize low-loss HCWs. Various on-chip HCWs have been reported, using ant resonant reflecting, metallic shells, distributed Bragg reflectors (DBRs) and photonic crystal (PhCs) as reflectors [40]. However, high optical loss due to the reflectors' insufficient reflectivity limits the uses of the aforementioned HCW.

From the discussion in Chapter 2, we can see that high contrast gratings (HCG) offer a broadband high reflectivity for both surface-normal and oblique incident light [10]. In this work, we propose a novel design of low-loss hollow-core waveguides using HCG as reflector. Additionally, leveraging the strong phase dispersion [12], an HCG hollow core waveguide (HCG-HCW) can produce a large group velocity reduction. We report a two-dimensional (2D) slab HCG-HCW design with loss $\sim 0.1\text{dB/cm}$ and group velocity $v_g \sim c/80$. Furthermore, we expand our model to three-dimensional cases by modeling waveguiding and slow light phenomena inside a 3D HCG-HCW. The structures we propose here are superior in sensing applications for the following reasons: first, slow light propagation significantly increases the light-matter interaction [41, 42] per unit length, which enables more compact integration; second, gas molecules can be flown into the waveguide from the side openings instead of from the two ends of the waveguide. Dynamic detection speed may benefit from this by orders of magnitude.

3.2 Two Dimensional HCG-HCW: Basic Concept

A high-contrast grating (HCG) consists of a single layer of sub-wavelength grating with a high refractive index (e.g. Si or III-V compound), fully surrounded by low-index materials (e.g. air or oxide). It has been demonstrated to be a broad bandwidth high reflection mirror both at the normal incidence angle and glancing angles. 2D HCG-HCW can be viewed by

a simple picture of ray optics: light is guided by zig-zag reflections between two parallel HCG reflectors, shown in Figure 3. 1. The hollow “core” size of the waveguide is the separation of two HCG reflectors, d . Each HCG reflector is characterized by following parameters: thickness t_g , grating period Λ and duty cycle η . The duty cycle is the ratio of bar width to grating period. These parameters determine the reflection of HCG.

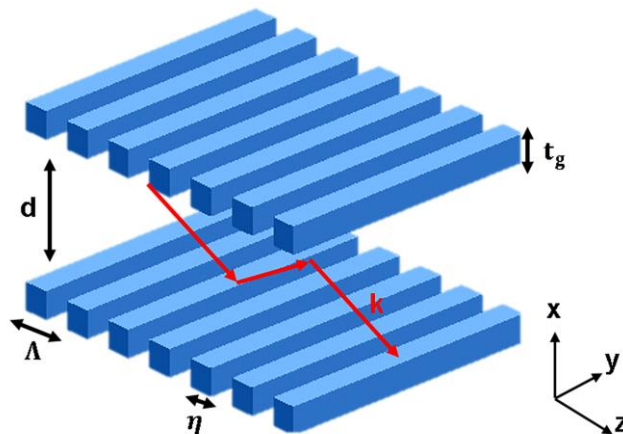


Figure 3. 1 Schematic of 1D HCG-HCW. Grating thickness t_g , period Λ and duty cycle η determine the reflection response, phase response Φ_{HCG} , which in turn determine the loss and modal dispersion. In an HCG-HCW, light travels by zig-zag reflections at the parallel reflectors (HCG in this case).

In the 2D case, the waveguide modes are described with the round-trip condition in x direction shown below:

$$d \times \sqrt{\left(\frac{\omega}{c}\right)^2 - k_z^2} + \phi_{HCG} = m\pi \quad (3.1)$$

where ω is the angular frequency of the light, k_z is the z component (z direction in Figure 3. 1) of the k vector, and $\phi_{HCG}(\omega, k_z)$ is the phase change upon reflection at the HCG. The phase change strongly depends on both ω and k_z ; m indicates different orders of transverse mode in x direction. The propagation loss and the effective mode index are then calculated using the following formulae [22]:

$$Loss \left[\frac{dB}{m} \right] = 10 \log_{10} R(\omega, k_z) \cdot \sqrt{\omega^2 - c^2 k_z^2} / (d \cdot k_z \cdot c) \quad (3.2)$$

$$n_{eff} = \frac{k_z}{k_0} = 1 / \sqrt{\left(\frac{m\pi - \phi_{HCG}}{k_z d} \right)^2 + 1} \quad (3.3)$$

The modal group index (defined as c/v_g) then can be written as the following:

$$n_g = n_{eff} + \omega \cdot \frac{dn_{eff}}{d\omega} = n_{eff} + \frac{\omega(m\pi - \phi_{HCG})}{(k_z d)^2} n_{eff}^3 \frac{\partial \phi_{HCG}}{\partial \omega} \quad (3.4)$$

Eq. (3.1) indicates that the waveguide loss is logarithmically dependent on the HCG reflection. Thus designing a highly reflective HCG is crucial to achieving a low-loss HCG-HCW. Also, from Eq. (3.4), we notice that the group index is proportional to HCG phase dispersion $\partial\phi_{HCG}/\partial\omega$. Therefore, by utilizing the strong phase dispersion from the HCG's reflection, we can extensively manipulate the group velocity for a certain waveguide mode while maintaining the extremely high reflectivity of the HCG. This enables a new, low-loss approach for on-chip slow light propagation.

3.3 Two Dimensional HCG-HCW: Low Loss Slow Light

In this section, we discuss our intuitive design algorithm for achieving low loss slow light inside a 2D HCG-HCW based on Eq. (3.1) to (3.4) above. We use rigorous coupled mode analysis (RCWA) to calculate the HCG reflection coefficient $R(\omega, k)$ and phase $\phi(\omega, k)$ as functions of various wave vectors (k) and frequency (ω). First, ideal metal hollow-core waveguide dispersion curves are plotted as reference in Figure 3. 2 (a). Here we use perfect electric conductors (PEC) as reflectors and set the reflection phase $\phi_{HCG} = 0$ for all frequencies. The same metal dispersion curves are also reproduced in Figure 3. 2 (b) to serve as general guidelines and for comparison with the HCG modes. Figure 3. 2 (b) shows the ω - k_z diagram for various waveguide modes in a HCG-HCW, each shown by a distinct blue curve. The HCG-HCW modes significantly deviate from the metal-waveguide modes due to the large HCG phase dispersion $\partial\phi_{HCG}/\partial\omega$. In Figure 3. 2 (b), we also plot the HCG reflection phase $\phi_{HCG}(\omega, k_z)$ as a color contour plot in the background. When the HCG reflection phase $\phi_{HCG}(\omega, k_z)$ is equal to 0 or π , the HCG-HCW's ω - k_z line intersects with metal-waveguide mode line (the white and yellow circles in Figure 3. 2 (b)). This means that the mode of HCG-HCW is the same as that of an ideal metal-waveguide at these points, since when $\phi_{HCG}(\omega, k_z)$ equals to 0 or π , the HCG acts just like a metal mirror. However, when $\phi_{HCG}(\omega, k_z)$ is not equal to 0 or π , the HCG ω - k_z curve deviates from the metal-waveguide line. It intersects with the next metal-waveguide mode only when the accumulated phase is equal to π . In essence, with the extra HCG phase dispersion, the HCG-HCW ω - k_z line connects two neighboring metal-waveguide lines. This effectively makes the mode transit to a lower modal number. This transition introduces a region of the ω - k_z curve with a flattened slope, indicating a reduced group velocity.

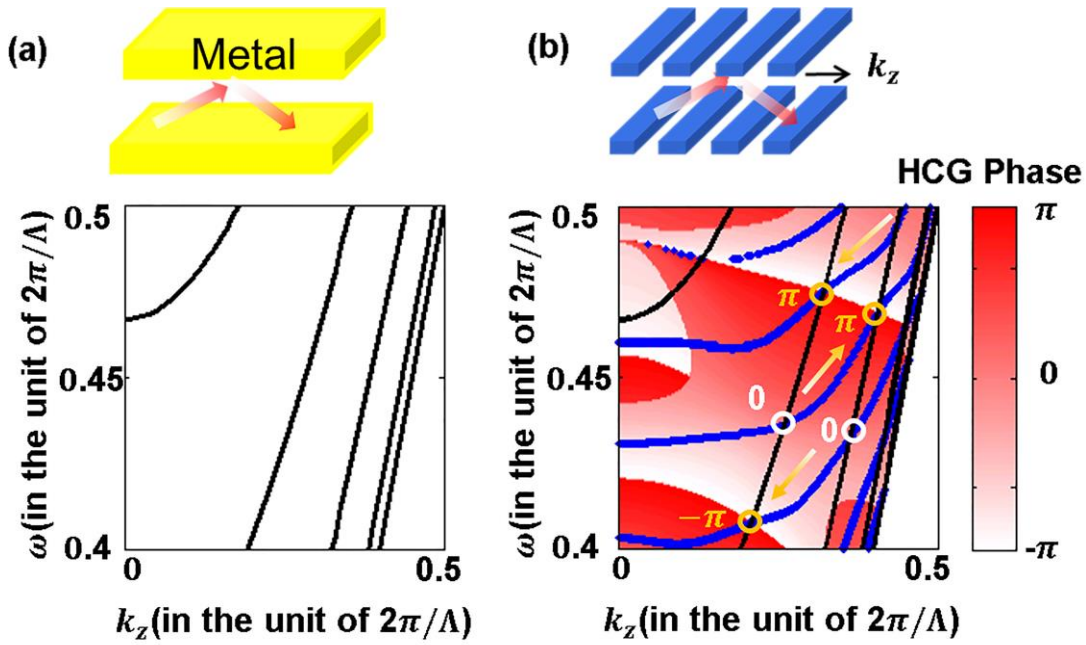


Figure 3. 2 (a) The dispersion relationship (ω - k_z diagram) of metal cladding HCW with a core size $d=3\mu\text{m}$. (b) The dispersion relationship of HCG HCW (shown as blue curves) compared with that of the perfect electrical conductor waveguide (shown as black curves). The background color shows the additional phase shift provided by HCG reflectors. Mode transition for two HCG-HCW modes happens between two adjacent PEC modes with phase accumulation equal to π .

Above, we studied the origins of slow light inside HCG-HCW. The advantage of using HCG for slow light HCW is shown in its design flexibility, where loss and group velocity can be optimized separately. On one hand, designing a slow light waveguide is very intuitive: the strong HCG reflection phase dispersion causes mode transition, where the flattened dispersion curve represents a reduced group velocity. In addition, it can be seen from Figure 3. 3 (a)-(c) that by reducing the core size d , the metal-waveguide lines can be pushed apart. This can lead to a larger range of flat slope in HCG-HCW ω - k_z curve or a reduced group velocity. The explanation can also be seen from Eq. (3.4): in general, the smaller d in the denominator will lead to a larger group index. On the other hand, the reflectivity of the HCG is mainly determined by its dimensions and thus remains relatively unchanged when d is varied. These two degrees of freedom (HCG dimensions and core size d) allow us to find a highly reflective HCG design with the large phase dispersion needed to achieve low-loss slow light. In Figure 3. 3 (a)-(c), we show the HCG ω - k_z curves overlapping with a background representing the HCG's reflectivity. When the HCG-HCW dispersion curves intersect with the HCG's high reflectivity regions (shown in red), the mode will be strongly confined inside the hollow core by the HCG reflector. This leads to low loss propagation. Figure 3. 3 (a)-(c) serves as a graphical design example that shows how we decrease the core size from $3\mu\text{m}$ to $1\mu\text{m}$ in order to shift the first order ω - k_z curve

flat and align it with the HCG design for a highly reflective HCG. HCG dimensions in these cases are the same.

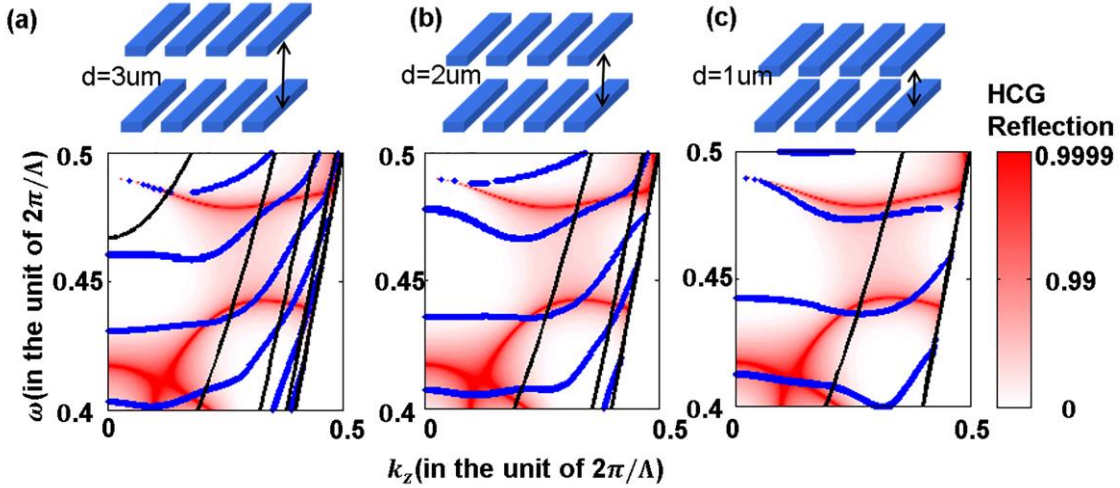


Figure 3. 3 The optimization of the waveguide loss and reduced group velocity by changing the core size d . The background color indicates the reflection of the HCG reflectors. When the ω - β intersects with the red region, the mode inside the hollow core is bounded by the HCG reflectors. (a) ω - β line for a HCG-HCW with core size $d = 3\mu\text{m}$ (b) core size $d = 2\mu\text{m}$ (c) core size $d = 1\mu\text{m}$.

Fundamental mode inside a $100\mu\text{m}$ length waveguide operating at optimized design region in Figure 3. 3 (c) is shown in Figure 3. 4. Light (intensity shown as red) is travelling inside the air core bounded by the two HCG reflectors (shown as white dashed line). Figure 3. 5 (a) shows the calculated loss, group index and group velocity dispersion as functions of frequency. The waveguide has a bandwidth over 120 GHz with loss $<0.1\text{ dB/cm}$ and group index ~ 100 . Pulse propagation simulation using FDTD method is shown in Figure 3. 5 (b), in which a 3ps pulse is launched into the waveguide. The pulse shape and position are monitored along the propagation direction at different time slices. Minor pulse shape dispersion is observed after $100\mu\text{m}$ propagation, indicating a small second-order dispersion. The waveguide dimensions for this design are: HCG period $0.77\mu\text{m}$, duty cycle ~ 0.5 , HCG thickness $1.51\mu\text{m}$ and air core size $d = 1.1\mu\text{m}$.

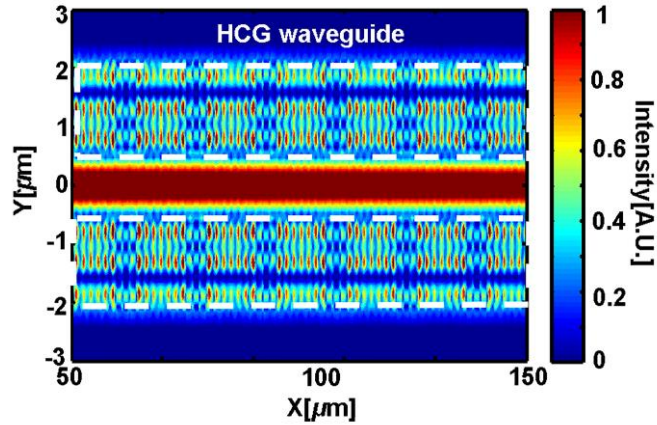


Figure 3. 4 FDTD simulation for 2D HCG waveguide operating with fundamental mode. White dashed line illustrates the HCG waveguide region. Light is mainly confined inside the hollow core.

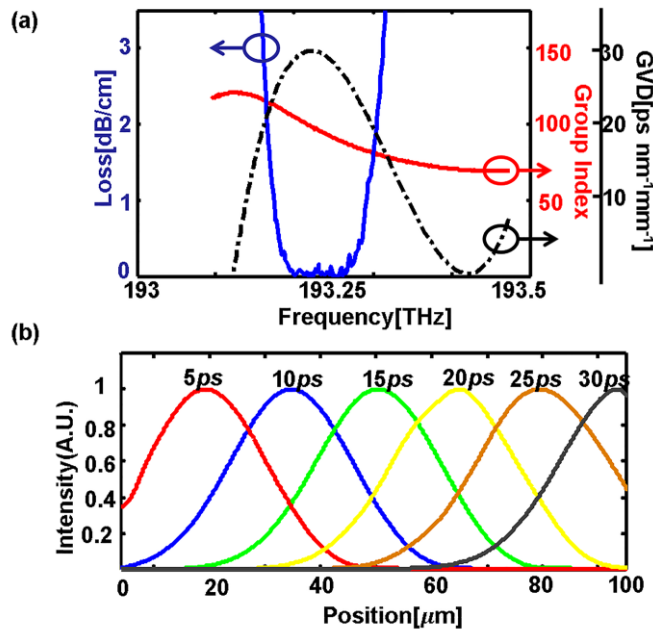


Figure 3. 5 FDTD simulation for 2D HCG waveguide. (a) Loss, group index and group dispersion analysis for the 2D HCG-HCW. Within a bandwidth of 120GHz, the loss is $< 0.1\text{dB/cm}$ and group delay is >100 (b) 5ps pulse propagation along the waveguide at different time slices.

3.4 Three Dimensional HCG-HCW: Wave Guiding and Slow Light

The 2D HCG-HCW shows great potential for low-loss chip-scale slow light devices. However, lateral confinement is needed for practical applications. Here we investigate a novel 3D HCG-HCW structure, where the HCG provides both lateral and transverse confinement. Figure 3. 6 (a) shows a schematic for our waveguide structure. It consists of a series of Si frames, looking like a “cage” for light. As we can see, the HCG “cage” waveguide has a periodic structure along the propagation direction. Thus, the traditional FEM (Finite Element Method) mode solver for waveguide eigenmode analysis cannot be applied here, as FEM requires the structure to be uniform along the propagation direction. Therefore, we introduce a simple method here for achieving a better understanding and also for providing intuitive design guidance. To simplify the problem, we start with a large hollow core size: Light propagating inside a large waveguide core hits the HCG at a nearly glazing angle; in this case, the HCG reflection phase is almost π . Under these two assumptions, we can use the following two equations to model the light inside the waveguide:

$$k_x d + \pi = m\pi \quad (3.5a)$$

$$k_y d + \pi = n\pi \quad (3.5b)$$

Then the effective angles for the guided mode can be seen as:

$$\begin{aligned} \cos\theta &= k_y/k_0 & \cos\theta' &= k_x/k_0 \\ \tan\phi &= \frac{k_x}{k_z} & \tan\phi' &= k_x/k_z \end{aligned} \quad (3.6)$$

where (θ, ϕ) are the effective angles for the light incident upon top and bottom gratings, and (θ', ϕ') are the effective angles for the confined light incident upon left and right gratings. The HCGs are then designed to be highly reflective at these angles. In Eqn. (3.5), m and n represent mode number in the x and y directions, respectively.

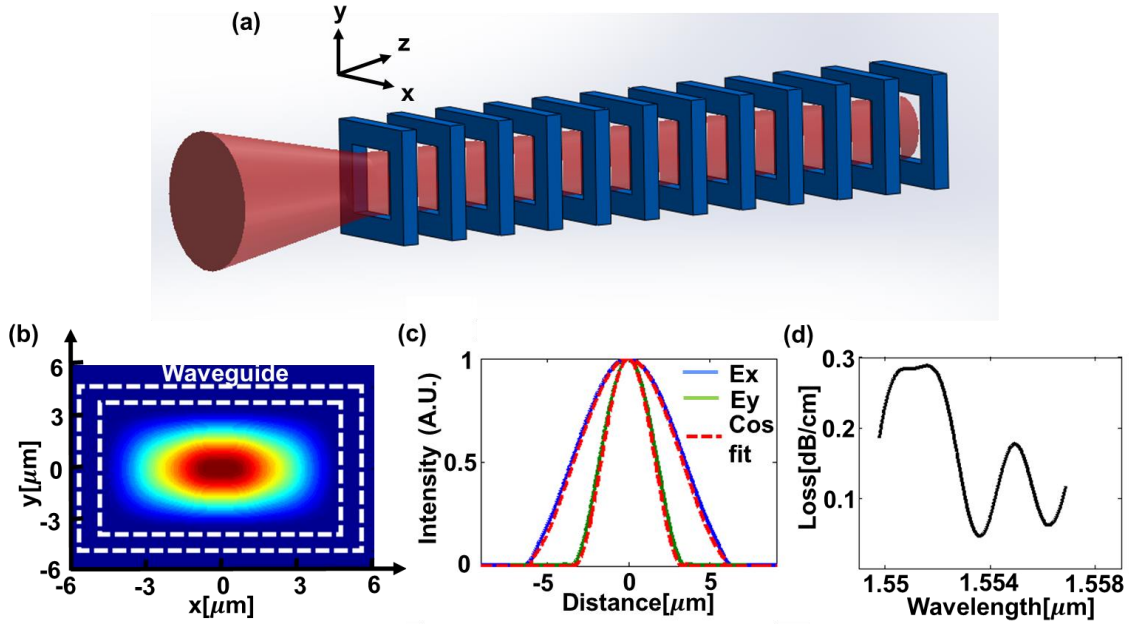


Figure 3. 6 (a) The schematic for 3D “cage” HCG-HCW. (b) The mode profile at the cross section of the waveguide with core size $10\mu\text{m} \times 8\mu\text{m}$. The white box indicates the area of Si grating. (c) The beam profile in the lateral and transverse directions. The cosine shape of the profile, resembling that of a metal waveguide, indicates that the mode is not formed by index guiding. E_x and E_y are intensity profiles along the x and y directions in (a). (d) Loss spectrum for HCG “cage” waveguide with a $10\mu\text{m} \times 8\mu\text{m}$ core. Lowest loss can be below 0.05dB/cm .

We start with core size $d_x = 10\mu\text{m}$ and $d_y = 8\mu\text{m}$ (roughly matching fiber core size). Then, the grating parameters are calculated for high reflection under the incident angles from Eqn. (3.5) and (3.6), as following: period $\Lambda = 700\text{nm}$, duty cycle $\eta = 45.28\%$, top-bottom grating thickness $t_g = 400\text{nm}$ and left-right grating thickness $t_g = 600\text{nm}$. These parameters lead to a low loss waveguide operating with fundamental mode. FDTD simulation is performed to verify the results. In Figure 3. 6 (b), we show the intrinsic mode supported by the “cage” 3D HCG-HCW. White dashed lines indicate the boundary of the Si frame. The majority of the guided light is tightly confined inside the air core by HCG reflection. Beam profiles in the X and Y directions are shown in Figure 3. 6 (c) as E_x and E_y . The cosine shape of the profile indicates that that mode is guided by waveguide “wall” reflection instead of index difference. The net propagation loss is extracted by monitoring the transmission power at the beginning and the end of a $500\mu\text{m}$ length waveguide shown in the Figure 3. 6 (d). The lowest loss is less than 0.05dB/cm at around $1.554\mu\text{m}$ in FDTD simulation.

Next, we will investigate the slow light phenomenon inside the 3D HCG-HCW. In Figure 3. 7, we simulated the dispersion relation for a waveguide with a $1\mu\text{m} \times 6\mu\text{m}$ core size, grating period of $0.77\mu\text{m}$, duty cycle of ~ 0.49 , thickness for top grating of $1.15\mu\text{m}$ and thickness for side grating of $0.8\mu\text{m}$. A smaller core size is chosen here to achieve a

smaller group velocity due to the reason described in Chapter 3. 2. The figure is generated using FDTD simulation in the following way: dipoles with random orientations are put into the waveguide hollow core. Then one period of the waveguide is simulated with the Bloch boundary condition along the direction of propagation. Randomly positioned dipoles excite various modes inside the hollow core. After a sufficient decay time, only the modes supported by the waveguide (intrinsic waveguide modes) build up a strong field (shown as red in Figure 3. 7), and all other modes decay, leaving little intensity remaining (shown as white in Figure 3. 7). In this way, we can easily find the intrinsic modes for the 3D HCG-HCW. When the stable state is reached, only the intrinsic waveguide modes will build up. These modes are shown as red in Figure 3. 7. Black dashed lines highlight the deep red region and indicate the mode dispersion curves for different modes (1st to 3rd mode in the case we studied). Again, the black solid curve is the dispersion relation from an ideal metal waveguide with same core size shown for reference. This particular waveguide supports up to three modes in the frequency range we are showing here. However, by narrowing the frequency range, we can eliminate high order modes and maintain the fundamental mode operation.

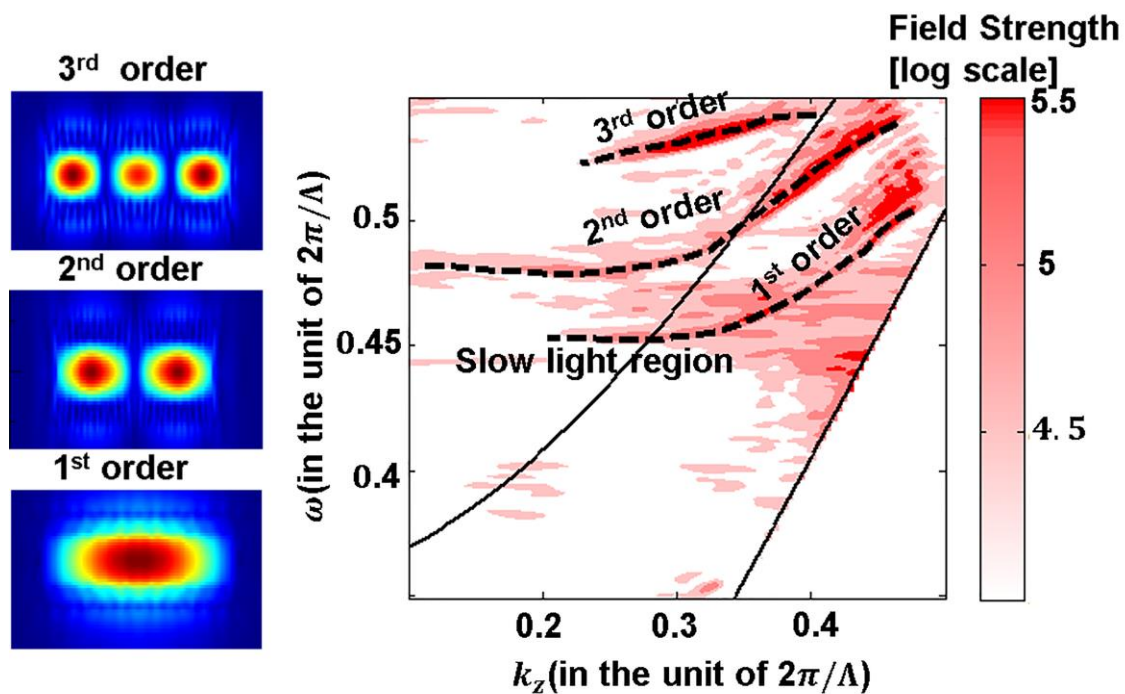


Figure 3. 7 The ω - k_z diagram for a “cage” waveguide with core size $1 \mu\text{m} \times 6 \mu\text{m}$. The background color indicates that the mode strength inside the waveguide excited by dipoles. Only the mode supported by the waveguide will build up intensity and is shown in red in the map. Black dashed lines highlight the deep red region and indicate the mode dispersion curve. Again, the black solid curve is the dispersion relation from a metal waveguide with same core size shown as reference.

Zooming into the tail of the 1st order mode dispersion curve, we see that the slope of the dispersion curve becomes more and more flat, indicating a reduced group velocity for the mode nearby. Tracing this mode and optimizing the grating thickness, we observe slow light inside a HCG “cage” waveguide for the first time. To verify the slow light performance inside this novel 3D HCG-HCW, we launch a time domain pulse into the waveguide. Then we trace this pulse in both the time and space domains. The intensity at the center line of the waveguide as function of time and position along propagation direction is shown in Figure 3. 8 (a). The bright line records how the pulse moves to different positions along the waveguide at different time slices. Thus, the slope of this bright line is the inverse of group velocity. Compared to the light’s speed in the air (shown as the red dashed light line), the group velocity for the slow light mode is reduced by 30 times inside the waveguide. We estimate ~6.5dB/cm loss by comparing the transmission power between the start and the end of the waveguide. At the current status, the light still suffers from loss and distortion while propagating along the waveguide. The pulse broadens and the peak power drops after 100 μm of propagation, as shown in Figure 3. 8 (b). However, we believe that there should not be a fundamental limit to loss. With fine tuning of the HCG parameters, one should be able to find a highly reflective design to minimize the waveguide loss. This is currently under further investigation.

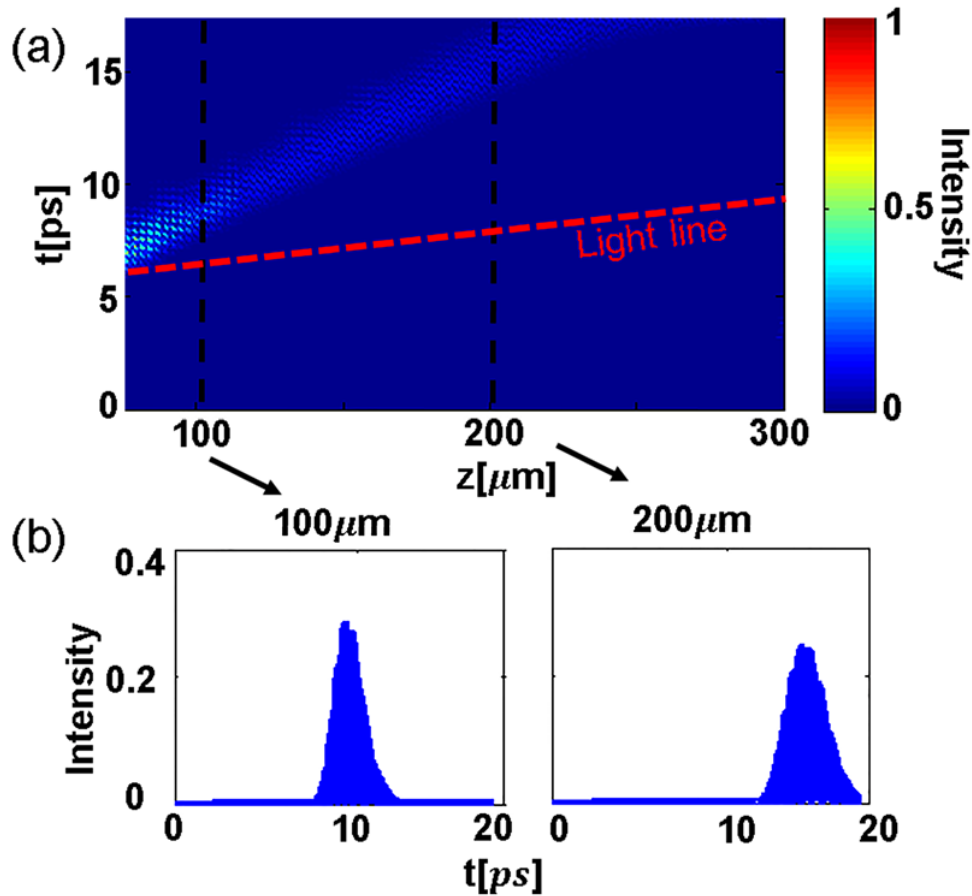


Figure 3. 8 Field intensity as a function of time and propagation distance. Red lines serves as reference, indicating the position of light line. (b) Pulse in time

domain monitored at $100\mu\text{m}$ and $200\mu\text{m}$. Group velocity can be calculated basing on the pulse propagation, $v_g \sim 1/30c$.

3.5 Device fabrication and characterization

The waveguide is fabricated in US Army Research Lab by RF photonics group led by Dr. Weimin Zhou [43]. The devices are fabricated on SOI wafer so that it has potential to be monolithically integrated with CMOS circuit to form more functional system. Cage waveguide is made in the Si layer and the Oxide underneath the device layer is then removed to suspend the waveguide structure to provide fully index contrast between four HCG reflector and the surrounding media.

Fabrication process starts with an etching mask (which is defined by e-beam lithography) on the top surface of the SOI wafer. The mask pattern comprises a series of parallel lines with separation equal to the HCG period, wherein a line width is equal to a HCG barwidth, where the center portion of the line represents the waveguide area shown in the figure below. Each line comprises of two wider portion, which are the positions of vertical HCG bar that will confine the light and serve as the cladding for the cage waveguide. After the top feature definition, modified Bosch etching process is used to create a deep vertical trench with a varying vertical profile. Three steps of modified Bosch etching are as followings: first directional etching will open the trend vertically and define the top HCG width. Secondly, a more isotropic etching will release the hollow core inside each frame. Thirdly, another directional etching etch through the Si layer vertically and define the bottom grating width. Oxide will be removed by HF at last step to fully release the cage Si structure. Fabrication steps are summarized in the figure shown below:

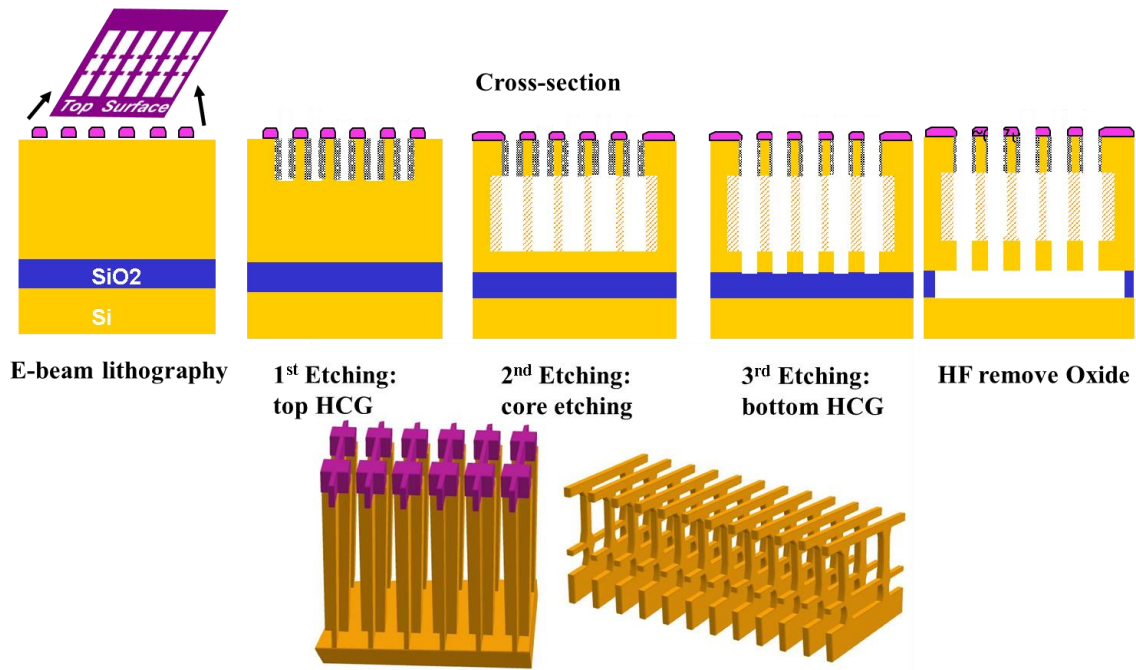


Figure 3. 9 Fabrication steps for cage waveguide. Reproduced from [43].

SEM images are taken and shown in the following figures. They serve as clear evidence of the successfully resolved features. Five waveguides are fabricated side by side to form an array.

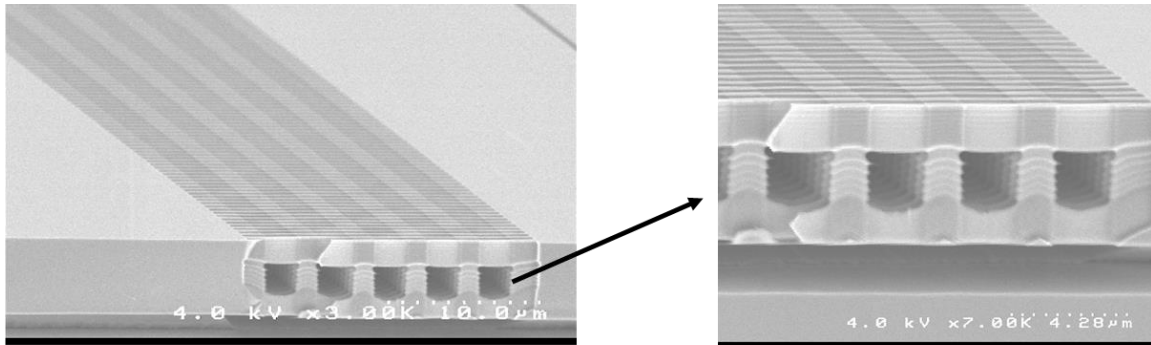


Figure 3. 10 The SEM images of the fabricated 3D cage waveguide. Five identical waveguides are fabricated side by side to form a compact array [43].

The waveguide sample is then tested. A free-space microscope objective lens is used to couple a tunable laser (centered at ~1550nm) in and out of the waveguide. A beam splitter is used to observe the output image with an IR camera. The following figure shows the mode pattern at the output facet of a 11mm long waveguide. We plot the waveguide per unit length by taking the average value loss between the normalized intensity measured from

the 5 identical waveguides side by side inside one array. Figure 3. 11 (b) shows that lowest loss is occurring at 1550nm with loss slightly less than 2dB/cm.

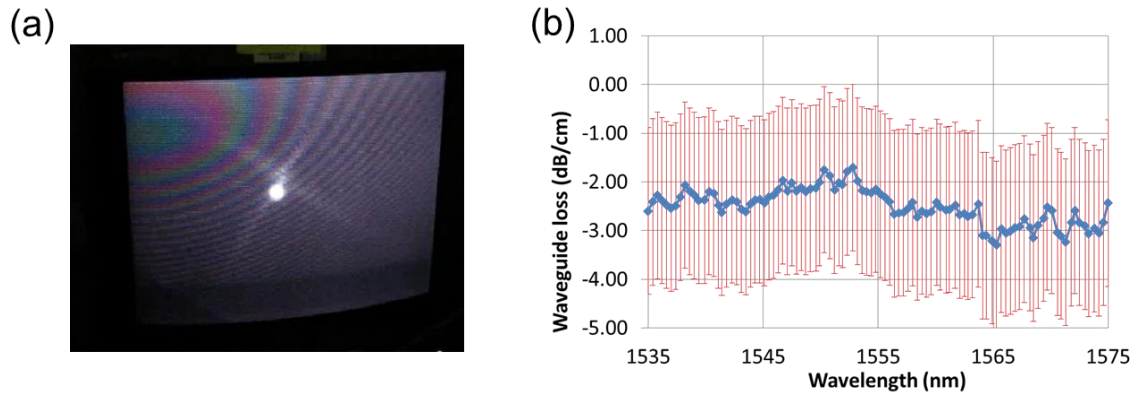


Figure 3. 11 (a) Mode pattern taken at the output facet of an 11mm long waveguide by a IR camera. (b) Loss measurement for the same waveguide in the wavelength range 1535nm to 1575nm [43].

Preliminary test on group delay is also carried on. Pulse propagation inside air and waveguide are compared to get group delay, and then group velocity will be extracted by knowing the length of propagation distance. ~260ps delay is observed between pulse inside two media, which indicates a group delay $n_g \sim 10$. Input laser is set at 1552.8nm, at which waveguide loss is minimum.

From SEM image shown in Figure 3. 10, we can see that etching profile for top and bottom HCG are more close to a parabolic shape instead of rectangular bars in design. Also, grating duty cycle (defined as grating barwidth divided by grating period) tends to be smaller than the design value. We believe with optimized processing recipe, we can further improve the performance (loss and group delay) and get results more close to theory predication.

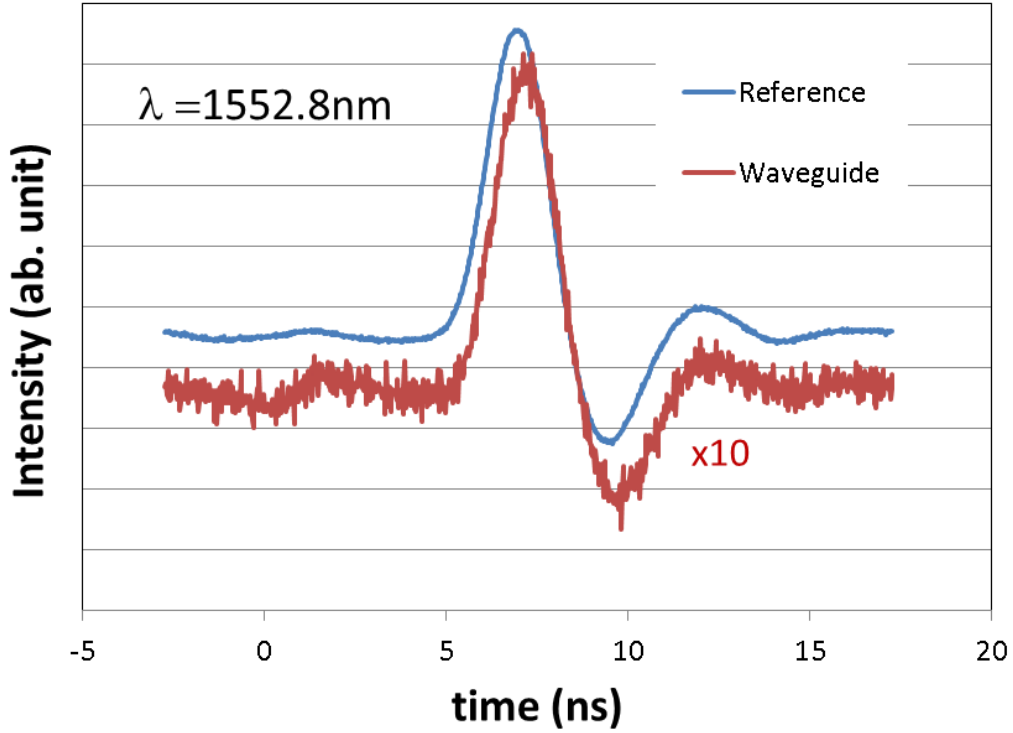


Figure 3. 12 Pulse propagation inside air (blue) and slow light hollow HCG cage waveguide (red). ~260ps delay is observed, which indicates group delay $n_g \sim 10$ is reached inside our device. (Lase wavelength is centered at 1552.8nm) [43].

3.6 Application in gas sensing

This novel HCG- HCW design is a strong candidate for use in compact, low-power, rapid integrated gas sensor applications (Figure 3. 13). Absorption spectroscopy is a powerful technique for measuring trace concentrations of gaseous species. The quantitative absorption measurement is described by Beer's Law [32]:

$$I = I_0 \times \exp(-\gamma\alpha L) \quad (3.7)$$

where I_0 is the initial laser intensity, α is the absorption coefficient of the gas, L is the optical interaction length, and γ is the absorption factor that is determined by the light-matter interaction. L must be large enough to achieve a suitable sensitivity of measured I/I_0 . In a slow light system, γ can be written as:

$$\gamma = f \times \frac{c/n}{v_g} \quad (3.8)$$

where c is the velocity of light, v_g is the group velocity and f is the fill factor, which denotes the fraction of the optical filed overlapping with gas. In the previous sections, we have already shown that an HCG-HCW provides a large gas/light overlapping (namely f

~ 1) and a small $v_g(\sim 30)$. These features may potentially enable a 30x reduction in the required absorption length L and a more compact lab-on-chip system.

Another superior advantage of the HCG-HCW over other conventional HCWs is rapid dynamic detection. Gaseous molecules can flow in and out of the waveguide from the side without latency, instead of being pushed from one end of the waveguide to the other. This dramatically reduces the response time in gas detection. With Fick's first law, the diffusion length (a measure of the distance l that the concentration has propagated over diffusion in time t) can be derived to be proportional to \sqrt{Dt} , where D is the diffusion coefficient. Thus t is proportional to l^2/D . In a traditional HCW gas sensing system (with length L and core size d), the diffusion time t can be approximated by L^2/D . However, in HCG-HCW, the diffusion time is reduced to d^2/D . Thus it is L^2/d^2 times faster for gas to fully diffuse into HCG-HCW than the conventional HCW. Furthermore, this ratio can be easily larger than 8 orders of magnitude with the typical L on the order of millimeters and d on the order of micrometers. Figure 3. 13 shows a schematic of using HCG-HCW as a platform for gas sensing.

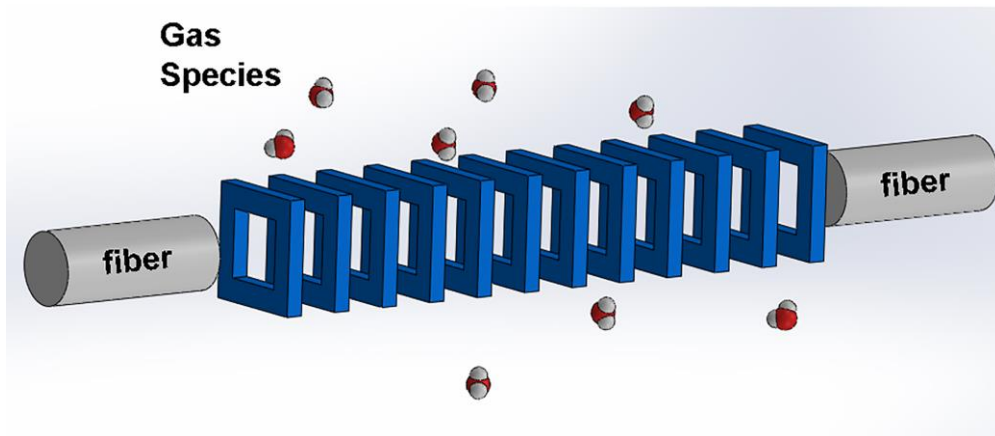


Figure 3. 13 Schematic of HCG-HCW as a gas sensor. Required length is reduced by factor of group index. Detection speed (limited by diffusion time) is greatly improved due to the novel structure.

3.7 Conclusion

In this Chapter, we presented a novel low-loss slow light HCW using HCG reflectors. Reduced group velocity is produced by the phase dispersion from the HCG reflectors. Since the dispersion is relatively independent of the HCG's reflectivity within a large design window, we are able to optimize the loss and slow down factor separately to obtain a low loss and low group velocity at the same time. For a 2D HCG-HCW, slow light with loss $< 0.1\text{dB/cm}$, group velocity $< c/80$ and bandwidth $> 120\text{ GHz}$ is obtained and confirmed using FDTD simulation. A novel 3D "cage" HCG-HCW is also presented. FDTD simulation demonstrates that in such waveguide, light is confined by reflective

waveguide 'walls' instead of index difference. A 3D waveguide design with loss as low as 0.05dB/cm is obtained for a core size of about (10 μm x 8 μm). Slow light phenomena is found in a smaller core size design (1 μm x 6 μm) with different grating dimensions. A slowing down region with group velocity $\sim c/30$ is found and simulated using FDTD. Low loss design is currently under further investigation. With all these desirable attributes, HCG-HCWs show great promise for integration with many on-chip systems used in applications such as compact and rapid integrated gas sensor

Chapter 4 High Contrast Grating Resonator and Its Application in Optical Bio-sensing and Nonlinear Optics

4.1 Introduction

Point of care devices (POC) [44-52] offer considerable advantages over conventional biomarker detection technologies for disease biomarkers that are often slow, difficult to automate, and require large quantities of reagents and require bulky and expensive instrumentation that make them difficult to use in the field. POC diagnostic devices on the other hand are rapid, require minimal quantities of detection reagents and can be produced at low-cost. POC systems typically use colorimetry or fluorescence signals to readout the amount or presence of a target biomarker associated with cancer, neurologic and cardiovascular disease. Since diagnostic tests account for an appreciable percentage of the national healthcare budget, the demand for POC devices will increase, and indeed companies such as Theranos are already implementing decentralized strategies for low-cost analyses of biomarkers within patient samples [53].

Another trend in the design of next generation POC devices is to move away from enzyme linked immune assays (ELISA) formats to label-free detection formats. This is a necessary trend as antibody-enzyme conjugates are heterogeneous and have significant batch-to-batch variation, the conjugates exhibit reduced affinities for their targets and the requirement for multiple incubation and wash-steps increases the complexity of the device and the time to complete an assay. Optical biosensors, using light as probe, have been demonstrated to have sensitive detection and negligible influence on the target caused by detection. High throughput label-free optical sensing techniques have been described for POC devices including those based on surface plasmon resonance [48], photonic crystals [50], integrated micro-cavity [51], and metal nanohole arrays [52]. These devices provide sensitive detection however require expensive e-beam lithography while the need for exact optical alignments and specialized personnel limits their potential in the field.

We have developed an alternate and novel label-free biosensor that employs a high-contrast grating (HCG) resonator (Figure 4. 1 (a), (b)). The high-contrast grating structure generates strong and specific resonances that are sensitive to surface properties. Light is surface-normally coupled to the device with high coupling efficiency and confined inside a single grating layer, which serves as an optical cavity. When bio-molecules bind to the HCG surface, the resonance wavelength red-shifts due to the increase in the effective optical length of the cavity (Figure 4. 1 (c)). These devices are produced at low cost and en masse using standard DUV lithography (ASML 5500/300) and silicon reactive-ion etching (Lam

Research). The surface normal input of the probing light beam simplifies the optical alignment, and helps to maximize the accuracy of the measurement. Detection antibodies are coupled covalently to HCG surface providing a platform for rapid and specific detection of target antigens with a sensitivity that is relevant to clinical diagnosis.

In this chapter, HCG device is shown to be used to detect serum troponin I (cTnI), a component of the troponin complex in cardiac muscle [54]. Following myocardial infarction, damaged cardiac muscle cells release cTnI into the blood – the detection of cTnI in serum is a reliable and validated clinical marker of cardiac muscle tissue injury and stroke, which affect ~1 million people in the USA each year [55]. Because cTnI is present at low levels in the blood, most approved assays for serum cTnI use ELISA platforms. In this study we show how the HCG label-free detection platform can be used to detect cardiac cTnI in PBS and in serum rapidly and over the clinically relevant concentration range of 100 pg/ml to 80 μ g/ml.

4.2 HCG resonator design, fabrication and characterization

A detailed analysis of the design algorithm employed for the HGG resonator is described in Chapter 2 and also reference 10. For HCG devices used in this study, the period is 792nm, the bandwidth is 427nm and the grating thickness is 500nm. The devices are patterned onto a 6 inch silicon-on-insulator wafer using DUV lithography followed by silicon refractive ion etching, which are both standard processes in semiconductor manufacturing. A test array with thousands of single HCG resonators can be patterned during a single exposure, enabling low-cost and high-throughput production of devices. An SEM image of gratings within a single device is shown in Figure 4. 1 (b) and highlights the high quality nature of the fabrication process. Two steps fabrication are shown in Figure 4. 2, and we emphasize its simplicity and CMOS compatibility.

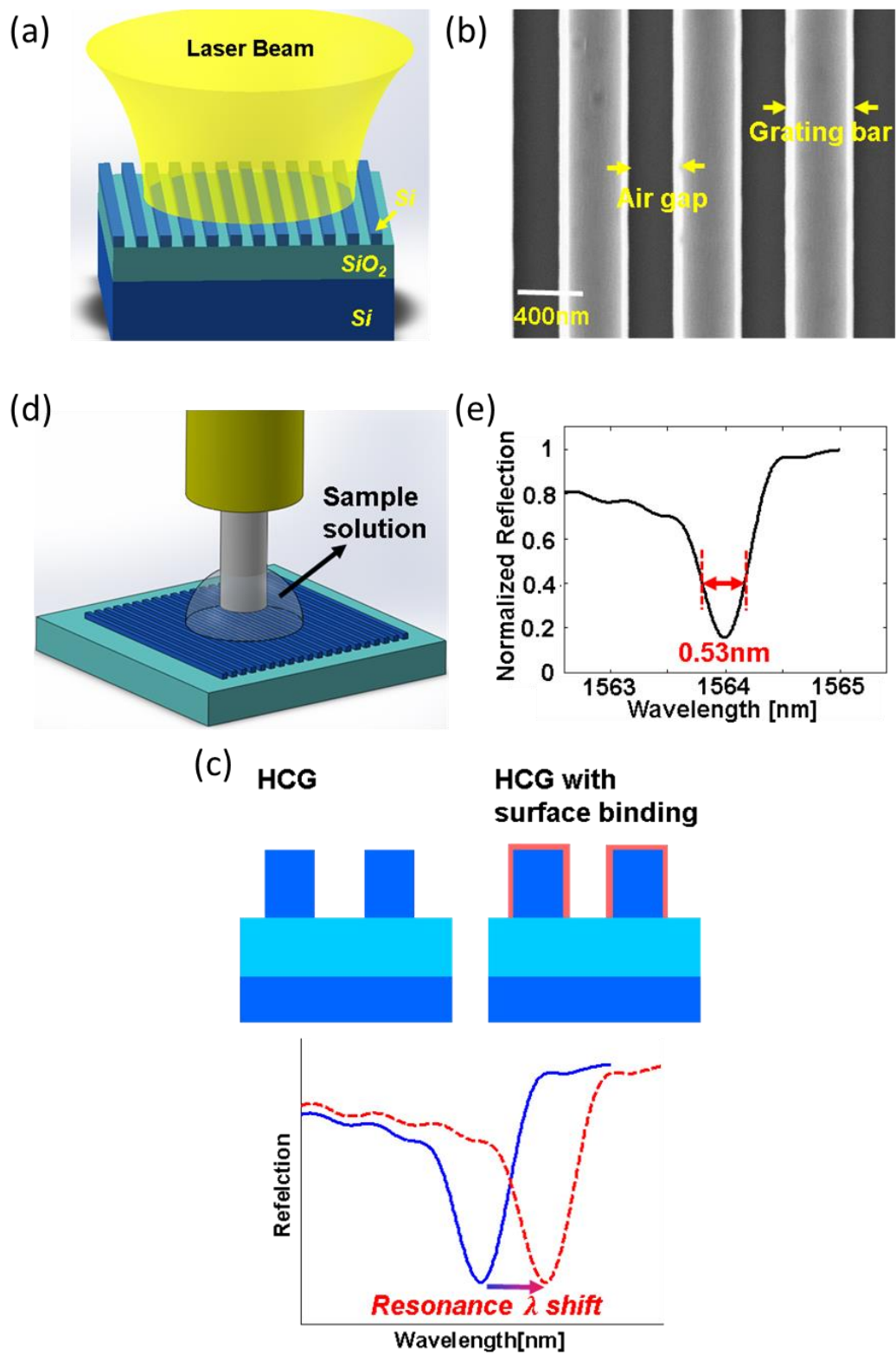


Figure 4. 1 High Contrast Grating Resonator as a label-free biosensing platform. (a) Schematic of a surface normal coupled high contrast grating (HCG) resonator.

(b) SEM image of gratings within a single fabricated HCG resonator. (c) Schematic of the principle of using HCG resonator as protein binding sensing platform. Red dashed curve shows resonance wavelength will red-shift due to the protein binding at HCG surface. (d) A single mode fiber probe is immersed in the fluid above the HCG surface to avoid surface reflections. (e) A reflection spectrum recorded for a device having the configuration schematized in (d). A tunable laser centered at 1550nm is used as excitation source and is run in a continuous sweeping mode. The reflection power is recorded in real time and is synchronized to laser sweeping rate.

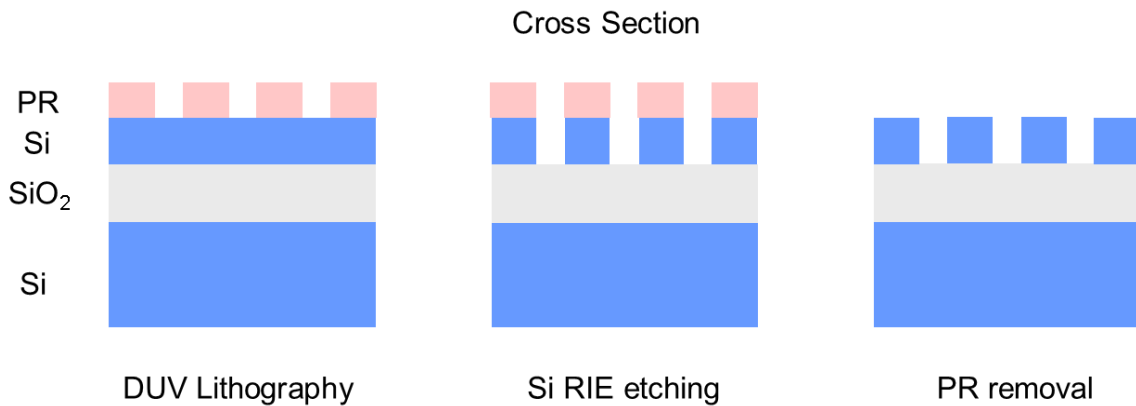


Figure 4. 2 Fabrication process for HCG resonator. Only two main steps are needed to generate an on-chip high Q HCG resonator, including optical lithography and Si RIE etching.

A single mode fiber is used to excite resonances inside the HCG sensor— in practice the fiber is simply adjusted above the surface of the HCG and does not require any precise optical alignment (Figure 4. 1 (d)). A tunable laser centered at 1550nm is used as the excitation and is set in a continuous sweeping mode between 1560nm and 1565nm at a rate of 40nm/sec. The power of the reflected light is recorded using a photodiode in real time and is synchronized to the laser sweep rate. The reflection spectrum obtained under fiber illumination of a HCG device is shown in Figure 4. 1 (e). The device has a quality factor measured at ~3000 with a center wavelength of 1564nm when immersed in phosphate buffered saline (PBS). Free space setup is shown in Figure 4. 3 (a), free space tunable laser, photodiode, beam splitter and objective are used in the measurement. We try to use as few as components to minimize the application cost. In Figure 4. 3 (b), we show a fiber-optic measurement setup. Single mode fiber is used as probe. Laser is coupled in from a tunable laser and coupled out to a fiber-based detector through a circulator. Fiber is used here to probe device under sample solution to avoid multi reflection from multiple surfaces.

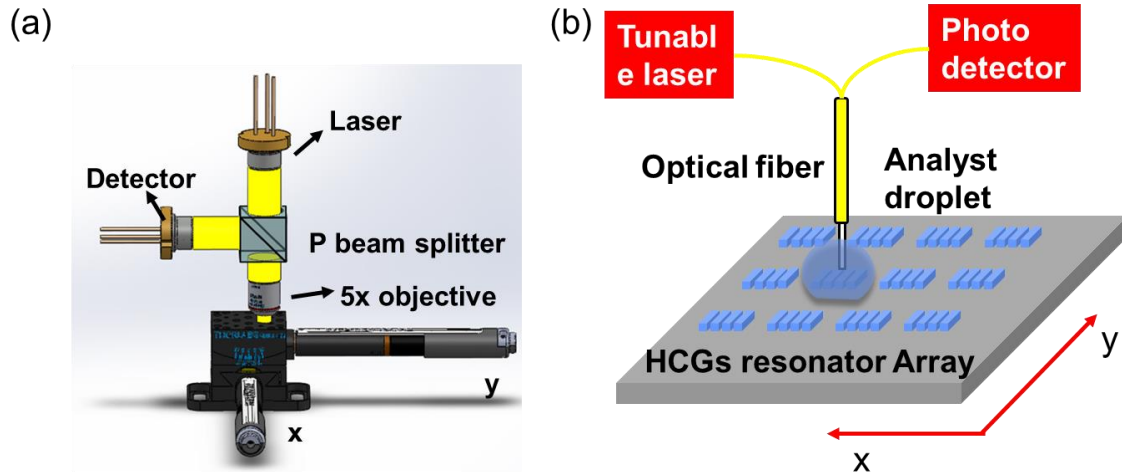


Figure 4. 3 (a) Free space measurement setup. Free space laser, detector, beam splitter and a 5x objective are used in the measurement. We try to use as few as components to minimize the application cost. (b) Fiber based measurement setup. Single mode fiber is used as probe. Laser is coupled in from a tunable laser and coupled out to a fiber-based detector through a circulator. Fiber is used here to probe device under sample solution to avoid the surface multiple reflection.

An important advantage of the HCG resonator over other on-chip resonance based devices is the ability to establish a unique pattern of resonance modes. A simulated mode pattern at resonance for an HCG resonator excited with a Gaussian beam of $\sim 10\mu\text{m}$ spot size (output from a single mode fiber) is shown in Figure 4. 4 (a). The top view of the resonance sliced in the center of resonator is shown in Figure 4. 4 (a). Efficient optical coupling of the input light to the HCG device is facilitated by the large mode overlap between the input Gaussian beam and resonance mode. The side view of the resonance inside one grating period of HCG is shown in Figure 4. 4 (b), which reveals a large portion of the resonance mode exists near the HCG surface. This feature results in a strong interaction between the resonant light and surface attached biomolecules.

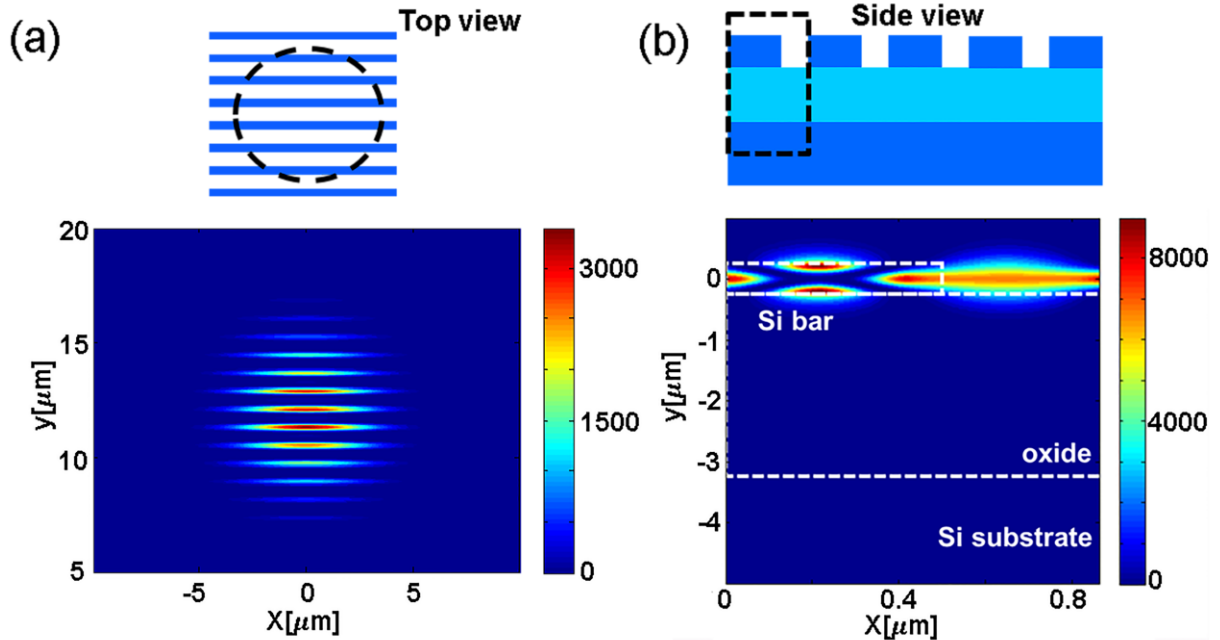


Figure 4. 4 HCG resonator mode pattern. (a) Top view of the resonance inside the HCG cavity excited by Gaussian beam with a $10\mu\text{m}$ spot size. A large mode overlap with the input beam contributes to a simple and efficient coupling of the input light. (b) Side view of the resonance (showing one period) inside the HCG cavity. The resonance is designed to have large mode exposure to surroundings, which contributes to the high sensitivity of the device.

4.3 Sensitivity of the HCG device to changes in refractive index

Quantitative measurements are used to evaluate the intrinsic sensitivity of the HCG device to a change in refractive index. First the sensor is covered uniformly with a liquid of known refractive index (RI), with solvents covering a RI range from 1.494 to 1.506. The results of these measurements are shown in Figure 4. 5 (a), and reveal that increases in RI shift the resonance wavelength to the red. The shift in wavelength as a function of the change in RI is plotted in Figure 4. 5 (b). These plot reveals a linear relationship between ΔRI and red-shift and show our HCG sensors have a RI sensitivity (RIS) of 418nm/RIU, which is higher than those measured for other dielectric structures [50]. The high sensitivity of the HCG is attributed to the special resonance mode pattern of the HCG resonator, which was described in the previous section.

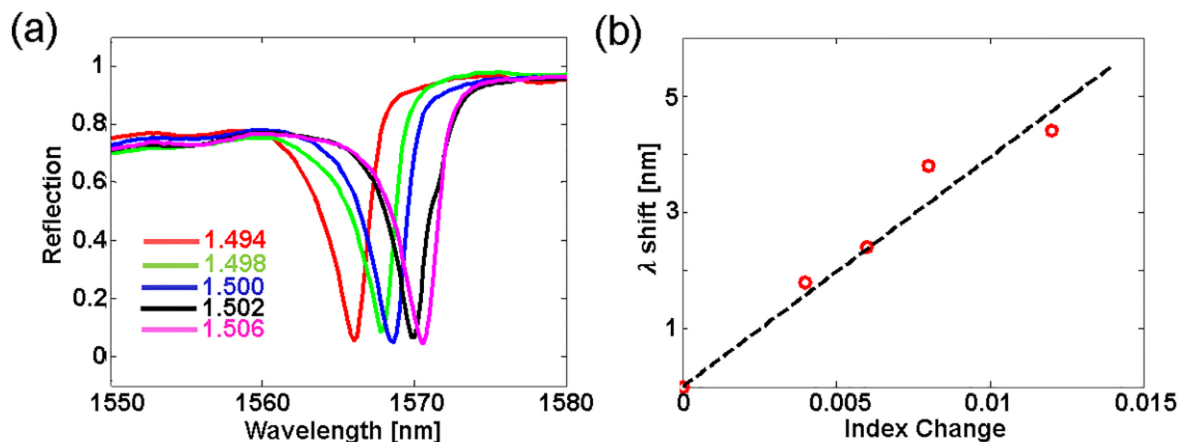


Figure 4. 5 Refractive Index Sensing. (a) Reflection spectra when HCG resonator is immersed in liquids with different refractive index ranging from 1.494 to 1.506. (b) Resonance wavelength as function of the change in refractive index.

4.4 Quantitative analysis of antibody-antigen interactions using HCG devices

To characterize the sensitivity of the HCG sensor in detecting target antigens, we tested a complementary antibody-antigen pair of unlabeled IgG from rabbit serum (I5006, Sigma) as the antigen, and anti-rabbit IgG produced in goat (R2004, Sigma) as the detection antibody. A schematic of binding assay platform is shown in Figure 4. 6 (a) and (b). First the antibody is immobilized covalently on the sensor surface using a maleimide-thiol reaction. Specifically, maleimide groups are introduced to the antibody by treating the antibody (1mg/ml) with 100 μ M maleimidobenzoic acid succinimide ester (MBS, Sigma) in PBS for 2hrs at room temperature. The mixture is then passed over a PD-10 column in PBS to remove unlabeled MBS and fractions containing the MBS-antibody conjugate are pooled. The surface of the Si-sensor is thiol-silanized using a fresh 5% solution of (3-Mercaptopropyl) trimethoxysilane (MPTMS) in IPA for 1hr. After washing with PBS the surface is treated with a 1mg/ml of the MBS-antibody. The reaction between the MBS-antibody conjugate and surface thiol groups on the HCG results in a stable thioether bond. After an incubation period of two hours, the surface is washed with PBS, and a blocking buffer containing 3% BSA is applied to the surface to reduce the non-specific binding of serum proteins. Before adding the target antigen, the spectral response of the sensor is recorded and the resonance wavelength for this measurement assigned as the reference. Next antigen solutions (200 μ l) at different concentrations ranging from 0.1ng/ml to 1mg/ml are added separately onto the HCG surface and the spectra recorded after each addition of antigen.

The first set of binding studies presented in Figure 4. 6 (c) and (d) focus on label-free recording of the interaction between surface-bound goat anti-rabbit IgG and rabbit IgG. A standard curve for the device is generated by recording the spectral shift for different

concentrations of the purified antigen in PBS; three parallel titrations are performed for each antigen concentration to improve the precision of the measurement. The standard curve shows a monotonic relationship for antigen concentration with the shift of wavelength. The interaction between the antibody and antigen is conducted over a 1000-fold range of antigen concentration. The surface antibody is seen to saturate at around 3 $\mu\text{g/ml}$, with the lowest detectable concentration being 100pg/ml, which results in a wavelength shift of 60pm (red trace of Figure 4. 6 (d)). A negative control experiment is carried out using a non-complementary antigen, namely anti-rabbit IgG and mouse IgG, which is shown in the blue line of Figure 4. 6 (d). This wavelength shift for the control sample is minimal compared to the complementary rabbit IgG/anti-rabbit IgG pair. The detection of the same antibody-antigen complex performs equally well for antigens diluted in serum rather than PBS. Three concentrations of the rabbit IgG in serum at 2ng/ml, 10ng/ml and 80ng/ml are found to lie on the same standard curve recorded for rabbit IgG in PBS (black triangles in Figure 4. 6 (d)). The calculated concentrations of the rabbit serum IgG antigens derived from the spectral shift on the standard curve correspond very well with the actual concentrations. The serum studies also show that non-specific binding of serum proteins including rabbit IgG on the HCG surface is negligible.

The time dependence of rabbit IgG binding to the anti-rabbit IgG labeled surface is recorded to demonstrate the ability of the device to quantify on-rates of antigen-binding (and the of-rate for unbinding) In these kinetic studies, the response is measured continuously following separate additions of the antigen at 4 different concentrations. As shown in Figure 4. 6 (c), the response changes with time, with 95% of the equilibrium value being reached at ~200 seconds after exposing the antibody surface to antigen solution at the four indicated concentrations (Figure 4(c)). The change in signal is exponential with a time constant of ~50 seconds, which being typical of antibody-antigen pairs, allows us to read-out the device for an antigen within 5 minutes.

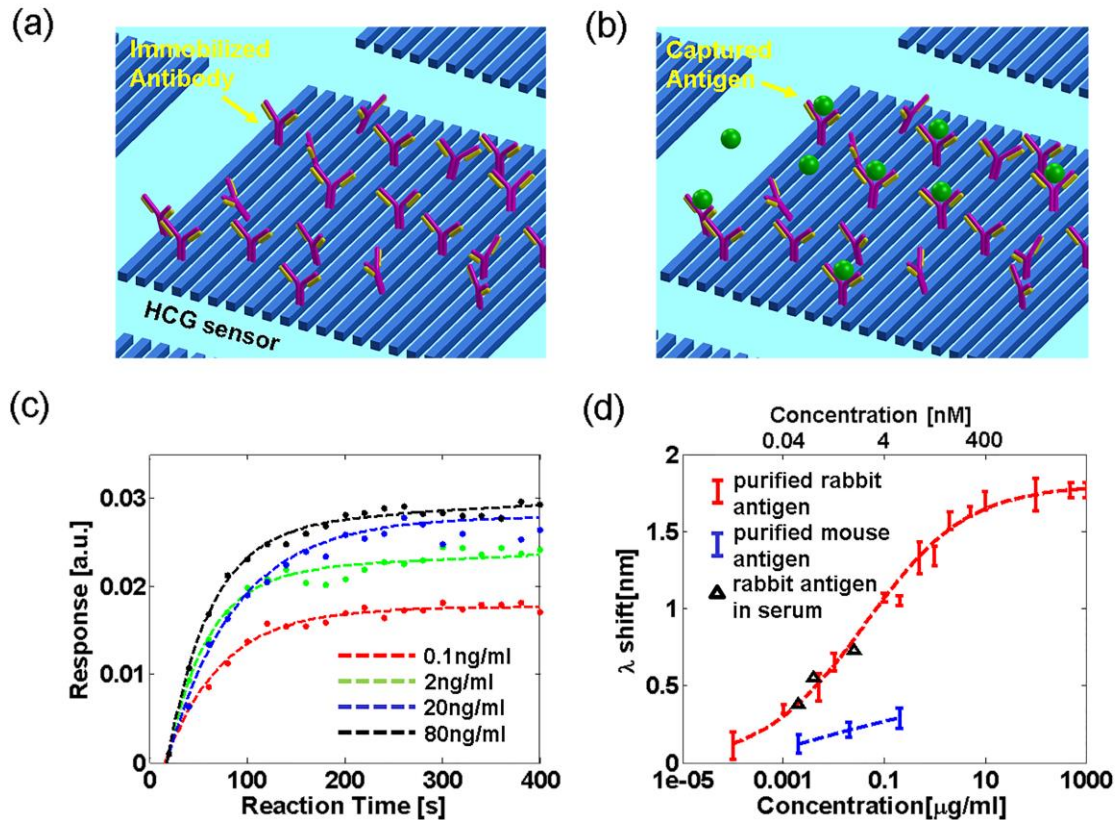


Figure 4. 6 Antigen binding assays on the HCG device. (a),(b) Schematic of using HCG resonator for a label-free protein binding assay. (c) Real time recording of the interaction of surface bound goat anti-rabbit IgG for different concentrations of antigen (rabbit IgG). The dashed lines are the corresponding fits to these curves. (d) Red dots show the resonance wavelength shift corresponding to different purified rabbit IgG concentrations added to a HCG resonator surface-coated with anti-rabbit IgG. The red dashed line is the fit to measured data. Blue dots show the result of non-specific test indicating that mouse IgG/anti-rabbit IgG having a much lower shift in the resonance wavelength. The black triangles show the response of the HCG sensor to the addition of rabbit IgG dissolved in goat serum. The bars indicate the error range for the 3 measurements.

4.5 Quantitative analysis of Troponin I

cTnI is a component of the troponin complex that regulates cardiac muscle contraction. cTnI is released from cardiac muscle into the blood after a stroke and is widely used as a serum biomarker to diagnose heart disease or stroke [54]. In our study, purified human cTnI [54] is detected in PBS and serum using a commercial anti-Troponin antibody specific for an epitope mapping between amino acids 86-209 at the C-terminus of Troponin I-C of human origin (sc-133117, SCBT). The antibody is covalently linked to the HCG surface using the maleimide-thiol coupling strategy described earlier. The standard curve for cTnI binding to anti-cTnI on the HCG surface is generated by measuring the change in the

resonance wavelength for different dilutions of purified cTnI in PBS ranging from 0.1ng/ml to 80 μ g/ml (Figure 4. 7 (a)). Next purified cTnI is diluted in fetal bovine serum and measured on the HCG device at 4 defined concentrations. The concentrations of cTnI in the serum samples, which are calculated by relating the spectral shift measurement of the serum sample to the standard curve, agree very well with actual concentrations of the biomarker (black triangles in Figure 4. 7 (a)) and fall within the range of commercial assays for serum cTnI.

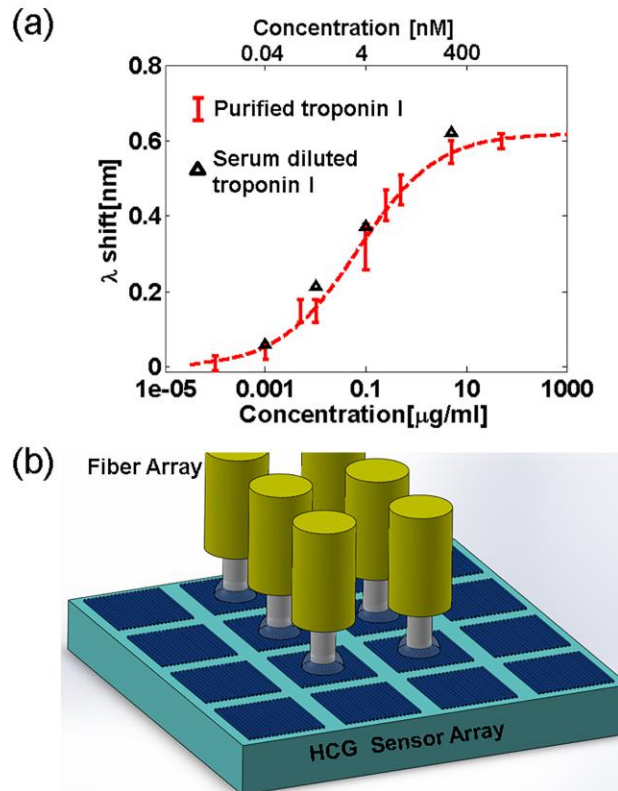


Figure 4. 7 (a) Measurement results for troponin I molecule inside PBS (red dots) and serum (black triangles). The bars indicate the error range over 3 measurements. (b) HCG sensor array combined with fiber array for high throughput screening.

4.5 Discussion

Clinical diagnosis of diseased states requires robust, sensitive, accurate and specific detection of the complexes between validated antibodies and their antigen targets. POC devices usually employ the ELISA format to detect low abundant biomarkers in serum. The ELISA technique however is slow, primarily because of multi-step processing of the sample while the use of heterogeneous antibody-enzyme conjugates introduces batch-to-batch variability in performance. In this study a novel high contrast grating (HCG) resonator is employed as part of a label-free platform to quantify interactions between specific antibody-antigen pairs. The low cost, label-free device is simple to construct and

allows for sensitive and robust, surface-based detection formats to quantify disease biomarkers in serum. Our studies show that cTnI can be detected in a mock serum sample with a sensitivity of 100pg/ml in less than 5 minutes – this level of detection falls well within the range of serum cTnI levels associated with stroke with ~0.4ng/ml being widely used as the cutoff [56]. The simple design of the HCG sensor, which is based on a standard silicon manufacturing process enables compact integration and up to 10000 sensors can be fabricated on a single 1cm² chip with integrated microfluidic and electronic systems. Furthermore, the surface-normal fiber detection format of the device reduces the need for constant and precise optical alignment. A simple extension of the HCG platform described in this study would be to combine a HCG sensor array with a fiber array, as shown in Figure 4. 7 (b). This new platform could facilitate high-speed screening of thousands of samples at a drastically reduced cost compared to ELISA based systems. Finally, the HCG label-free biosensor is shown to perform well in a mock clinical diagnosis of cTnI in blood. Moreover, the HCG format generates one the fastest quantitative readouts of cTnI in serum samples over a concentration range that is relevant for clinical diagnosis of cardiac infarction.

4.6 HCG assisted SPP Flexible Biosensor

4.6.1 Introduction

The biological and chemical sensing on the ubiquitous surface is very important for many applications, such as medical treatment, pharmaceuticals, environment sensing, security, etc. As we discussed in Chapter 4.1, commercial microarrays mainly rely on detecting labeled molecules. Labeling process complicates the sample preparation, detection process, and also may change the molecule's binding properties, which will then leads to compromise of detection accuracy and reliability. Here, we propose a novel optical label free sensor based on HCG coupled with surface plasmon polariton (SPP), which can provide both sensitive detection and flexibility to meet the requirement in many wearable devices and point of care situation.

4.6.2 Optical Sensor Design

Surface plasmon polariton (SPP) is a transverse magnetic surface electromagnetic excitation that propagates along the interface between a metal and a dielectric medium. Mode field is concentrated on the metal surface to result in a sensitive detection to the change on or above the metal surface. High contrast grating (HCG) has been shown to possess extraordinary property of broadband reflector and high Q resonance. Here we use HCG to assist the excitation of surface plasmon polariton and then use the concentrated optical field near the metal surface to perform chemical, gas and bio-sensing.

The schematic of our optical sensor is illustrated in the following Figure 4. 8. The design consists 3 key parts: (1) high contrast grating, used to do phase matching between the input

light and surface plasmon prartiton and assist the SPP mode to excite. (2) Thin film of metal, on the surface of which SPP mode is excited and sensing is performed. (3) Flexible carriers are used to support the sensor structure and build up a flexible platform.

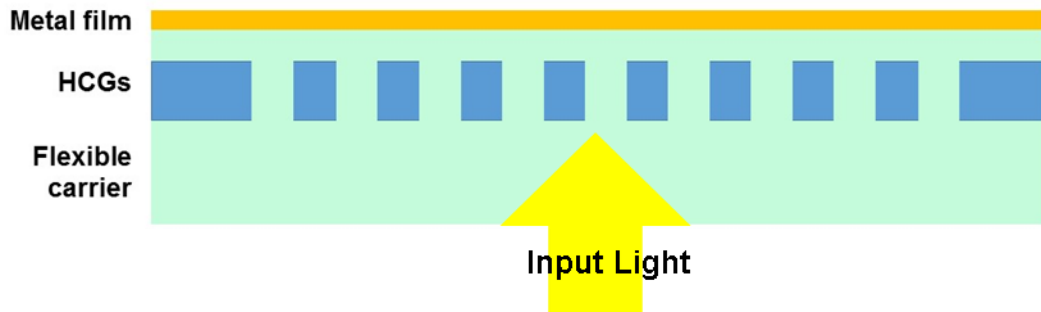


Figure 4. 8 Schematic of HCG-assisted SPP sensor

The design principle of the optical sensor can be illustrated using Figure 4. 9 (a). In the figure, reflection is plotted as a function of grating thickness and operation wavelength. The period of the grating is chosen when $\frac{\lambda}{\Lambda} = n_{\text{eff}}$, where λ is the working wavelength, Λ is the grating period and n_{eff} is the effective index of the SPP mode. Thickness of the grating is chosen from the Figure 4. 9 (a) to optimize the resonance effect. FDTD simulation in Figure 4. 10 (a) shows the mode pattern of SPP mode. Intensity is enhanced by ~ 100 times at the metal surface to improve the surface sensitivity. In Figure 4. 10 (b), reflection as function of wavelength and grating thickness. Two resonance lines indicate SPP resonance with surface binding thickness $t_b = 0\text{nm}$ and 20nm . A large tolerance on the grating thickness give us a very large design and fabrication tolerance space.

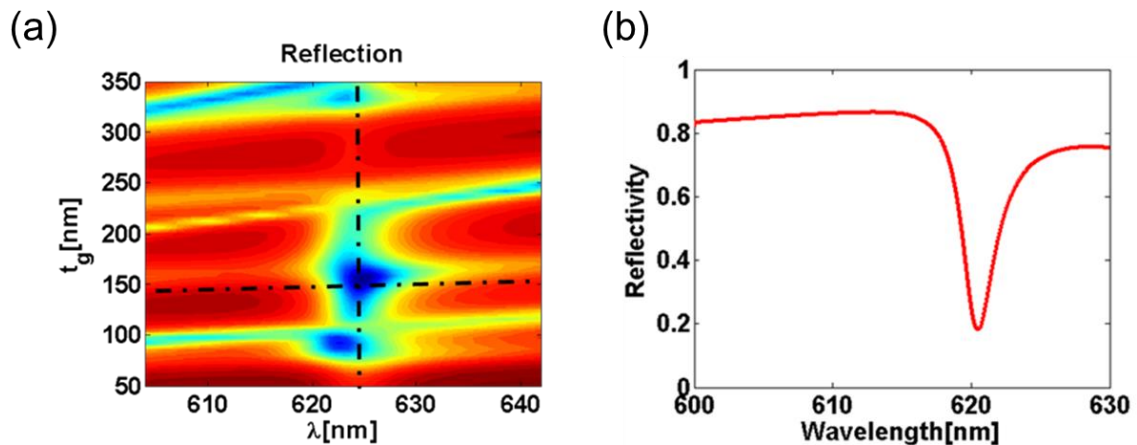


Figure 4. 9 (a) Reflection as function of working wavelength and grating thickness. Period is chosen to be 600nm in this case and duty cycle is 50%. Vertical dotted line represents the effective index of SPP mode. (b) Reflection spectrum for a sensor design with period = 600nm, duty cycle 50% and grating thickness = 149nm (horizontal dotted line (a)).

Once the SPP mode is excited, small changes of on or above the surface will be reflected in the wavelength shift of reflection spectrum. The detectable changes could be changes of surrounding refractive index, thickness of material attached to the surface, etc. Figure 4. 11 (a) and (b) shows how the sensor response to the thickness of material attached to the surface.

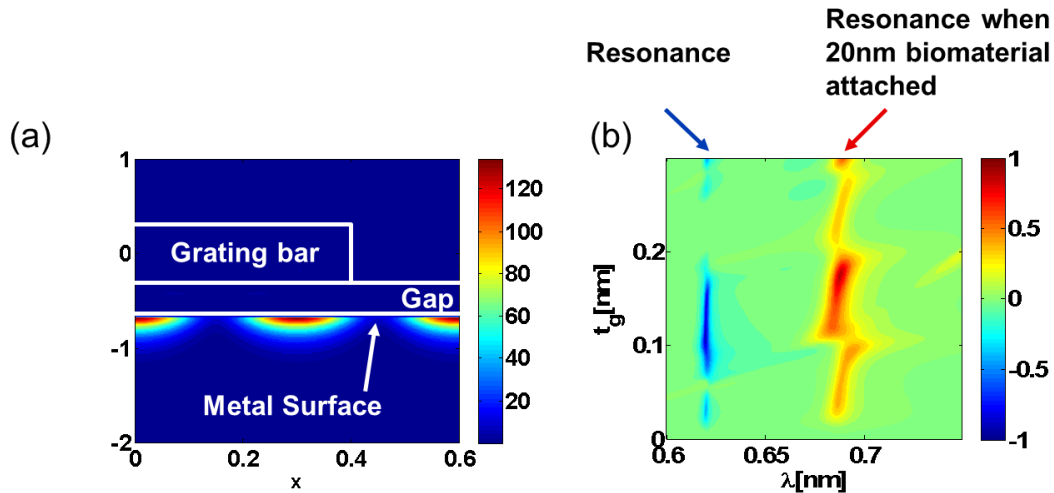


Figure 4. 10 (a) FDTD simulation showing the mode pattern of SPP mode. Intensity is enhanced at the metal surface to improve the surface sensitivity. (b) Reflection as function of wavelength and grating thickness. Two resonance lines indicate SPP resonance with surface binding thickness $t_b=0\text{nm}$ and 20nm .

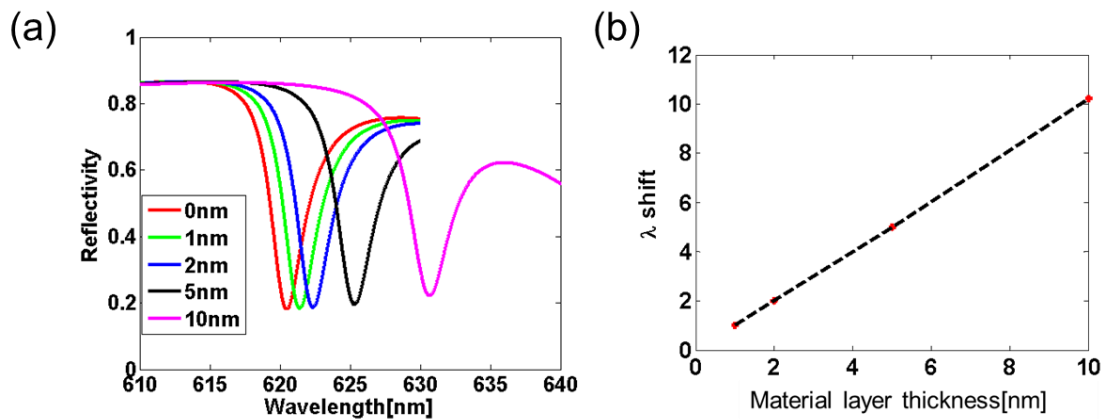


Figure 4. 11 (a) Reflection spectra with different layer thickness of material attached to the surface. (b) Function of the resonance wavelength as function of material layer thickness attached to the metal surface.

4.6.3 Fabrication Process

The fabrication process is illustrated in Figure 4. 12. The process starts with a semiconductor wafer with sacrificial layer under the device layer. The sacrificial layer can be selectively etched to make the device layer suspending. One common structure with such configuration is the silicon-on-insulator wafer. It has a silicon device layer on top of a buried oxide layer, which serves as the sacrificial layer that can be selectively removed with hydrofluoric acid. However, other material combinations with selective etching capabilities can also be utilized, for instance, InP/AlGaInAs, GaAs/AlGaAs, etc. Lithography will be performed to generate the grating pattern onto the wafer. Depends on the critical feature size, which is directly related to the target optical resonance wavelength, conventional photolithography can be used for features greater than 1 μ m, while high resolution lithography techniques, such as DUV lithography or ebeam lithography, can be utilized. Following the lithography step, an etching step (In the silicon case, RIE etching is used) is performed to etch away the exposed area of the device layer. The HCGs are therefore defined with transferring the pattern on the photoresist to the semiconductor layer. In order to facilitate the transfer of the HCGs to other substrates, the HCG structure needs to be released from the original rigid substrate. The sacrificial layer under the HCGs is selectively etched, making the grating bars suspending. The HCG transfer process is then performed. The HCGs are covered by polydimethylsiloxane (PDMS). The suspending HCG bars will attach to the surface of the PDMS. By peeling off the PDMS from the rigid substrate, the HCGs are transferred to the flexible PDMS substrate, whose cross section is shown in the figure with HCGs sitting on top of the flexible carrier. After the HCGs are transferred to the flexible carrier, another thin polymer layer is coated on top of the HCGs. The thickness of this thin PDMS layer is from 10s nm to 100s nm. It can be achieved by the spin coating process with the PDMS diluted in hexane. The thickness can be controlled by varying the dilution ratio and the spin coating speed and time. In the last step, the surface plasmon polariton waveguide is fabricated with metal evaporation, as shown in the second last step in the figure.

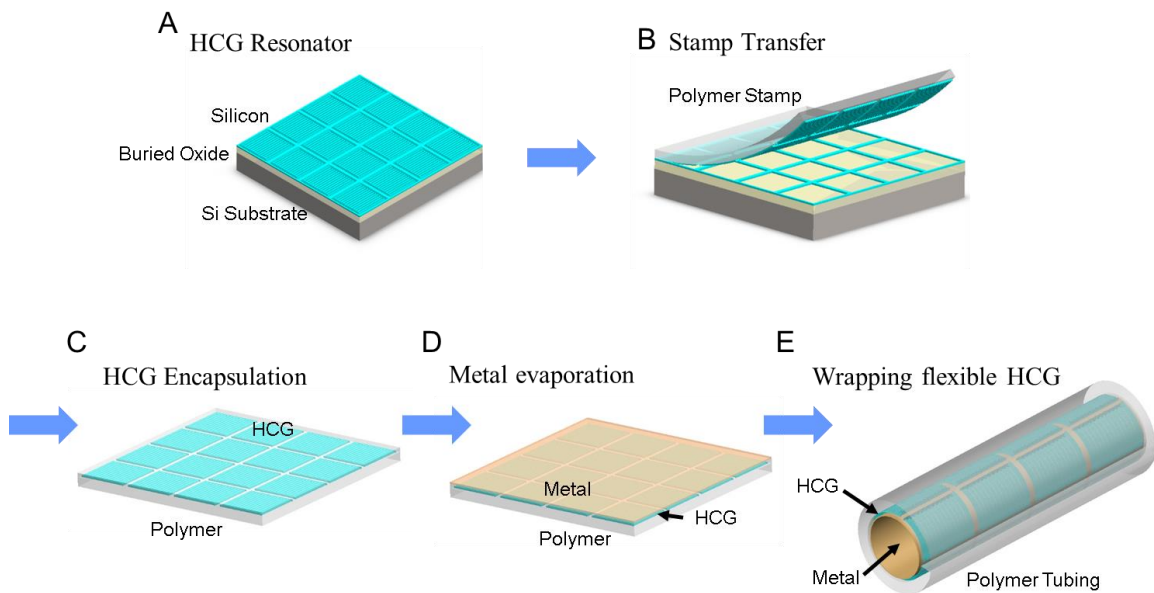


Figure 4. 12 Fabrication process for HCG-assisted SPP sensor.

4.6.4 Preliminary measurement results

We use the following configuration show in Figure 4. 13 to measure the response of flexible sensor. Broadband source is used to excite SPP. Then whole reflection spectrum is recorded. Shift of resonance wavelength is used for quantitative detection. Change on or above the surface will shift the resonance wavelength and bring the intensity change.

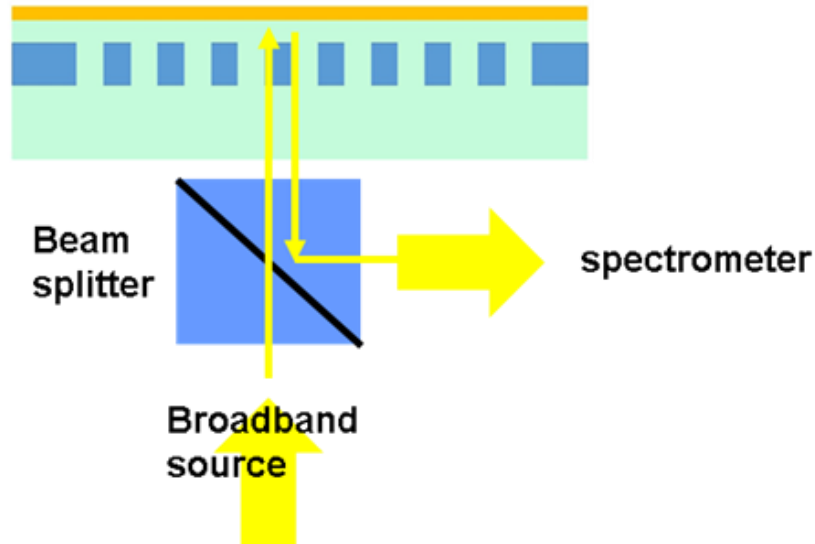


Figure 4. 13 Measurement setup schematic: broadband source (500nm to 800nm) is used to excite the SPP resonance. Spectrometer is used to collect the reflection spectrum. Resonance wavelength shift will give us information on the sensor surface changing.

Different concentration of glucose solution is added to the sensor surface. Measurement results are recorded and shown in the Figure 4. 14. There is a fixed relation between the glucose concentration and refractive index. By perform the calculation, refractive index sensitivity is then extracted: Resonance wavelength shifts 16nm when there is around 0.15 change in the refractive index, indicating sensitivity $\sim 110\text{nm/RIU}$.

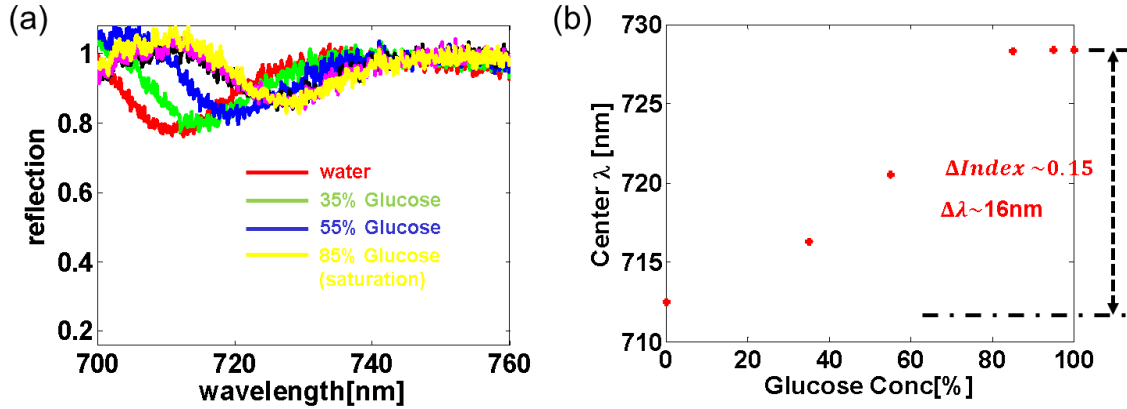


Figure 4. 14 (a) Reflection spectrum at different concentration of glucose concentration. (b) Resonance wavelength shift as function of different glucose concentration. Resonance wavelength shifts 15nm when there is index difference ~ 0.15 .

4.6.5 Future application in catheter bacteria detection

Hospital-acquired infection (HAI) is an infection developed by a hospital environment. Over 1.7 million HAIs are estimated in the United States every year, resulting 99,000 death [57]. The catheter-related infection, which is caused by the presence of the bacteria in the catheters, can lead to very severe consequences. The catheter-related bloodstream infection is one of the most frequent, lethal and costly complications of the venous catheterization. Attributed to the increase in invasive medical devices and procedures, immunocompromised patients and an overall increase in elderly patients, the death rate of catheter-related infection has been increase in the recent decades. Therefore, inexpensive detection of intact bacteria flowing through the catheter is critical for reducing the infection, resulting less complications for the current procedures and overcoming the obstacles for exploring the advanced treatments.

The proposed optical sensor can be used to achieve low cost catheter bacteria detection. Because such a structure is fabricated on a flexible substrate, it can be wrapped to form a tube. With standard tubing connectors, such tubing section will be connected in series with the ordinary plastic tubing. The resonance wavelength is sensitive to the antibody-antigen reaction on the metal surface, leading to the sensitive detection of the bacteria in the tubing, shown in Figure 4. 15.

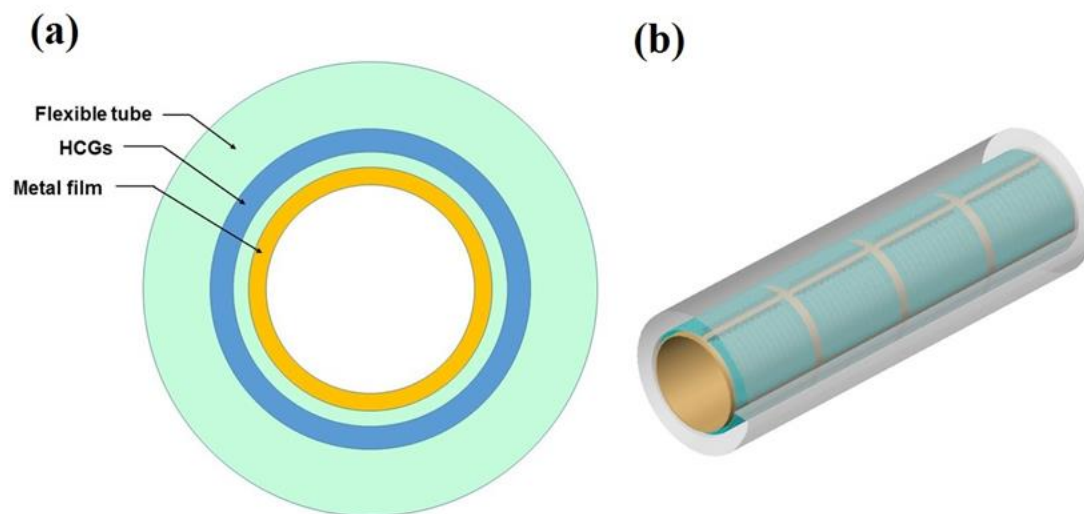


Figure 4. 15 (a) Cross section (b) Three dimensional view of the biosensor tubing

4.7 Four Wave Mixing inside HCG Resonator

4.7.1 Introduction

Nonlinear optical frequency conversion is important for many applications, including photonic switching, correlated photon pair generation, and narrow linewidth sources [58-61]. Recently, Four Wave Mixing (FWM) in silicon platform has received intense investigation due to the potential of integrating with electric/photonic circuits, scalable manufacturability, and a reasonably large third-order susceptibility in silicon [62]. FWM in silicon devices has been studied in slab waveguides, resonator structures, photonic crystal slow light waveguides etc [63-68]. These structures are mostly based on silicon waveguides, utilizing strong index contrast between core and cladding to achieve high transverse confinement. Enhanced optical intensity inside silicon due to mode confinement will then result in increased FWM efficiency. However, in such structures, laser input is usually coupled into in-plane waveguide structures from an off-chip source. The optical coupling loss between an optical fiber and the in-plane waveguide structures compromises the net conversion efficiency and total power consumption. Efficient coupling requires both optimized coupling structures (i.e. grating couplers or tapered waveguides) and accurate alignment, thus greatly increasing the system complexity [69, 70]. In addition, for practical applications, it is critical to develop devices with high efficiency at low pumping levels.

In this chapter, we present a novel Si-based on-chip high contrast grating (HCG) resonator and demonstrate resonance enhanced degenerate four-wave mixing. Theoretically and experimentally, the HCG resonator has been demonstrated to have high optical quality factor [10, 25]. Furthermore, laser light can be directly coupled to the HCG resonator from a free space or fiber output with very high efficiency (~87% experimentally). A lower bound Q of 7330 was chosen in the experiment to allow a cavity linewidth ~210pm, within which the four-wave mixing process is enhanced by the resonance. The surface-normal input angle is designed to allow for easy alignment and setup robustness. High FWM conversion efficiency (-19.5dB) in this resonator has been demonstrated under low pumping power (~900 μ W).

4.7.2 High contrast gratings resonator design and fabrication

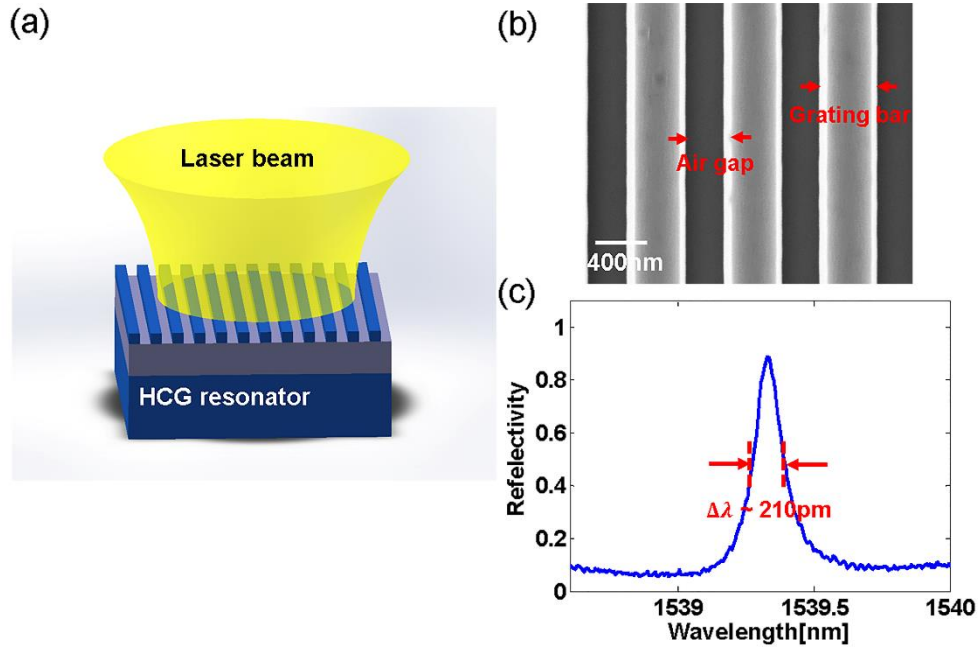


Figure 4. 16 (a) Schematic of HCG resonator. In this particular design, resonance is coupled by a surface normal plan wave input with TE polarization. Grating thickness t_g , period Λ and duty cycle are important parameters to determine the resonance wavelength and quality factor. (b) Top view of SEM image of gratings within a single fabricated HCG resonator. (c) Measured reflection spectrum for the HCG resonator. Linewidth shows 210pm, indicating $Q \sim 7330$. An absolute reflectivity (normalized by gold mirror) of 87% was achieved at the peak indicating a very high coupling efficiency.

Devices are fabricated on an SOI wafer with a 500nm Si device layer and 3 μm buried oxide layer. A simple two-step fabrication process including optical lithography and silicon etching was used. We chose grating period (780nm) and barwidth (410nm), which can be easily fabricated with ASML300 deep UV stepper. Reactive ion etching (RIE) was performed for Si etching (Lam Research). In the scanning electron micrographs of the fabricated devices shown in Figure 4. 16 the HCG structure is evident and good fabrication accuracy is observed.

Measurement is performed to exam the optical quality factor (Q) of the fabricated devices. The single device we fabricated has a lateral size $\sim 800\mu\text{m} \times 800\mu\text{m}$ and input spot size is adjusted to be 20 μm diameter. In this scenario, the HCG is practically infinite compared to the spot size we used in the measurement. A tunable laser centered at 1550nm is used as the excitation and is set in a continuous sweeping mode between 1538nm and 1540nm at a rate of 40nm/sec. Laser light is adjusted to TE polarization (parallel to the grating bars). The power of the reflected light is recorded using a photodiode in real time and is synchronized to the laser sweep rate. Reflection spectrum is normalized to a near 100% gold mirror and then plot in Figure 4. 16 (c). As high as 87% peak reflection was obtained, indicating an excellent surface-normal coupling efficiency. Theoretical

predication shows that 100% reflection is expected at resonance wavelength [10]. Experiment results will be further increased if structure optimization is performed under Gaussian beam excitation. A linewidth ~210pm indicates that the Q for this device is ~7330, an excellent value for high FWM conversion efficiency with a reasonable detuning range.

One most important advantage of HCG resonator over the other on-chip resonators is the high coupling efficiency with single mode fiber output or free-space Gaussian mode. From the discussion in the previous chapter (Chapter 2 & Chapter 4.2), we know that excellent match of mode intensity profile with the input Gaussian beam contributes to the easy and efficient coupling from the input.

4.7.3 Enhanced four-wave mixing experiment

We demonstrated that an HCG can be a high Q resonator with easy and efficient coupling from an off-chip laser source. Now we show its application in degenerate four wave mixing (FWM). We consider the net conversion efficiency $\eta = P_{idler} / P_{signal}$ by taking the ratio of idler output power and signal output power. This ratio can eliminate the difference caused by fluctuation from the experiment setup (i.e. coupling and laser fluctuation). Thus, the conversion efficiency under certain pumping power will serve as an important figure of merit to determine performance of FWM devices. Theoretically, the conversion efficiency for resonance enhanced FWM can be modeled using the following equation [71, 72]:

$$\eta = \gamma P_p L' |FE_p|^4 FE_s^2 FE_c^2. \quad (4.1)$$

where γ is the third order nonlinear parameter, P_p is the pumping power, L' is the effective optical length and FE_p, FE_s, FE_c are the field enhancement factors of pump, signal and idler respectively. This simple equation contains physics for both FWM and the resonator. To take the most advantage of cavity enhancement for FWM in the HCG resonator, the pumping laser is typically aligned to the center of resonance frequency. In the experiment, we place both pumping and signal inside the same cavity linewidth. Thus, FE_p^2, FE_s^2 and FE_c^2 have the same Lorezian lineshapes with HCG cavity under first order estimation. When the pumping laser is fixed at the resonance wavelength, conversion efficiency η lineshape will be described by square of cavity lineshapes. Thus, the detuning linewidth will be roughly depending on $1/Q$.

Figure 4. 17 shows the schematic of the experimental setup used to achieve the degenerate FWM in the HCG resonator. Two continuous-wave tunable lasers serve as the pump and signal source, respectively. A 50:50 optical fiber coupler combines the pump and signal prior to coupling them into HCG resonator. A 5x objective lens is used to adjust the laser spot size to achieve optimized coupling. The reflected beam and the generated signal are collected by the same objective and directed to an optical spectrum analyzer through a free space beam splitter. High coupling efficiency with simple alignment is enabled by the unique resonance mode of inside HCG as we discussed in Chapter 4.7.2.

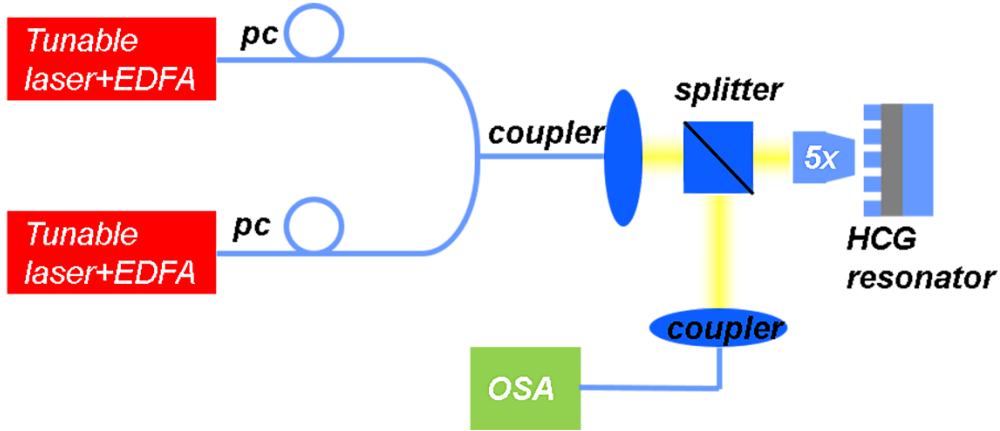


Figure 4. 17 Schematic of the FWM measurement setup.

Figure 4. 18 shows the observed FWM results in the HCG resonator. In this example, the pump wavelength is set at 1538.9nm, located at the center wavelength of the resonance to maximize the cavity enhancement. The signal laser is set at 70pm detuning. The idler shows up as a side band with frequency $\nu_{idler} = 2\nu_{pump} - \nu_{signal}$. The net conversion efficiency in this particular configuration is approximately -19.5dB at a low pumping power of $\sim 900\mu\text{W}$.

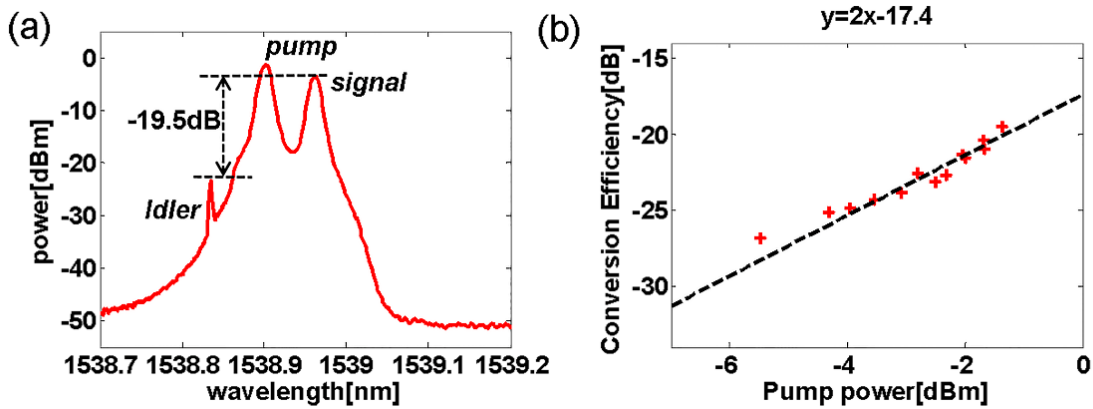


Figure 4. 18 (a) Reflection beam spectrum taken from the OSA; -19.5dB conversion efficiency is achieved in this configuration. (b) Conversion efficiency as function of signal power. The slope of the Log-Log plot is nearly 2, indicating the idler signal is generated from FWM.

Conversion efficiency as function of pumping power is plotted in Figure 4. 18 (b). The slope of the linear fitted line (nearly 2) in the log-log plot indicates that the pulse at frequency $2\nu_{pump} - \nu_{signal}$ is caused by FWM inside HCG resonator.

Next, we studied the FWM detuning characteristics inside the same device. In the measurement, the pumping laser and signal laser detuning were both placed within the resonance linewidth, with carefully controlled TE polarization. Two example series of idler

measurements are presented in Figure 4. 19, with different pump and signal detuning wavelengths, respectively. In Figure 4. 19 (a), the pump wavelength is set at center wavelength of the resonance (1538.9nm) with the signal detuning from -200pm to -70pm. In Figure 4. 19 (b) signal wavelength is fixed with the pump detuning from -240pm to -70pm. In both series, the parametric idler is clearly observed as a side band to the cavity resonance, located at frequency $2\nu_{pump} - \nu_{signal}$.

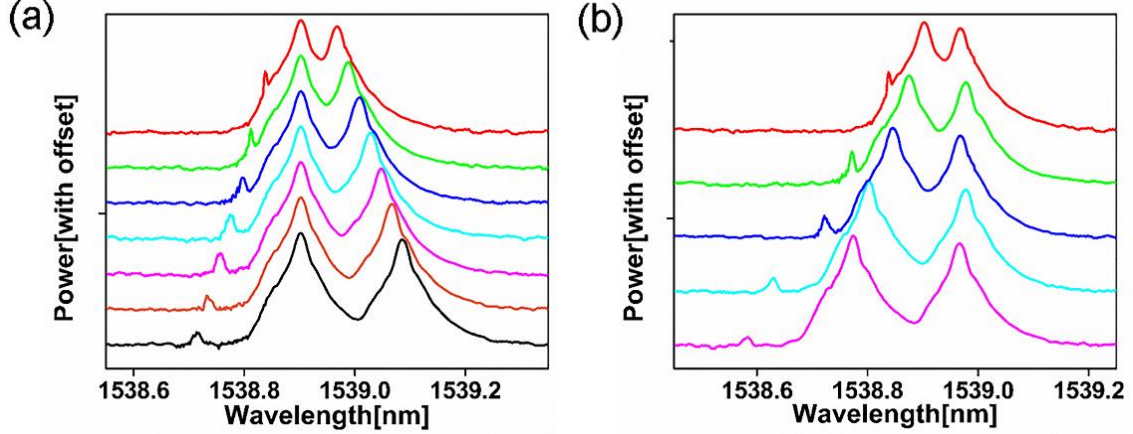


Figure 4. 19 Wavelength detuning: (a) Signal detuning with pump fixed at resonance wavelength (1538.9nm). (b) Pump detuning with fixed signal laser.

The phase matching condition for FWM in HCG resonator can be expressed in terms of the requirement fitting the idler frequency inside the resonance:

$$\Delta\nu = |\nu_{idler} - \nu_{res}| < \frac{\Delta\nu_{FWHM}}{2}. \quad (4.2)$$

where $\Delta\nu_{FWHM}$ is the resonance linewidth. Figure 4. 20 shows conversion efficiency as a function of signal detuning wavelength (with pumping laser fixed at resonance frequency). The measurement results are plotted as red dots and a numerical fitting based on Eq. (4.1) is shown as a black dashed curve. Under first order estimation, the FWM detuning bandwidth roughly matches the HCG resonance linewidth. In our numerical fitting, FE^2 is assumed to have a shape of Lorentzian function with peak ~ 7330 . L' is $\sim 0.5\mu\text{m}$.

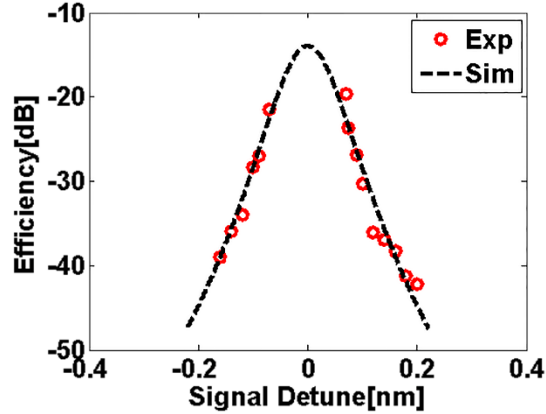


Figure 4. 20 Conversion efficiency as a function of signal detuning. Red dots are measurement results. Black dashed line is from numerical simulation using Eq. (4.1).

4.7.4 Discussion

To our knowledge, this is the first time that high Q resonance and four wave mixing are observed in a Si based HCG resonator. Compared with other on-chip Si resonators, aseptically those photonic crystal cavity with far-field optimization [22], HCG resonators gain benefits from direct and more efficient coupling from either free-space optics or fiber output. It reduces design complexity, area on chip and total power consumption. Highest Q we measured so far is ~ 7330 , lower than the highest number reported in photonic crystal cavity or ring resonator [73]. However, this number is mainly limited by the imperfection of etching (side wall roughness and 60 side wall angle). We are expecting 2 orders of improvement with optimized process.

On one hand, the peak conversion efficiency is strongly depending on resonance enhancement, which is proportional to cavity quality factor (Q). On the other hand, lineshape of conversion efficiency η function is described by square of cavity lineshape function, which is depending on $1/Q$. Thus, there is an obvious trade-off between detuning linewidth and peak efficiency. This trade-off may limit the practical use of resonance-enhanced FWM as wavelength conversion devices. One solution to overcome this problem is to employ a resonator array together with wavelength splitting device. Each resonator inside the array will be optimized for high efficiency at single wavelength. Resonance wavelength inside the array will be designed to vary with grating period and duty cycle, which can be easily defined in the lithography step. By taking advantage of free-space operation, we can put the wavelength splitting device (i.e. diffraction gratings) in front of HCG resonators array. Different wavelength will be diffracted to the ‘right’ device inside the array. This will not increase the system cost because of the small HCG resonator footprint and coupling mechanism.

4.7.5 Summary

We observed resonance enhanced four-wave mixing in a surface-normal coupled silicon based high contrast grating (HCG) resonator, with an experimentally measured $Q \sim 7000$. We achieve a peak conversion efficiency of -19.5dB at a pumping power of $\sim 900\mu\text{W}$. Coupling efficiency is $\sim 87\%$ with an easily aligned and robust configuration. The device demonstrated here could have a small footprint and the potential to be built into a large array to increase the operation wavelength range.

Chapter 5 High Contrast Grating Based Spatial Light Modulator for Optical Remote Sensing

5.1 High Contrast Grating Optical Phased Array

5.1.1 Introduction

Optical phased arrays have enabled free-space beam steering for a wide range of applications, such as imaging, display, chemical-bio sensing, precision targeting, surveillance, etc. In this remoting sensing applications, light has to be fast scanned through target. A high-speed, chip-scale optical phased array is of particular desire. It fits in the advanced applications such as fast imaging and ranging (LIDAR) etc, where high operation speed, low power consumption, high integration density, and small footprint are desirable. The central element of the phased array is the individual phase tuner. The phase tuner can either actively emit light with different phase, or passively transmit or reflect incoming light while modifying its transmission phase or reflection phase. Several phase tuning mechanisms have been demonstrated for optical phased arrays, such as using electro-mechanical [74, 75], electro-optic [76], and thermo-optic [77, 78] effect. The liquid crystal represents the most mature technology; however its response time is very slow, typically in the order of hundreds of Hz to tens of kHz [79, 80]. Thermo-optic is slow in response as well. Electro-mechanical (i.e. MEMS) based phase tuner can be fast, but the MEMS structure is usually sophisticated in design and fabrication. High speed phase tuning has been reported in dielectric waveguide array using electro-optics effect; however the waveguide is arranged in one dimension, and thus only one dimensional beam steering can be realized.

In this sub-chapter (Chapter 5.1), we demonstrate a high speed novel 8x8 optical phased array based on high contrast grating all-pass filters with low voltage microelectromechanical actuation. Each array element is an all-pass filter (APF) at 1550 nm with a high contrast grating (HCG) [10] as a reflective top reflector and a distributed Bragg reflector (DBR) as the bottom reflector. The incident light comes at surface normal to the APF; the phase of the reflective light can be tuned efficiently with a small actuation distance of the HCG. A phase shift as large as 1.7π is experimentally demonstrated within 50 nm displacement of the HCG and 10 V actuation voltage, in a speed as high as 0.5 MHz. Beam steering is demonstrated by creating a near-field reflection phase pattern with different applied voltages on individual pixels.

5.1.2 HCG MEMS piston phase tuner

From the discussion in previous chapters (Chapter 2 & 3), we know that HCG is a very good reflector. Also, due to its light weight, it be efficiently electrostatically actuated. An intuitive way to construct a phase tuner is to use HCG as a piston mirror. In this scenario, a laser beam comes at surface normal incident angle onto the HCG and then gets reflected back. By actuating the HCG reflector up and down, the reflection light will experience physical delay due to the change of optical path, and thus the phase is tuned accordingly. This is shown in the schematics below.

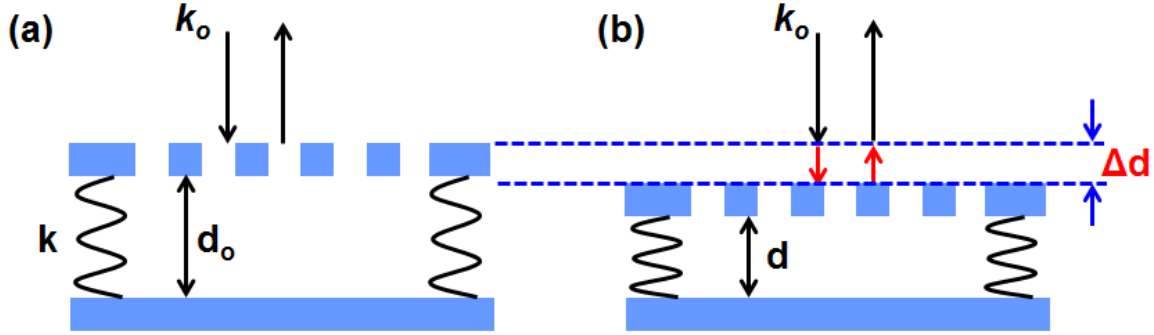


Figure 5. 1 Schematic of using HCG as a piston mirror for phase tuner. The HCG is connected to the substrate with a spring. HCG can be electrostatically actuated by capacitor structure. When the HCG has been displaced by a distance Δd , the reflection light experiences a phase delay of $\Delta\varphi = 2k_0\Delta d$.

The piston mirror provides a straight forward phase tuning mechanism. The drawback is that in order to achieve a 2π phase shift (needed in a phase array), a very large actuation distance is required. This distance is directly related to input wavelength, and is $\lambda/2$. Large actuation distance usually means a larger voltage, and complex fabrication. On the other hand, in order to have a rapid actuation speed, the spring constant k needs to be large to have a larger mechanical to allow a larger mechanical resonance frequency. However, this means the actuation voltage is further increased. By using the HCG as actuated mirror, we can greatly reduce this required actuation voltage due to the light weight of sub-micrometer thick semiconductor grating. We will use several formulas in the following to show:

For a capacitor-based MEMS actuator, spring structure is used to connect the movable mirror to the fixed anchor. We have formulation:

$$F = k(d - d_0) \quad (5.1)$$

where d_0 is the initial distance between two plates of the capacitor. In our case, two plates are HCG reflector and the substrate. When voltage is applied between the two plates, HCG will be moved to a new place d . The electrostatic force associated is as followings:

$$F_e = \frac{\partial W_e}{\partial d} = -\frac{\epsilon_0 A}{2d^2} V^2 \quad (5.2)$$

When stable states reach, $F = F_e$. Then balance equation is as followings:

$$(d - d_0)d^2 = -\frac{\epsilon_0 A}{2d^2}V^2 \quad (5.3)$$

From previous analysis, we know that for a 2π phase shift, displacement $\Delta d = \frac{\lambda}{2}$, and the required voltage is as following:

$$V_{2\pi} = \sqrt{\frac{\lambda k}{\epsilon_0 A}} \left(d_0 - \frac{\lambda}{2}\right) \quad (5.4)$$

For a smaller $V_{2\pi}$, we need a smaller d_0 . However, the minimum gap size to avoid MEMS pull in in a capacitor based actuator is $2/3d_0$. This means that minimum d_0 is $\frac{3\lambda}{2}$. Thus, we can reform Eq. (5.4):

$$V_{2\pi} = \sqrt{\frac{\lambda k}{\epsilon_0 A}} \lambda \quad (5.5)$$

On the other hand, the mechanical resonance frequency f_r is function of mirror mass and spring constant, which is shown in the following:

$$f_r = \frac{1}{2\pi} \sqrt{\frac{k}{m}} \quad (5.6)$$

Eq. (5.5) and (5.6) show that there is a linear relation between the $V_{2\pi}$ and f_r . We can write in the form shown in the below:

$$V_{2\pi} = 2\pi \sqrt{\frac{\lambda m}{\epsilon_0 A}} \lambda f_r \quad (5.7)$$

Eq. (5.7) shows that for a higher speed phase tuning, a larger actuation voltage is required. Also, the $V_{2\pi}$ is positively proportional to the mirror mass m , and here we can clearly see the advantage of a single HCG grating over other traditional mirrors (DBR or metal mirror). Figure 5. 1 shows the relation between $V_{2\pi}$ and f_r for a Si based HCG reflector. HCG used in the simulation is $20\mu\text{m} \times 20\mu\text{m}$, with a duty cycle of 0.5 and thickness $\sim 200\text{nm}$. It is clearly seen in the calculation, the required voltage is more than 40V for resonance frequency larger than 0.5MHz. Such a large voltage is not compatible to most integrated circuits. Thus, more efficient tuning mechanism is needed to reduce the tuning voltage.

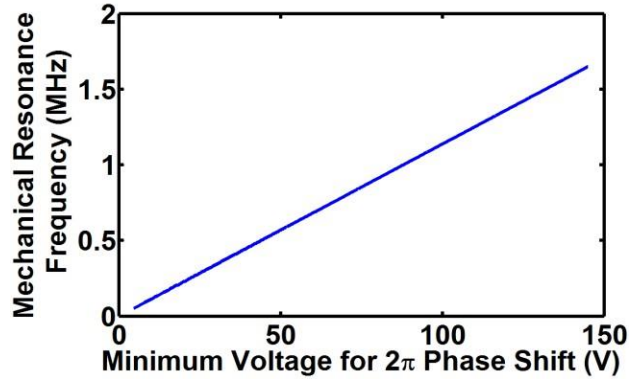


Figure 5. 2 Linear relationship between $V_{2\pi}$ and f_r for a Si based HCG reflector.

5.1.3 All pass filter approach

To reduce the actuation voltage, we use resonator structure to amplify the phase tuning. By replacing the substrate shown in Figure 5. 1 with a highly reflective mirror, an FP etalon can be constructed. Figure 5. 3 shows the typical reflection spectrum, and the reflection phase spectrum of a typical FP cavity. The dip in the spectrum indicates the resonance. Across the resonance, 2π phase shift is achieved. In Figure 5. 3 (b), we fix the incident light wavelength and plot the amplitude reflection and phase spectrum as function of cavity length. Similarly, as the cavity length goes across the cavity resonance, 2π phase shift is achieved. In the calculation, the reflectivity of the top HCG and bottom DBR is 0.99 and 0.995 respectively. The cavity length is set to be 775 nm, and the central wavelength is set to be 1550 nm. Note that in the calculation for Figure 4.4 (a), the phase dispersion of the mirror is not considered. The reflection phase of both mirrors is set to be π .

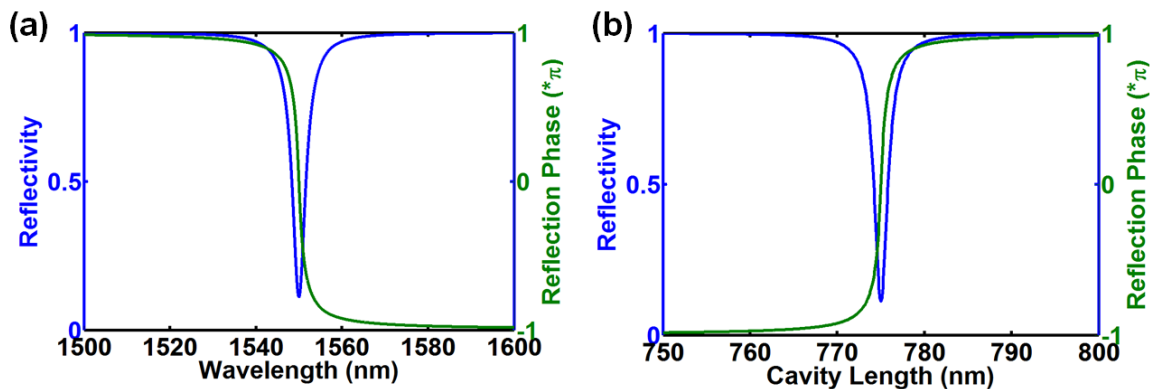


Figure 5. 3 (a) Reflection spectrum and reflection phase spectrum of a FP cavity. (b) Reflectivity and reflection phase versus the cavity length, at a fixed incident wavelength of 1550nm.

As shown in Figure 5. 3 (b), a small cavity length change (i.e. top mirror displacement) leads to a very large reflection phase change. This sets up a foundation for efficient phase tuning. As the cavity length is tuned, different reflection phase is obtained,

however, the reflectivity is also different. In particular, the reflectivity at the cavity resonance point is low. This translates to the non-uniform reflectivity among the different pixels in the phased array, since each pixel might be assigned to provide different phase. This non-uniform reflectivity effectively scatters the light into the background, and lowers the contrast in the far field beam steered pattern. Thus a uniform reflectivity is desired for different reflection phase value.

Actually this is a typical problem in etalon reflection spectrum. A simple way to solve the problem will be adjust the top and bottom mirror reflectivity (R_1 and R_2 respectively). Dip in the reflection spectrum indicates loss in the system. Assuming an ideal all pass filter, there should be a uniform response in amplitude reflection spectrum. Less reflective bottom mirror bring loss to the whole filter and thus contribute to the reflection dip. In the following figure, we show that when we fix the top mirror reflection and how the bottom mirror reflection will influence on the reflection dip and phase transition. Reflection dip become shallower with increase of bottom mirror reflection. This is also consistent with the fact system loss decreases with increase of bottom mirror reflection.

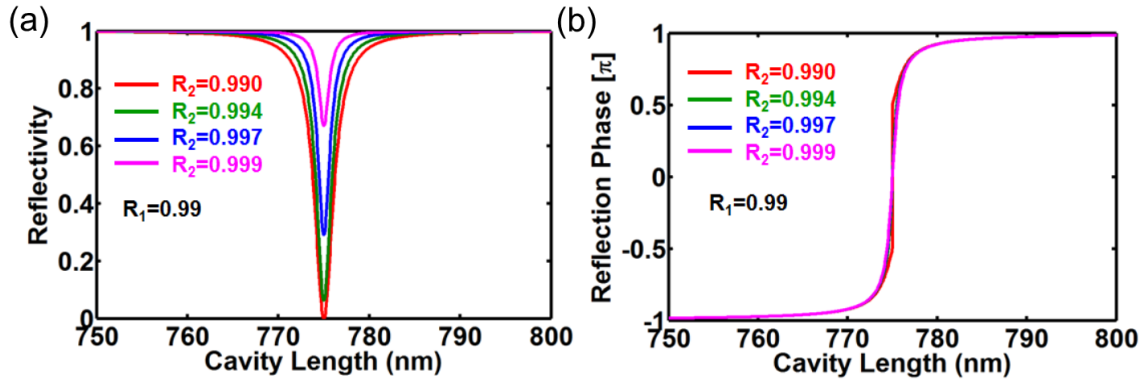


Figure 5. 4 R_1 is the reflection from top mirror and R_2 is the reflection from bottom mirror. (a) Reflection dip become shallower with increase of bottom mirror reflection. (b) Phase spectra with various bottom mirror reflection.

In the following figure, we fix bottom mirror reflection to a relatively high value (0.997 in this case), and vary the value of top mirror reflection. We can see from the figure that as R_1 decreases, the reflection dip at the resonance becomes shallower, and at the meanwhile, the phase transition becomes less sensitive to the cavity length change. This also could be understood from the energy point of view: in our simulation, bottom mirror reflection is set to be 0.997. And this non-ideality contributes to the system energy loss. Less reflective top mirror means smaller resonance quality factor and less light cycling inside cavity, and thus less loss. In this sense, the dip will become shallower. Practically, this will be a good operation regime for all-pass filter. Although phase change sensitivity is sacrificed, the tuning sensitivity is still an order better than piston mirror and also more flat reflection spectrum is obtained.

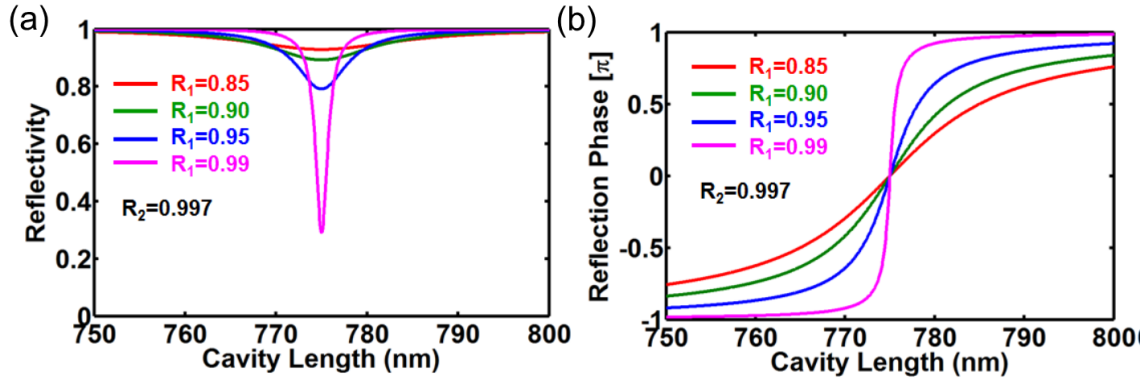


Figure 5. 5 Bottom mirror reflection is fixed at 0.997. Top mirror reflection is varied from 0.85 to 0.99. (a) Amplitude reflection spectra with various R_1 value. (b) Phase reflection spectra with various R_1 value.

5.1.4 HCG based all pass filter

From previous chapters, we know that HCG can be a good reflector. By replacing the uniform membrane with HCG, one gains the flexibility in controlling the mirror reflectivity and thus the cavity quality factor. By actuating the HCG to tune the length of the etalon across its Fabry-Perot (FP) resonance, the reflection phase of the surface normal incident light experiences a continuous phase change approaching 2π , while the reflection beam power can maintain nearly the same with the incident light. The resonance effect greatly enhances the phase tuning efficiency, i.e. a small HCG displacement for a large phase shift. High speed and low voltage can be achieved at the same time.

The high-contrast grating (HCG) is a single layer of subwavelength grating composed of a high-refractive-index material (e.g. Si or III-V semiconductors) surrounded by low-index materials (e.g. air or SiO_2). The HCG can be designed as a very broadband high reflection mirror ($R > 0.99$, $\Delta\lambda/\lambda > 30\%$). It has been implemented as a reflector in vertical-cavity surface-emitting laser (VCSEL) [13] and hollow-core waveguide [22]. HCG has also been used as a piston mirror for optical phased array [4], where the phase of the reflection beam on the HCG can be tuned linearly with the displacement of the HCG. While this approach is simple and straightforward, a long HCG actuation distance is required for a 2π phase shift, trading off actuation voltage for high speed operation. To overcome this problem, here we construct an all-pass filter using a top HCG and bottom DBR, with carefully designed reflectivity. Optical all-pass filters have been studied before [81, 82, 83], and MEMS tunable all-pass filter has been reported for applications as modulators and dispersion compensators [84], with a silicon nitride membrane as the front reflector. By replacing the uniform membrane with HCG, one gains the flexibility in controlling the mirror reflectivity and thus the cavity quality factor. By actuating the HCG to tune the length of the etalon across its Fabry-Perot (FP) resonance, the reflection phase of the surface normal incident light experiences a continuous phase change approaching 2π , while the reflection beam power can maintain nearly the same with the incident light. The resonance effect greatly enhances the phase tuning efficiency, i.e. a small HCG

displacement for a large phase shift. High speed and low voltage can be achieved at the same time.

Figure 5. 6 shows the schematic of the APF. The device is fabricated on a GaAs epitaxial wafer. The HCG is defined by electron beam lithography, and followed by a reactive ion etch on a p-doped $\text{Al}_{0.6}\text{Ga}_{0.4}\text{As}$ epitaxial layer, which is on top of an intrinsic sacrificial layer and 22 pairs of GaAs/ $\text{Al}_{0.9}\text{Ga}_{0.1}\text{As}$ n-doped DBR. The sacrificial layer is subsequently etched to form a FP cavity with the suspended HCG as top mirror and DBR as bottom mirror. To form the all-pass filter, the reflectivity of the DBR is designed to be >0.9975 and the HCG ~ 0.9 . The HCG period, bar width and thickness is designed to be 1150 nm, 700 nm and 450 nm respectively. The incident light polarization is TE, i.e. electrical field along the HCG bars. The static cavity length is 700 nm; with the reflection phase response of the designed HCG, this corresponds to the cavity resonance wavelength of ~ 1550 nm. Each HCG mirror is $20\ \mu\text{m}$ by $20\ \mu\text{m}$ in size, and 8×8 individual pixels form the whole optical phased array, with the pitch $\sim 33.5\ \mu\text{m}$. The pixels are isolated from each other by deep trenches, and they are individually electrically addressable through the metal fanned-out lines. Figure 5. 7 shows the scanning electron microscope (SEM) image of the fabricated device.

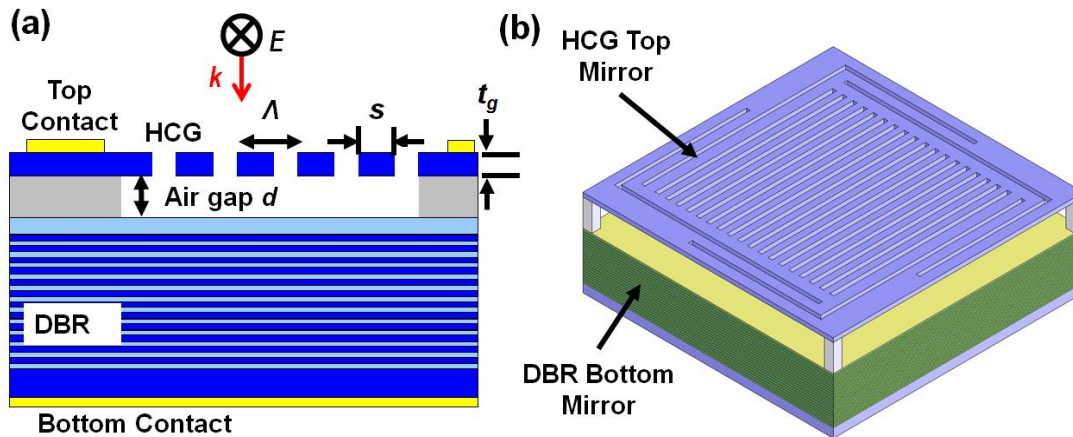


Figure 5. 6 Schematic of an individual pixel of the optical phased array. The $\text{Al}_{0.6}\text{Ga}_{0.4}\text{As}$ HCG and 22 pairs of GaAs/ $\text{Al}_{0.9}\text{Ga}_{0.1}\text{As}$ DBR serve as the top and bottom reflector of the Fabry-Perot etalon. The incident light is surface normal to the etalon, and polarized in parallel to the grating bar. Λ , HCG period; s , grating bar width; t_g , HCG thickness; d , air gap between HCG and DBR. We design $\Lambda=1150$ nm, $s=700$ nm, $t_g=450$ nm, and $d=700$ nm.

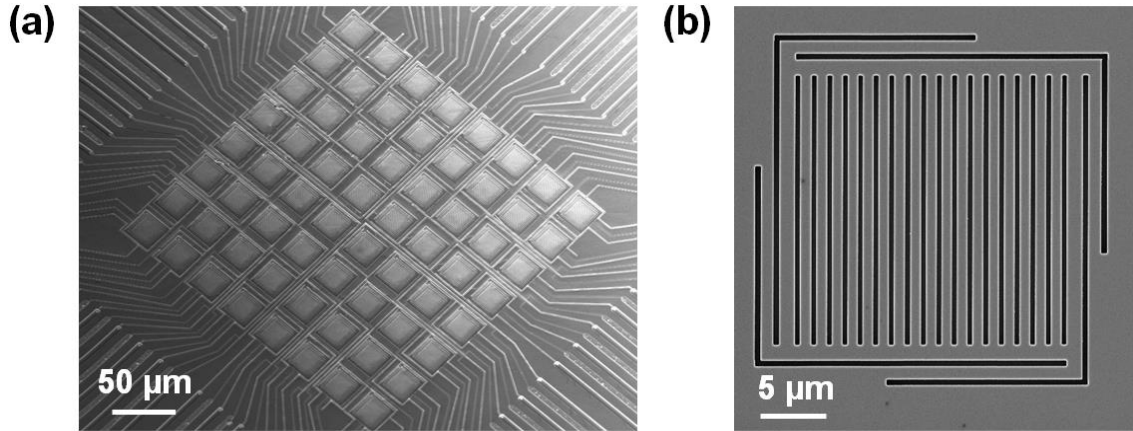


Figure 5. 7 SEM image of an 8x8 optical phased array. Each pixel is an HCG-APF, which can be individually electrically addressed by the fanned-out metal contacts. The pitch of the HCG mirror is $\sim 33.5 \mu\text{m}$. (b) Zoom-in view of the HCG mirror in a single pixel. The HCG mirror size (without the MEMS) is $20 \mu\text{m}$ by $20 \mu\text{m}$.

The HCG can be actuated by applying a reverse electrical bias between the HCG and DBR. This changes the cavity length and thus the reflection phase of the incident light. Figure 5. 8 (a) shows the reflection spectrum of a single HCG APF of the array, for different reversed bias. As the reversed bias increases, the cavity length decreases, resulting in a blue-shift of the resonance wavelength. The measured reflection spectrum is fitted with the standard FP etalon reflection formulation, and the top mirror and bottom mirror's reflectivity is extracted. The reflectivity of the bottom DBR is extracted to be 0.9965 ± 0.0012 , and the reflectivity of the top HCG increases from 0.955 to 0.976 as the wavelength decreases. The HCG reflectivity is higher than the designed value due to an inadvertent inaccuracy in electron beam lithography and etching process.

The reflection phase of an individual etalon versus applied voltages is then characterized by a Michelson interferometer. The result is shown in Figure 5. 8 (b). A total phase change of $\sim 1.7 \pi$ is achieved within 10 V actuation voltage range at a wavelength of 1550 nm. The actual displacement of the HCG can be extracted from Figure 5. 8 (a) and the cavity design. For this 1.7π phase change, the HCG displacement is 50 nm. This demonstrates the high phase tuning efficiency of the APF. The reflectivity of the DBR and HCG can be extracted from this phase measurement by a curve fitting. They are extracted to be 0.9977 and 0.935 respectively, in a reasonable good match with the value extracted from the reflection spectrum measurement.

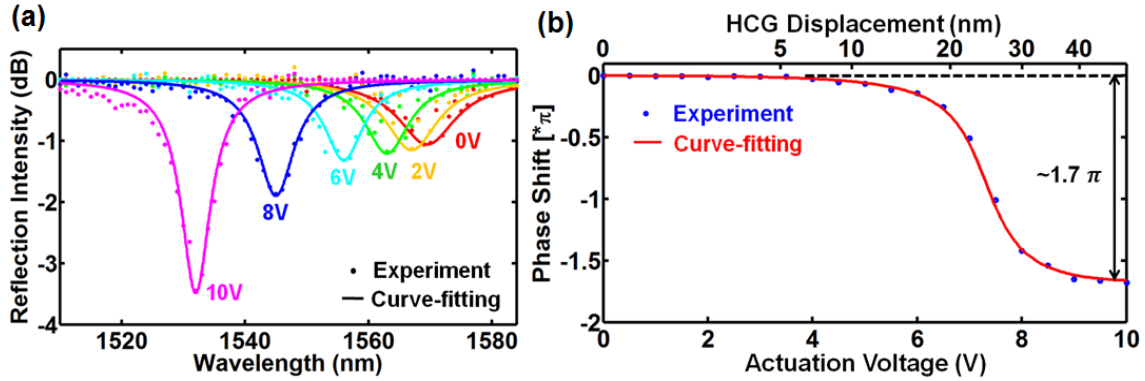


Figure 5. 8 (a) Reflection spectrum of an HCG-APF with different actuation voltages. As the reversed bias increases, the cavity length decreases, resulting in a blue-shift of the resonance wavelength. (b) Reflection phase shift versus applied voltage on a single HCG-APF of the phased array. $\sim 1.7 \pi$ phase shift is achieved within 10V actuation voltage range at a wavelength of 1550 nm; this corresponds to a displacement of ~ 50 nm of the HCG. The measured results are curve fitted to extract the reflectivity of the DBR and HCG.

The MEMS HCG is designed to have a high mechanical resonance frequency to facilitate a fast phase tuning. Two different methods are used to characterize the mechanical resonance frequency. The first one is the laser Doppler velocimetry (LDV). A white-noise electrical signal is used to actuate the HCG. A laser is incident onto the HCG, and the Doppler shift of the reflection beam is recorded with respect to time, followed by a Fourier transform to reveal the information in the frequency domain, shown in Figure 5. 9 (a). The mechanical resonance frequency f_r is 0.53 MHz. Alternatively, a step voltage is applied to actuate the HCG mirror, and time resolved phase measurement can be used to extract the mechanical resonance frequency. This time resolved phase trace is shown in Figure 5. 9 (b). The applied voltage changes from 6 V to 7 V at $t=13.7 \mu\text{s}$ and back to 6 V at $t=33.8 \mu\text{s}$. A damped second harmonic oscillator model is used to analyze the ringing trace. The damped mechanical resonance frequency is extracted to be 0.52 MHz, in good agreement with the LDV measurement.

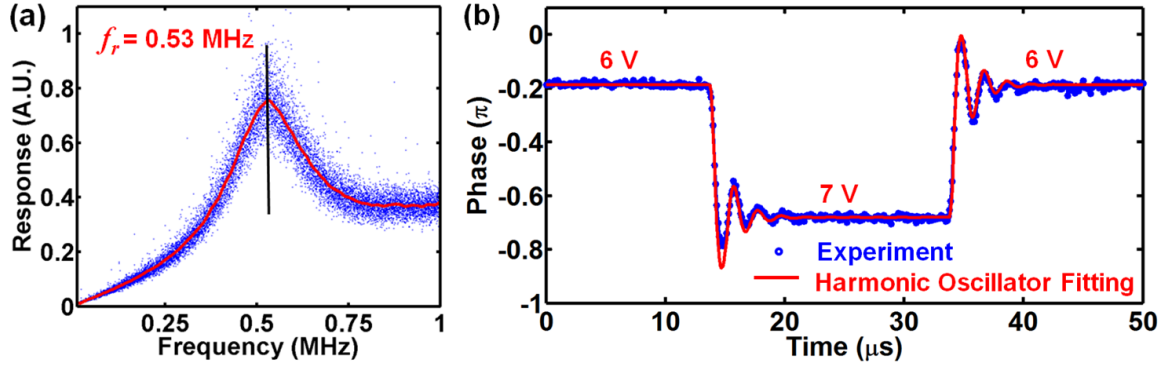


Figure 5. 9 (a) Laser Doppler velocimetry measurement to characterize the mechanical resonance frequency of the HCG MEMS mirror. (b) Time resolved phase measurement of the HCG APF with a step voltage actuation signal. The blue dots are recorded in the experiment, and red traces are the simulated fitting curve from the second harmonic oscillator model.

In Figure 5. 9 (b), ringing in the phase response is seen. This is not ideal in the practical system. To reduce the ringing, one can break the single voltage step into two steps, i.e. using input shaping technique [85, 86, 87]. Instead of changing directly from 6 V to 7 V in the above example, we first change the voltage from 6 V to 6.5 V, hold it for 1 μs , and then change from 6.5 V to 7 V. The same applies for the case when the voltage changes from 7 V to 6 V. The 1 μs corresponding to about half of the ringing period, and thus the individual ringing from these two separate steps would have destructive interference, leading to an overall reduced ringing. The comparison between the single step and two step voltage control is shown in Figure 5. 10. The phase settles down much quicker when the two-step voltage control is used.

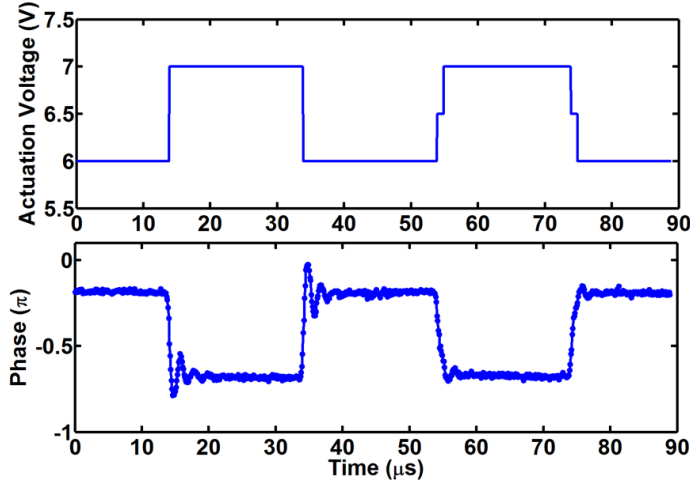


Figure 5. 10 Comparison of the ringing between a single step and two step voltage control. In the two step voltage control case, the time interval between the two different steps is 1 μs , corresponding to half of the ringing period. The individual ringing from these two separate steps would have destructive interference, leading to an overall reduced ringing.

5.1.5 HCG based all pass filter array for beam steering

Beam steering in far-field is achieved by creating the desired near-field phase front of the reflection beam on the whole 8x8 phased array. By controlling the applied voltage on each individual pixel of the HCG-APF array, the near-field phase pattern can be generated. The beam steering experiment setup is similar to that described in [87]. The maximum steering angle is achieved when the phase is alternative between the pixels. This is also defined as half the total field of view (TFOV). Since the pitch of the pixel of the 8x8 array is 33.5 μm , the TFOV is 2.65°, for the operation wavelength of 1550 nm. To increase this, a two-lens system is used to magnify the beam steering angle. This angular magnification ratio is set to be 3.45 in the current experiment, and thus the TFOV is 9.14°. Optical measurement setup is shown in Figure 5. 11, where a 4-f system is used to expand the beam steering angle. Device is mounted in a chip holder and attaches to the PCB circuit board to address each filter element shown in Figure 5. 12.

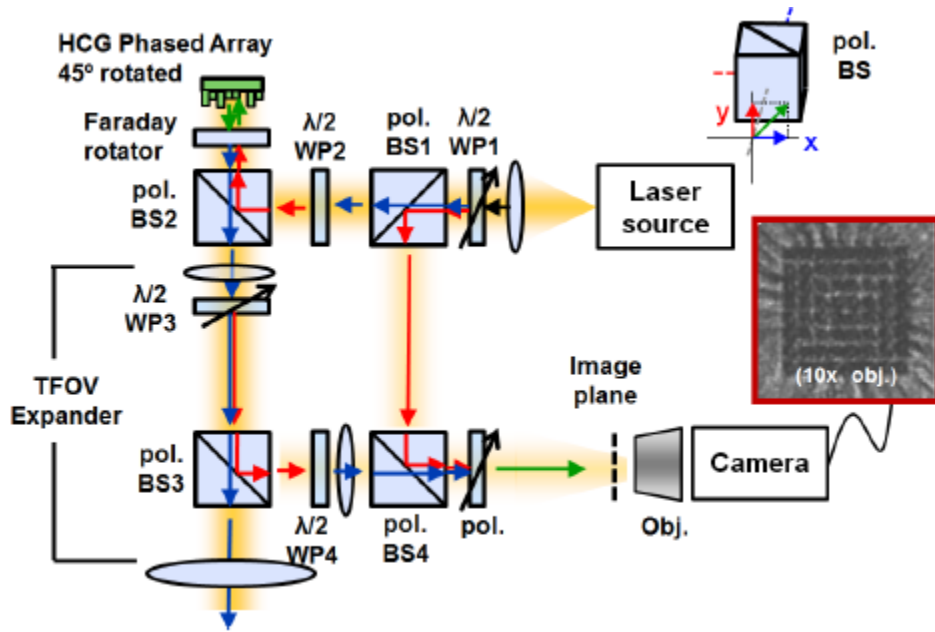


Figure 5. 11 Experimental setup to characterize the reflection phase of the HCG APF phased array, as well as the beam steering performance. WP, wave plate; pol. BS, polarization beam splitter; Obj., objective; pol., polarizer; TFOV, total field of view.

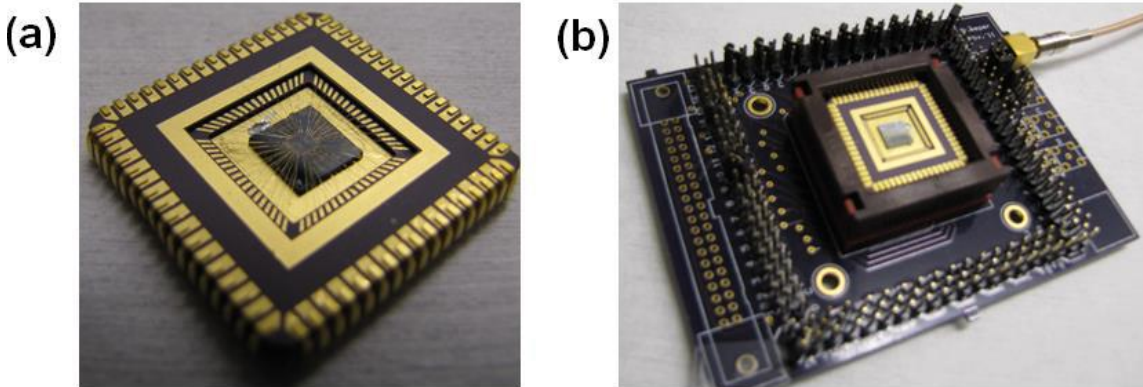


Figure 5. 12 Image of an assembly of the optical phased array system. The chip is bonded on the chip carrier (a), which is hosted by a printed circuit board (b).

Figure 5. 13 (a) and (c) shows various near-field phase patterns on the phased array, and the corresponding measured far field pattern. Both symmetric (column 2~5) and asymmetric (column 6~7) beam steering are performed. The TFOV is shown as the box in dashed line in Figure 5. 13 (c). The strong zeroth order beam is due to the relatively low filling factor of the phased array (~36%). Quite a large portion of light gets directly reflected from the background without phase shift, contributing strongly to the zeroth order beam. The ratio between the total power of the steered beams and that of the

zeroth order beam is measured to be ~ 0.5 in the best case. With the consideration of the filling factor, Fourier optics is applied to calculate the far-field patterns, shown in Figure 5. 13 (b). The measured value of the full width beam divergence at the half power point (FWHM) is $\sim 1^\circ$. This FWHM is determined by the total size of the array, calculated to be 0.33° , and magnified to be 1.14° by the lens. The experiment is in reasonable good agreement with the calculation results.

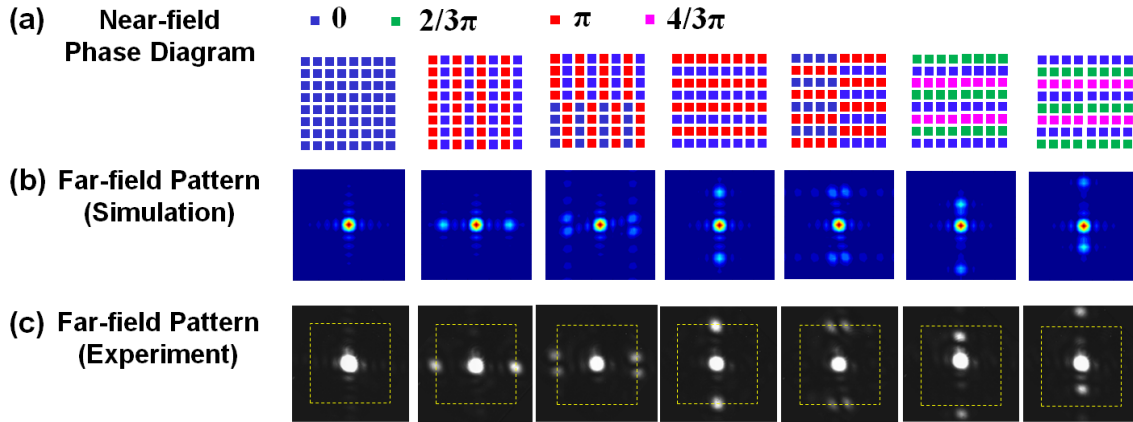


Figure 5. 13 Beam steering experiment. (a) Near-field phase pattern created by the HCG-APF optical phased array. (b) The corresponding far-field pattern calculated by Fourier optics. (c) Experimentally measured far-field pattern, in reasonable good agreement with the calculation. The strong zeroth order beam is due to the relatively low filling factor of the phased array ($\sim 36\%$). The light that does not hit on the HCG-APF gets directly reflected without phase shift, contributing strongly to the zeroth order beam. The field of view of the image windows is $13^\circ \times 13^\circ$. The box in dashed line in (c) indicates the TFOV of the phased array ($9.14^\circ \times 9.14^\circ$).

5.1.6 Discussion

In the previous sections, we present the HCG all-pass filter, and its application in optical phased array for beam steering. While we demonstrate its high-speed and low-voltage operation, there is much room to improve the overall performance of the all-pass filter array. Here we discuss the strategies.

First of all, while the all-pass filter serves as a phase shifter for the incident beam, it also changes the power of the reflection beam, as seen in Figure 5. 8 (a). This is not desirable. To improve this, one can increase the reflectivity of the bottom DBR, by increasing the number of pairs; and meanwhile slightly decrease the reflectivity of the top HCG. Both approaches reduce the reflection loss at the resonance.

Secondly, due to the large number of pixel size, there can appear some non-uniformity among the array pixels -- more specifically, the non-uniformity in the phase tuning curve shown in Figure 5. 8 (b). In the beam steering experiment, the deviation of the phase from its desired value in each pixel effectively scatters the light into the background and thus reduces the beam steering efficiently. To overcome this problem, one can actively monitor the phase and apply a feedback loop for the phase control on each individual pixel.

Thirdly, both the TFOV and the divergence angle of the reflective beam from the phased array are important figure of merits. Their ratio determines the total number of resolvable spots across the TFOV in one dimension. This number is 8 in the device discussed above. The TFOV can be increased by reducing the pixel size; and the beam divergence angle can be decreased by scaling up the pixel numbers. Together, this will boost up the number of resolvable spots in TFOV.

Fourthly, the zeroth order beam appears to be quite strong in Figure 5. 13. To suppress it, one can increase the filling factor of the phased array. To demonstrate this, we design a high-filling factor array by grouping four pixels together without isolation trenches in between. Furthermore, two dimensional HCG [88, 89] is designed and fabricated. The symmetric HCG can overcome the polarization sensitivity of the one-dimensional HCG. The two-dimensional HCG grid can also be actuated more uniformly. Figure 5. 14 (a) shows the SEM image of the two-dimensional HCG mirror for the HCG-AFP array. The HCG mirror size is $20\ \mu\text{m}$ by $20\ \mu\text{m}$, and the filling factor is $\sim 47\%$. Beam steering is experimentally demonstrated with the two-dimensional HCG-AFP, shown in Figure 5. 14 (b). Compared to device used for Figure 5. 13, more power is being beam steered in this case. The ratio between the total power of the steered beams and that of the zeroth order beam is ~ 1.2 . The increase power in the steered beam is also attributed to the improved pixel uniformity of the array.

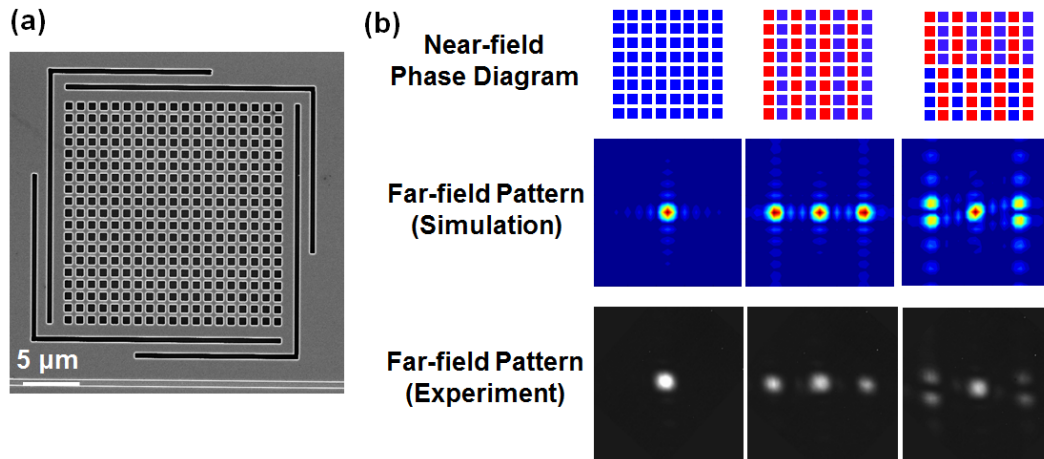


Figure 5. 14 (a) SEM image of the two-dimensional HCG mirror for HCG-APF array. (b) Beam steering experiment of the optical phased array using two-dimensional HCG as the top mirrors of the APF. Top panel, near-field phase pattern created by the HCG-APF optical phased array. Middle panel, the corresponding far-field pattern calculated by Fourier optics. Bottom panel, experimentally measured far-field pattern, in good agreement with the calculation.

5.1.7 Summary and future work

In summary, a novel 8x8 optical phased array using HCG-APF is experimentally demonstrated for beam steering. The key advantage of using HCG APF is its high efficient phase tuning, i.e. small HCG MEMS mirror displacement (~ 50 nm) for large phase change ($\sim 1.7\pi$), and small voltage actuation (10 V) for fast beam steering (>0.5 MHz). The property of the HCG APF is also temperature independence, since the main cavity is made up of air. Both one-dimensional HCG and two-dimensional HCG are demonstrated as the top mirror for the APF. Beam steering is achieved by creating the desired near-field phase pattern on the HCG-APF array. Beam steering performance can be optimized by increasing the reflectivity of the bottom DBR, scaling up the pixel number while reducing the individual pixel size, as well as increasing the filling factor. We believe that by integrating a microlens array in front of the phased array, the effective filling factor can increase to 100%, leading to a greatly improved beam steering efficiency. This work paved the road of realizing an on-chip fast beam steering device and may be potentially be used in many remote sensing applications, such as LIDAR or fast optical imaging.

To further optimize the beam steering performance, a micro-lens array can be placed in front of the phased array, which can focus the input beam onto the HCG mirror of each pixel. This effectively increases the filling factor to 100%, and will ultimately suppress the zeroth order beam. However, this may not be easy to be achieved using

traditional micro-lens array since they have limited filling factor. We propose to use HCG lens to overcome this problem.

High Contrast Grating (HCG) is an array of high index material fully surrounded by low index medium. We demonstrated broadband reflector and high-Q resonator using periodic HCGs. Also, chirped HCG can be designed for lens purpose [1], utilizing the fact that HCG resonance is strongly localized. Schematic of a 1D HCG lens is shown in Figure 5. 15 (a). Due to the period and duty cycle change along x axis, plane wave will have different reflection phase at different x. By constructing reflection phase front, we can design different HCG planar lens for focusing or diverging purposes. To test the HCG lens concept experimentally, three different reflection lenses are fabricated and examined in experiment: 2D lens with NA~0.025, 1D cylinder lens with NA~0.1 and 2D negative lens. The device is fabricated on SOI wafer with photo-lithography and one-step etching. Figure 5. 15 (b) shows the SEM picture of a 2D circular HCG lens.

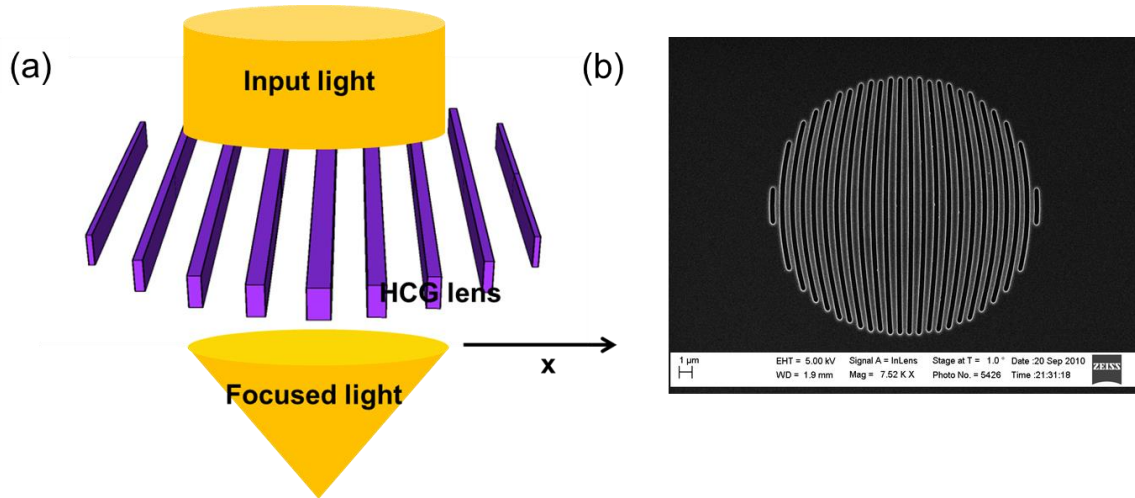


Figure 5. 15 (a) Schematic of a HCG lens. (b) SEM images for a 2D HCG lens. Devices are fabricated on SOI wafer, and the grating is sitting on oxide.

To test the HCG lens concept experimentally, three different reflection lenses are fabricated and examined in experiment: 2D lens with NA~0.025, 1D cylinder lens with NA~0.1 and 2D negative lens. The device is fabricated on SOI wafer with photo-lithography and one-step etching. 2D lens experimental results are summarized in Figure 5. 16 and Figure 5. 17. In Figure 5. 16 (a), simulation results show the intensity of the reflected field as a function of x and z, which x is the direction of grating period and z is the light propagation direction. HCG lens are located at $z = 0$ and a Gaussian source is put right above the lens. Images of reflected beam spots at different positions are recorded and shown in Figure 5. 16 (b). Beam profile can be reconstructed from the spot image and then compared with simulation results, which are shown in Figure 5. 16 (c). Good agreement strongly indicates the validity of our theory and design algorithm [1]. Using these parameters, we can then plot the beam spot size vs. propagation distance in Figure 5. 17. Focal length can be easily seen from figure 4 (~ 2mm), close to the design value. Different colour represents different wavelength.

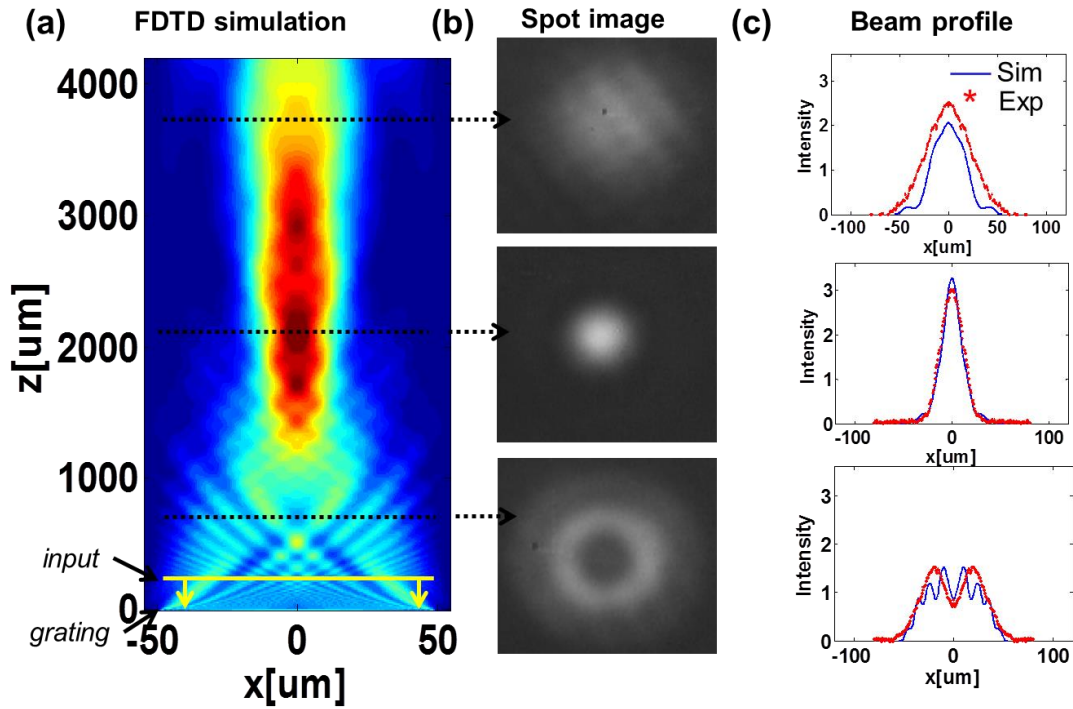


Figure 5. 16 (a) Simulated intensity of reflected beam as a function of different position for 2D lens. Positions for HCG lens and Gaussian source are indicated in the figure. (b) Laser beam spot image at different position along the propagation. (c) Beam profile along the cross section. Red dots show the experimental measurement and blue curves show the simulation results.

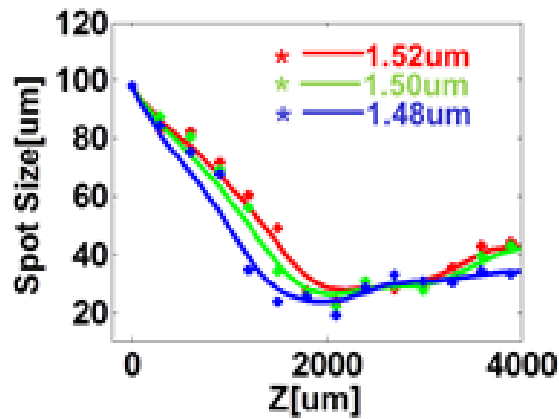


Figure 5. 17 Spot Size vs, propagation distance for 2D lens. Different colour represents different wavelength.

Similar characterization is done for 1D cylinder lens, which are shown in and Figure 5. 18. In this case, laser spot is focused only in x direction and remain unchanged in the

other direction. The reflection of the lens is also measured for a certain spectra (1530nm ~ 1565nm). 90% in reflection is a little bit lower than the expected 97%, probably due to the dimension variation in fabrication, shown in Figure 5. 19 (b).

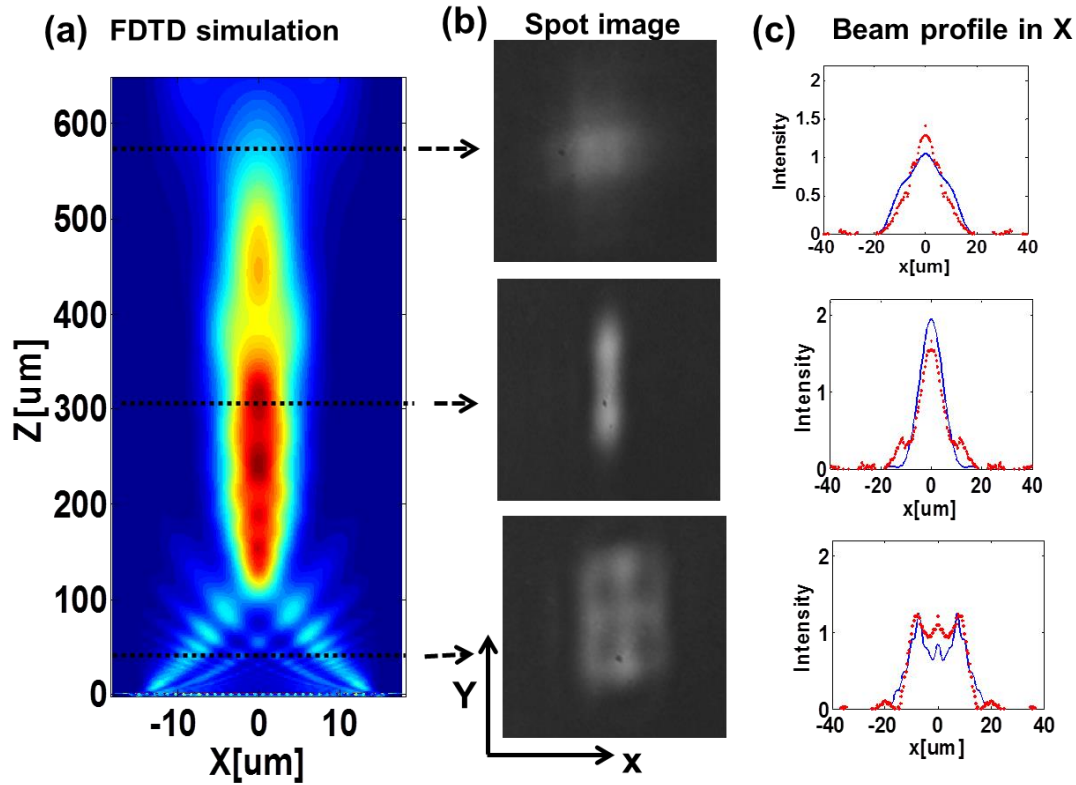


Figure 5. 18 Simulated intensity of reflected beam as a function of different position for 1D cylinder lens. Positions for HCG lens and Gaussian source are indicated in the figure. (b) Laser beam spot image at different position along the propagation. (c) Beam profile along the cross section. Red dots show the experimental measurement and blue curves show the simulation results.

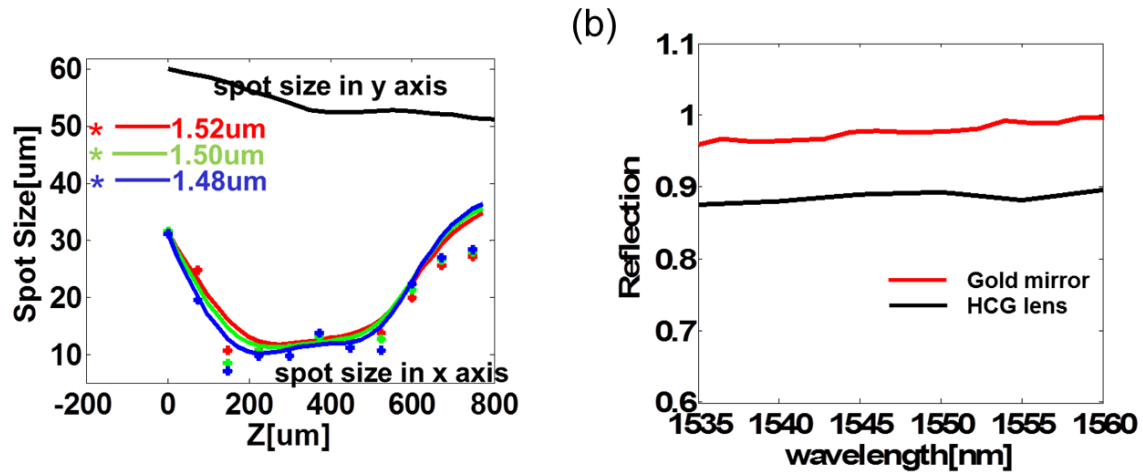


Figure 5. 19 (a) Spot Size vs. propagation distance for 1D cylinder lens. Different colour represents different wavelength. Black curves on the top gives the spot size in y direction. (b) Reflection spectra for gold mirror (red) and HCG reflective lens (black). Reflection for gold mirror is calibrated to be 98.5%.

From the previous discussion, we can find that HCG lens can provide planar geometry, large NA and high transmission/reflection efficiency. These features make it a promising solution to construct lens array with nearly 100% filling factor to improve the beam steering efficiency for our HCG all pass filter array. Our proposal is conceptually shown in the below. FDTD simulation shows the HCG lens array performance. Left figure in Figure 5. 20 (b) shows intensity pattern at focal plane. Right figure in Figure 5. 20 (b) shows that after going through a single cell inside lens array. Majority of the energy will be focused into a $10\mu\text{m} \times 10\mu\text{m}$ region in the focal plane, indicating a large focusing efficiency. By combining the HCG lens array and optical phased array, we are expecting a high-speed, large-scale, high performance beam former and beam steering.

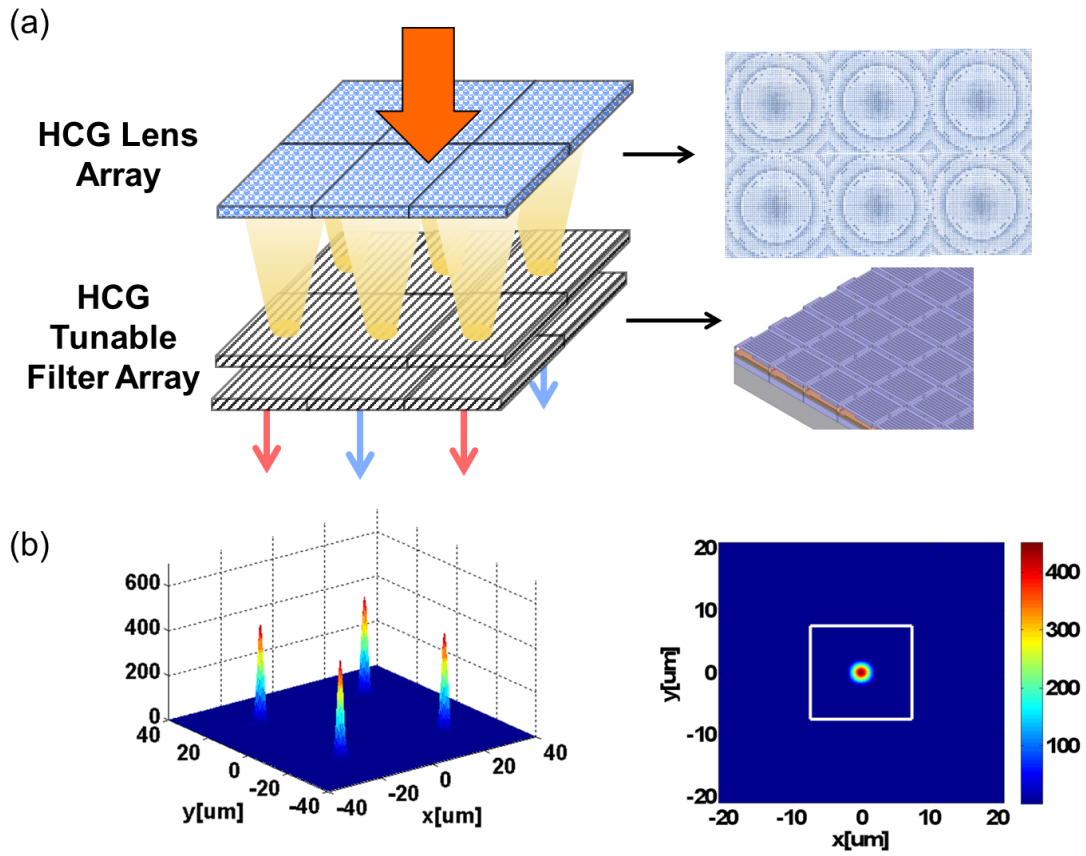


Figure 5. 20 (a) Combining optical phased array with HCG lens array to improve filling factor to nearly 100%. Schematic of lens array is shown in the right top corner. (b) FDTD simulation shows the HCG lens array performance. Left figure shows intensity pattern at focal plane. Right figure shows that after going through a single cell inside lens array. Majority of the energy will be focused into a $10\mu\text{m} \times 10\mu\text{m}$ region.

5.2 Spatial light modulator using graphene integration with high contrast grating resonator

5.2.1 Introduction

Spatial light modulators are widely used in many applications related to remote sensing, including beam scanning, beam shaping. In previous sections (Chapter 5.1), we showed our work of using HCG phased array for fast beam steering. The HCG is actuated by MEMS structure and demonstrate operation speed close to MHz. However, higher speed is difficult to achieve with traditional MEMS structure due to the increasing requirement of actuation voltage (see discussion between mechanical resonance frequency and operation voltage in Chapter 5.1). To achieve GHz tuning speed or beyond, electrical tuning is often desired. In this sub-chapter, we will show electrically controllable spatial light modulator with graphene integrated with HCG resonator, which has potential to operate at GHz operation speed.

Graphene exhibits uniform absorption [90, 91] over a broadband spectra from visible to mid-infrared. Particularly, the absorption can be dramatically modulated by electrostatic doping. By changing the Fermi level of graphene, we can ‘turn on’ or ‘turn off’ particular optical transition at corresponding wavelength. This process is shown in the figure below: Figure 5. 21 (a) shows a schematic of changing fermi level of graphene by applying voltage to graphene through a capacitor structure. Figure 5. 21 (b) shows that changing of fermi level will ‘turning on’ or ‘turning off’ optical transition at corresponding wavelength. Experimentally, fermi level can be shifted by hundreds of meV, covering from visible to infrared.

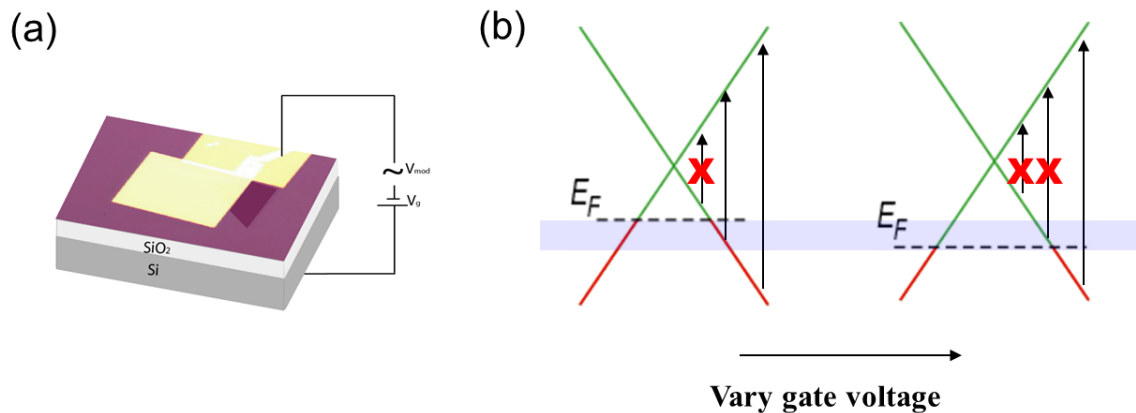


Figure 5. 21 (a) Schematic of changing fermi level of graphene by applying voltage to graphene through a capacitor structure. (b) Changing of fermi level will ‘turning on’ or ‘turning off’ optical transition at corresponding wavelength.

Secondly, high carrier mobility in graphene enables electro-optical modulator with high operation speed and low-power consumption. Several graphene-based EO modulators have

been realized by integrating graphene with waveguides [90], cavities [92] or meta-surface. For cavity-enhanced modulation, graphene strongly interacts with the cavity resonant field, resulting in a strong modulation of the cavity reflection. However, these devices are based on photonic crystal defect cavity. Low coupling efficiency may increase the total power penalty. Also, such configuration is difficult for high filling factor integration. And these drawbacks limit its application as spatial light modulation. Thirdly, due to the nature of two dimensional material, graphene has smaller density of states and also smaller active volume, making it much easier to be tuned electorally.

In this sub-chapter (Chapter 5.2) we demonstrate a new modulator architecture based on a high-mobility graphene capacitor integrated with a planar high contrast grating resonator. The HCG resonator greatly amplifies the absorption of light into graphene. In addition, HCG resonator has advantage over its counterparts: high quality factor and high coupling efficiency. Both electrolyte and dual-layer graphene structure have been realized and tested. Modulation occurs when the graphene Fermi levels are shifted to half of the incident photon energy ($\hbar\omega/2$), Pauli blocking suppresses the optical absorption. We achieved a maximum modulation depth of 10dB within a voltage swing of only 5V using electrolyte. To demonstrate the operation speed, we utilize dual-layer graphene capacitor structure to reduce the RC time constant. The speed is greatly enhanced and the measured 3dB cutoff frequency up to GHz and beyond. A schematic of our proposed structure is shown in Figure 5. 22.

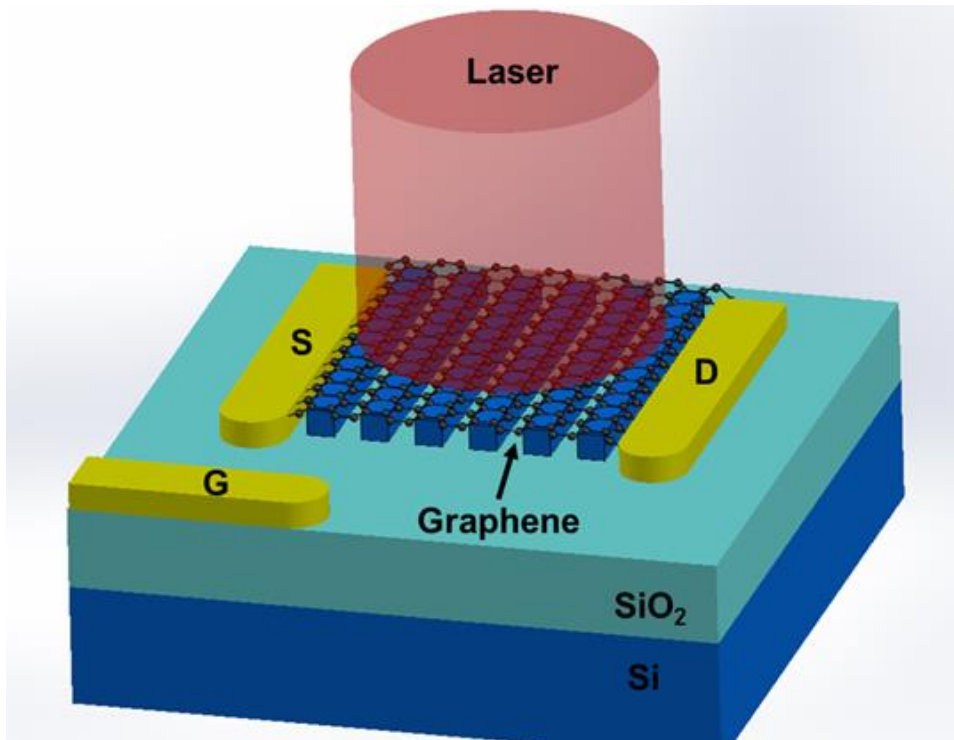


Figure 5. 22 Schematic of HCG graphene spatial light modulator. Light is directly coupled from surface normal direction. In this case, ion-gel is covered on top of device to uniformly gate the graphene.

5.2.2 Graphene integrated with HCG resonator

An important advantage of the HCG resonator over other on-chip resonance based devices is the ability to establish a unique pattern of resonance modes (See discussion in Chapter 4). Figure 5. 23 (a) shows the FDTD simulation of top view of resonance mode pattern with a $10\mu\text{m}$ Gaussian beam as excitation source coming from surface normal. White bars indicate the grating area. Large mode overlap between resonance mode pattern and input source contributes to easy and efficient coupling. Direct coupling efficiency can be above 87% experimentally without the assist of grating coupler or taped waveguide which are critical element for the other on-chip resonator. In Figure 5. 23 (b), Side view of the resonance inside one period is shown. White dashed line indicate the outlines of grating. Grating mode is specially designed to allow more mode exposure to the surface in order to achieve better graphene light interaction. Right side shows the cross section profile along the center of grating bar. A large intensity enhancement is introduced at graphene location.

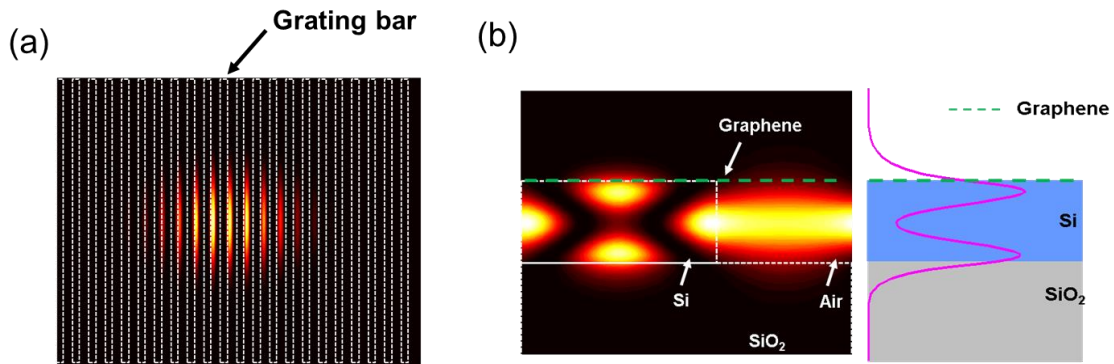


Figure 5. 23 (a) FDTD simulation of top view of resonance mode pattern with a $10\mu\text{m}$ Gaussian beam as excitation source coming from surface normal. White bars indicate the grating area. Large mode overlap between resonance mode pattern and input source contributes to easy and efficient coupling. (b) Side view of the resonance inside one period is shown. White dashed line indicate the outlines of grating. Grating mode is specially designed to allow more mode exposure to the surface in order to achieve better graphene light interaction. Right side shows the cross section profile along the center of grating bar.

5.2.3 Graphene Effect

A large-area graphene grown by chemical vapor deposition was transferred on top of the grating resonator using the standard growth and transfer processes. CVD grown graphene is usually on top of Cu foil. A layer of PMMA is spin-coated onto the graphene to act as a support. An etchant (Usually we use 1M solution of ferric chloride (FeCl_3) in water) is then used to remove the metal catalyst, after which the PMMA/graphene stack is transferred to another substrate. Solvents (Acetone in our case) are then used to remove the PMMA. Floating graphene is then finished out with HCG sample, and complete the transfer. The following schematic shows the process flow of graphene transfer.

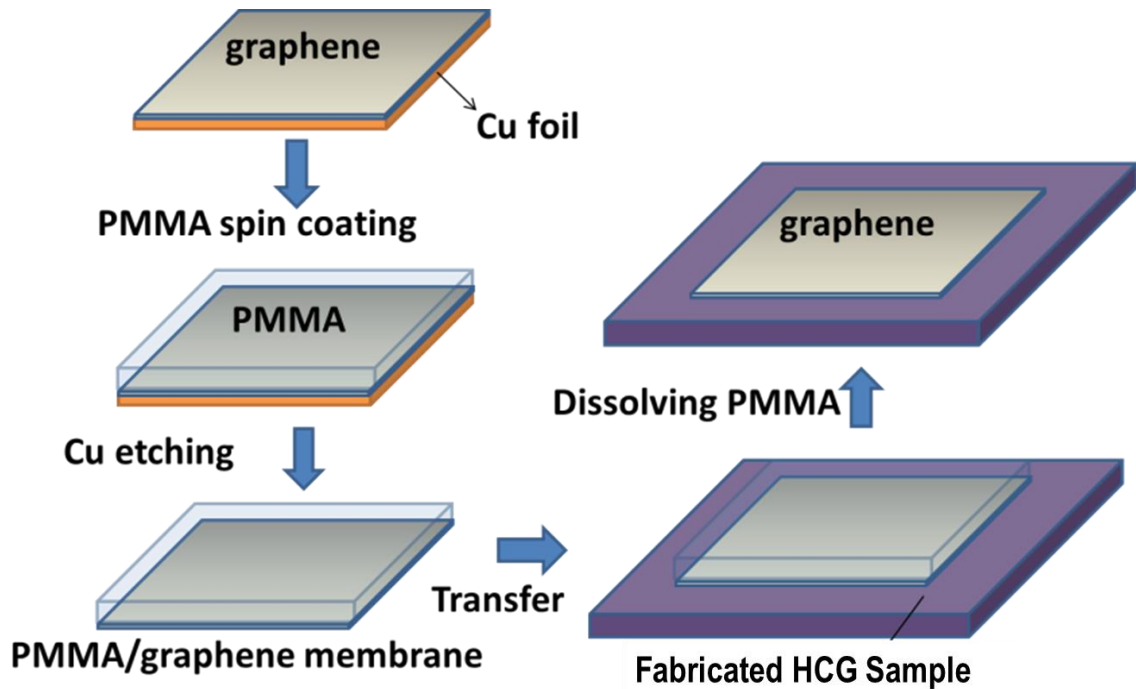


Figure 5. 24 Process flow of Graphene transfer.

To demonstrate the electrostatic gating of graphene we use a top electrolyte gating with ion-gel. The device schematic is shown in Figure 5. 22. In Figure 5. 25 (a), we show SEM images of HCG cavity with and without graphene. Top image is the HCG cavity before graphene transfer. Bottom image shows the cavity after graphene transfer. Pinholes inside the graphene layer serve as an evidence that graphene is indeed on top of the cavity. Surprisingly, the pinholes didn't affect the performance of the graphene as an effective absorber. We characterize the photonic crystal cavities in cross-polarized reflectivity measurement setup with tunable laser. Collected light is analyzed by spectrometer equipped with an InGaAs array detector. A quality factor of 1000 is observed for the fabricated device. This is the Q value for the unloaded cavity. After graphene transfer, the Q-factor reduces to 300-500, due to the absorption from graphene. Remarkably, the graphene layer renders the cavity nearly opaque, the cavity attenuation, defined as $[-10\log_{10}(\frac{R_g}{R_0})]$, increased by 12dB at the resonance of the unloaded cavity. Reflection spectrum before and after graphene transfer is shown in Figure 5. 25 (b).

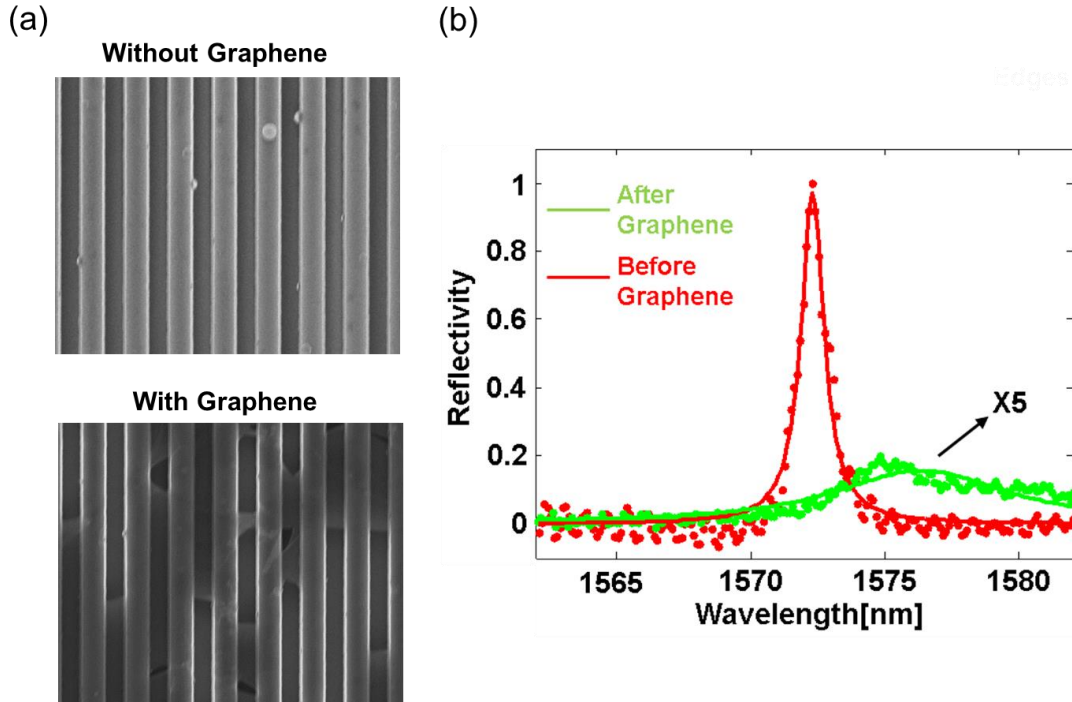


Figure 5. 25 (a) SEM images of HCG cavity with and without graphene. Top image is the HCG cavity before graphene transfer. Bottom image shows the cavity after graphene transfer. Pinholes inside the graphene layer serve as an evidence that graphene is indeed on top of the cavity. Surprisingly, the pinholes didn't affect the performance of the graphene as an effective absorber. (b) Reflection spectrum before (red curve) and after (green curve) graphene transfer. 12dB difference is achieved at 1572nm. Green curve is multiplied by 5 times and plotted with the red curve.

5.2.4 Static response

For the study of static response, we gate the graphene by means of the ion-gel that we spin-coat on the device. Figure 5. 26 shows the effect of the electric field on the graphene-HCG device. We measure the cavity reflection spectrum while varying the gate voltage at a step of 20 mV. Figure 5. 26 (a) shows the cavity reflectivity spectra for different voltages. A narrowing in the cavity line width as well as an increase in the cavity reflectivity is clearly observed with increasing gating of the graphene. We fit all of the spectra with a Lorentzian line-shape to extract the cavity resonance wavelength and linewidths. Figure 5. 26 (b) and (c) show the cavity linewidth and center wavelength as function of the applied voltage. Figure 5. 26 (d) shows reflection at 1590nm in log scale as function of applied voltage. 12dB modulation depth is achieved within 2V, making our device among the most efficient electrically tunable spatial light modulator.

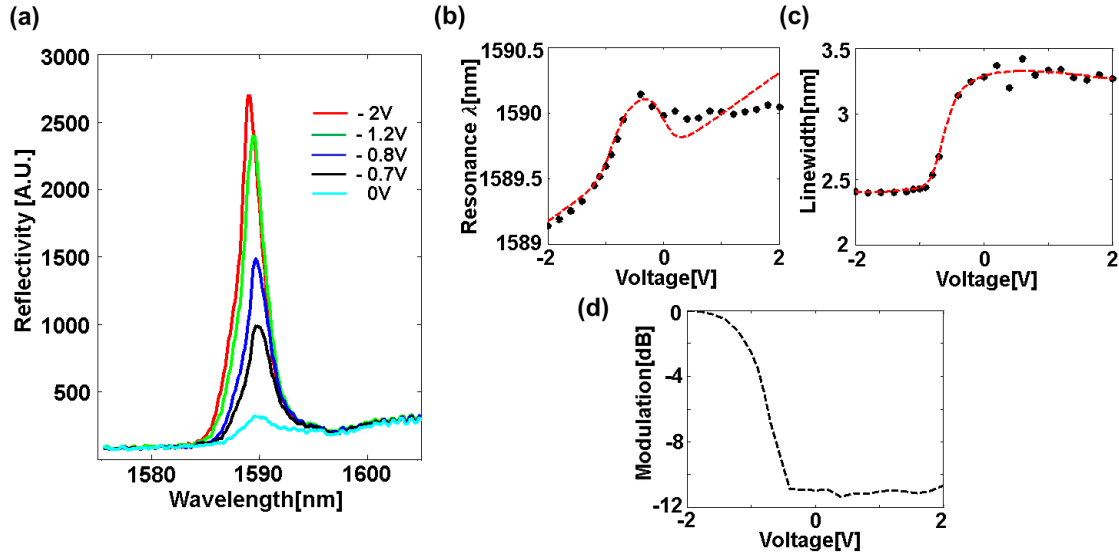


Figure 5. 26 (a) cavity reflection spectrum with various gate voltage from -2V to 0V. (b) Resonance wavelength as function of applied voltage. (c) Cavity linewidth as function of applied voltage. (d) Reflection at 1590nm in log scale as function of applied voltage.

5.2.5 High speed modulation

In the previous section, we have used ion-gel to electrostatically dope graphene to demonstrate the capability to modulate the HCG resonance by gating graphene. However, due to the low mobility of the ionic charger inside ion-gel, modulation speed for ion-gel based device is very difficult to be above MHz. To show the high speed operation of such modulator, we employ the dual-layer graphene structure, in which two layers of graphene are separated by Al₂O₃ grown by ALD. Both electron and holes are injected into graphene layers to form a p-oxide-n like junction. The device will benefit from the linear band dispersion of graphene, which gives a symmetrical DOS near the Dirac point. Because the interband transition coefficient in graphene is only determined by the fermi level, both graphene layers can become transparent simultaneously at high drive voltage and the device is thus at ‘on’ state. Schematic of such structure is shown below.

Now we do an estimation of the modulation speed and energy basing on the data we have. In a HCG graphene modulator we can achieve: $A = 25\mu\text{m}^2$ (assuming that the lithographically defined graphene covers $5\mu\text{m} \times 5\mu\text{m}$), alumina thickness $d = 5\text{ nm}$, dielectric constant of alumina is 10, and the carrier density in graphene required to do such modulation is $10^{17}/\text{m}^2$, then the capacitance of the device becomes $C_T \sim 400\text{fF}$. Such a low capacitance is the key for low energy and high speed operations. For high-frequency operations, the parasitic capacitance of the metal wire on the alumina on silicon will limit the performance. To circumvent that, one needs to dope the silicon selectively and reduce the overlap between graphene and doped silicon only to the cavity region. With a device capacitance of 400fF, the energy of the modulator is around 200 fJ. The speed of the device will be limited by the RC constant of the device. The resistance of the device will come

mostly from the graphene resistance, assuming the silicon is highly doped, and is of very low resistance. Again, one needs to bring the electrodes closer to the cavity to reduce the resistance. In our device, the graphene resistance is around 500Ω (including the contact resistance), leading to a device speed of $\sim 1\text{GHz}$. However, the dc conductivity of graphene in strongly doped region, as used in the modulator condition, can be quite high. People have shown a sheet resistivity of $30 \Omega/\text{sq}$. Assuming the length and width of the graphene electrode are $\sim 1\mu\text{m}$, we find that the resistance of the device can be as low as 30Ω , and the speed of the modulator can be over 10GHz .

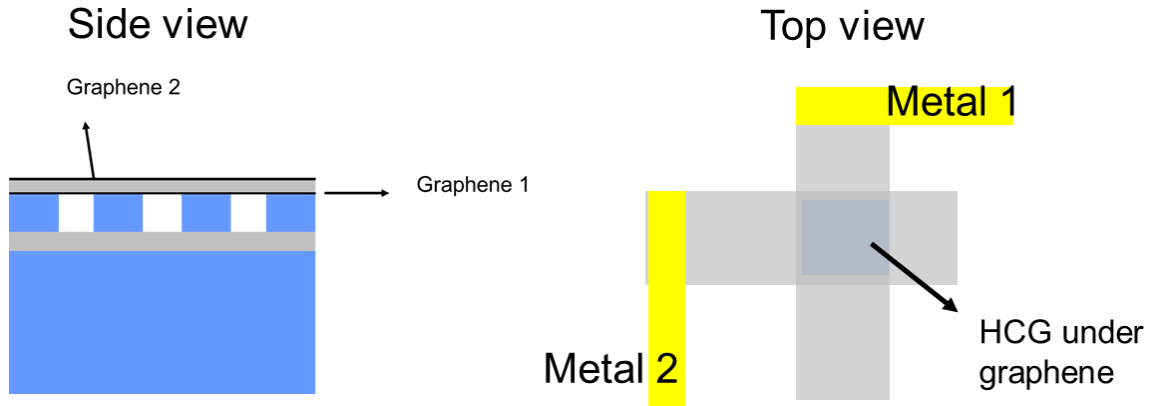


Figure 5. 27 Side view and top view of dual layer graphene HCG spatial light modulator.

5.2.6 Conclusion

In summary, we propose a novel spatial light modulator structure with graphene integrated with HCG resonator. A 12 dB modulation depth is achieved within 2V operation voltage. Using a cavity we significantly enhance the light-graphene interaction and thus increase the graphene absorption. Theoretical analysis shows that such a graphene-cavity based modulator can be used for very low power ($\sim 200\text{fJ}$) electro-optic spatial modulation maintaining a speed of GHz. We believe that such device will benefit many applications in fast beam scanning and beam shaping for remote sensing.

In addition, as we discussed in the previous section. Resonance wavelength of HCG resonator can be lithography defined (without changing the cavity thickness, namely the grating thickness). Utilizing this, one can build up modulator array covering a broadband of working wavelength. In the figure below, we show the measurement results for a resonator array (fabricated on top one single SOI, with same device thickness, however different period and duty cycle) with a broadband working wavelength (in our case, from 1460nm to 1660nm , for 200nm operation range). Such configuration will potentially overcome the narrow band operation associated with resonators.

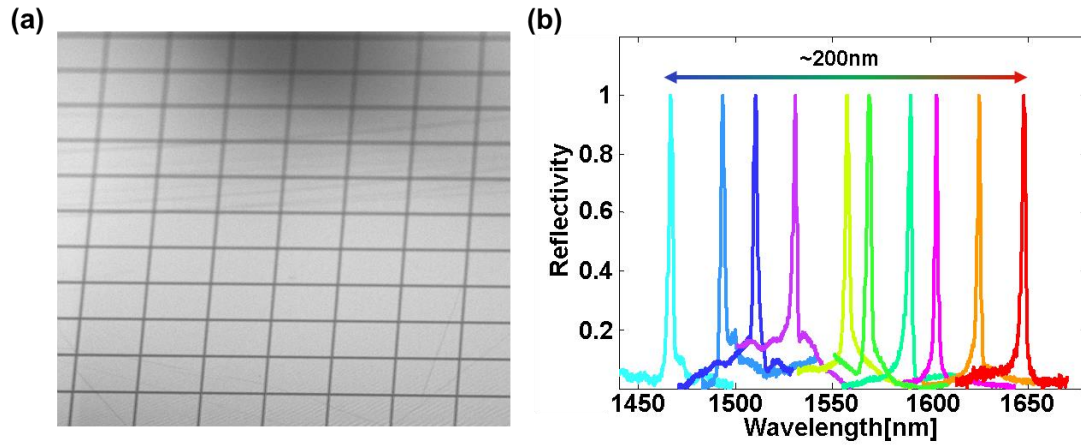


Figure 5. 28 (a) HCG resonator array fabricated on top one single SOI, with same device thickness, however different period and duty cycle. (b) Large working wavelength range, from 1460nm to 1660nm, covering 200nm.

Chapter 6 Summary and Outlook

In this dissertation, the properties of HCG are discussed, especially two extraordinary ones: broadband reflection and high Q optical resonance. Various optical sensing devices based on these two properties are designed, fabricated and characterized.

Physics behind HCG broadband reflection and high Q resonance are explored. Analytical solution is given based on array waveguide modes analysis: HCG is modeled into input plane, exit plane and a set of array waveguide modes in between. Waveguide array modes are used as the mode basis to expand the electromagnetic field inside the HCG, which represents the key difference of this analysis from the other approaches. Reflection matrix for the waveguide array modes is then developed for the two boundaries. The waveguide array modes interfere at the input and exit plane, giving rise to the various properties. The solution of HCG is very similar to that of a FP cavity, however it is in a matrix format, and uses the array waveguide modes as basis.

HCG slow light hollow waveguide explores the high reflectivity and reflection phase dispersion. A slow light hollow waveguide with HCG as the four side wall reflector is designed, fabricated and characterized. Low-loss propagation and slowing down effect are observed in the measurement. Application for compact gas sensor is proposed and analyzed. Three unique features of HCG slow light hollow waveguide gas sensor are worth emphasizing here: first, hollow core for light propagation enhances the light gas interaction, thus increases the sensitivity. Second, slow light effectively increases the time of light travelling inside the waveguide and dramatically reduces the required length for absorptive gas sensor. Third, unique grating structure allows fast gas flowing rate and reduces the detection speed by orders of magnitude.

A label-free optical biosensor is described that employs an HCG resonator with a spectral linewidth of $\sim 500\text{pm}$ that is sensitive to ligand-induced changes in surface properties. The device is used to generate thermodynamic and kinetic data on surface-attached antibodies with their respective antigens. The device can detect serum cardiac troponin I, a biomarker of cardiac disease to 100pg/ml within 4-minutes, which is much faster than and as sensitive as current enzyme-linked immuno-assays for cTnI. Approach to construct flexible biosensor using HCG assisted SPP is also discussed. Whole structure is transferred onto a PDMS substrate, paving the road towards wearable healthcare device in point of care.

High speed optical phased array and tunable detector both uses the HCG as an electrostatically actuated top mirror of a FP cavity. Due to its light weight and ultra-small thickness, the MEMS can have a very high operation speed. All-pass filter is used to construct the phase tuner, which shows a very high phase tuning efficiency. Fast optical beam steering (0.53 MHz) is demonstrated with an 8×8 optical phased array. This fast beam steering or beam forming is particularly promising for remote sensing and fast biological imaging. High filling factor, high NA and high efficiency HCG lens array is proposed and simulated to improve the filling factor of HCG all pass filter array. To achieve low-power high speed (GHz) spatial light modulator, structure with graphene integrated with HCG

resonator is explored. 12dB modulation depth is achieved with 2V operation voltage. Theoretical analysis predict 200fJ power consumption and ~10GHz operation speed.

So far, only one dimensional grating is analyzed. Using the same principle, it is possible to develop the analysis for two dimensional gratings. With another degree of freedom, there will be for sure new properties and opportunity for applications, such as polarization independent beam forming, etc will be enabled.

Theoretical analysis shows that many important HCG features (i.e. broadband high reflectivity and high Q resonance) still remain when the index contrast falls to only 1.5:1 ~ 2:1 [10]. These findings will enable many device innovation on material systems, such as silicon oxide or silicon nitride, where grating contrast is between nitride/oxide and air. This may expand the device working range covering from UV all the way to THz.

Since its invention in 2004, HCG has been actively studied both in theory and experiments. More and more novel devices have been developed with HCG as the enabling components. It is expected that HCG offers a new path for device innovation and form a platform of integrated optoelectronics for optical sensing and many other functionality.

References

- [1] E. G. Loewen, E. Popov, *Diffraction Gratings and Applications*, CRC Press, 1997.
- [2] B. C. Kress, P. Meyrueis, *Applied Digital Optics: from Micro-optics to Nanophotonics*, Wiley, 2009.
- [3] M. Born, E. Wolf, *Principles of Optics*, Cambridge University Press, 1999.
- [4] B-W. Yoo, M. Megans, T. Chan, T. Sun, W. Yang, C. J. Chang-Hasnain, D. A. Horsley, and M. C. Wu, "Optical phased array using high contrast gratings for two dimensional beamforming and beamsteering," *Optics Express*, vol. 21, pp. 12238-12248, 2013.
- [5] C. Chase, Y. Rao, W. Hofmann, and C. J. Chang-Hasnain, "1550 nm high contrast grating VCSELs," *Optics Express*, vol. 18, pp. 15461-15466, 2010.
- [6] C. Chase, Y. Zhou, C.J. Chang-Hasnain, "Size effect of high contrast gratings in VCSELs," *Optics Express*, vol. 17, pp. 24002-24007, 2009.
- [7] C. F. R. Mateus, M. C. Y. Huang, L. Chen, and C. J. Chang-Hasnain and Y. Suzuki, "Broadband mirror (1.12-1.62 μm) using single-layer sub-wavelength grating," *IEEE Photonics Technology Letters*, vol. 16, no. 2004, pp. 1676-1678, 2004.
- [8] C. F. R. Mateus, M. C. Y. Huang, Y. Deng, A. R. Neureuther, and C. J. Chang-Hasnain, "Ultra-broadband mirror using low index cladded subwavelength grating," *IEEE Photonics Technology Letters*, vol. 16, pp. 518-520, 2004.
- [9] C. J. Chang-Hasnain, Y. Zhou, M. C. Y. Huang, and C. Chase, "High-contrast grating VCSELs," *Selected Topics in Quantum Electronics, IEEE Journal of*, vol. 15, pp. 869-878, 2009.
- [10] Connie Chang-Hasnain, Weijian Yang, "High-contrast gratings for integrated optoelectronics," *Advances in Optics and Photonics*, vol. 4, no. 3, pp. 379-440, 2012.
- [11] D. Fattal, J. Li, Z. Peng, M. Fiorentino, and R. G. Beausolei, "Flat dielectric grating reflectors with focusing abilities," *Nature Photonics*, vol. 4, pp. 466-469, 2010.
- [12] F. Lu, F.G. Sedgwick, V. Karagodsky, C. Chase and C.J. Chang-Hasnain, "Planar high-numerical-aperture low-loss focusing reflectors and lenses using subwavelength high contrast gratings," *Optics Express*, vol. 18, pp. 12606-12614, 2010.

- [13] M. C. Y. Huang, Y. Zhou, and C. J. Chang-Hasnain, "A surface-emitting laser incorporating a high index-contrast subwavelength grating," *Nature Photonics*, vol. 1, pp. 119-122, 2007.
- [14] M. C. Y. Huang, Y. Zhou, and C. J. Chang-Hasnain, "A nanoelectromechanical tunable laser," *Nature Photonics*, vol. 2, pp. 180-184, 2008.
- [15] V. Karagodsky, B. Pesala, F. G. Sedgwick, and C. J. Chang-Hasnain, "Dispersion properties of high-contrast grating hollow-core waveguides," *Optics Letters*, vol. 35, pp. 4099-4101, 2010.
- [16] V. Karagodsky, C. Chase, and C. J. Chang-Hasnain, "Matrix Fabry-Perot resonance mechanism in high-contrast gratings," *Optics Letters*, vol. 36, pp. 1704-1706, 2011.
- [17] V. Karagodsky, F.G. Sedgwick and C.J. Chang-Hasnain, "Theoretical analysis of subwavelength high contrast grating reflectors," *Optics Express*, vol. 18, p. 16973, 2010.
- [18] V. Karagodsky, and C. J. Chang-Hasnain, "Physics of near-wavelength high contrast gratings," *Optics Express*, vol. 20, pp. 10888-10895, 2012.
- [19] "V. Karagodsky, B. Pesala, C. Chase, W. Hofmann, F. Koyama and C.J. Chang-Hasnain," *Monolithically integrated multi-wavelength VCSEL arrays using high high contrast*, vol. 18, pp. 694-699, 2010.
- [20] T. Sun, W. Yang, and C. J. Chang-Hasnain, "Surface-normal coupled four-wave mixing in a high contrast gratings resonator," *Optics Express*, vol. 23, pp. 29565-29572, 2015.
- [21] W. Hofmann, C. Chase, M. Müller, Y. Rao, C. Grasse, G. Böhm, M.-C. Amann, and Connie Chang-Hasnain, "Long-Wavelength High-Contrast Grating Vertical-Cavity Surface-Emitting Laser," *IEEE Photonics Journal*, vol. 2, pp. 415-422, 2010.
- [22] W. Yang, J. Ferrara, K. Grutter, A. Yeh, C. Chase, Y. Yue, A. E. Willner, M. Wu, and C. J. Chang-Hasnain, "Low loss hollow-core waveguide on a silicon substrate," *Nanophotonics*, vol. 1, pp. 23-29, 2012.
- [23] Y. Rao, W. Yang, C. Chase, M. C. Y. Huang, D. P. Worland, S. Khaleghi, M. R. Chitgarha, M. Ziyadi, A. E. Willner, and C. J. Chang-Hasnain, "Long-Wavelength VCSEL Using High Contrast Grating," *Selected Topics in Quantum Electronics, IEEE Journal of*, vol. 19, p. 1701213, 2013.
- [24] Y. Zhou, M. C. Y. Huang, and C. J. Chang-Hasnain, "Large fabrication tolerance for VCSELs using high contrast grating," *IEEE Photonics Technology Letters*, vol. 20, pp. 434-436, 2008.
- [25] Y. Zhou, M. Moewe, J. Kern, M. C. Huang, and C. J. Chang-Hasnain, "Surface-normal emission of a high-Q resonator using a subwavelength high-contrast grating," *Optics Express*, vol. 16, pp. 17282-17287, 2008.
- [26] Y. Zhou, V. Karagodsky, B. Pesala, F.G. Sedgwick and C.J. Chang-Hasnain, "A novel ultra-low loss hollow-core waveguide using subwavelength high-contrast gratings," *Optics Express*, vol. 17, pp. 1508-1517, 2009.

- [27] G. C. Righini, etc, An Introduction to Optoelectronic Sensors, World Scientific Publishing Co., 2009.
- [28] B. Temelkuran, S. D. Hart, G. Benoit, J. D. Joannopoulos, Y. Fink, "Wavelength-scalable hollow optical fiber with large photonic bandgaps for CO₂ laser transmission," *Nature*, vol. 3, pp. 420-650, 2002.
- [29] F. Benabid, J. C. Knight, G. Antonopoulos, and P. St. J. Russell, "Stimulated Raman scattering in hydrogen-filled hollow-core photonic crystal fiber," *Science*, vol. 298, pp. 399-402, 2002.
- [30] Y. Hamachi, S. Kubo and T. Baba, "Slow light with low dispersion and nonlinear enhancement in a lattice-shifted photonic crystal waveguide," *Optics Letter*, vol. 34, pp. 1072-1074, 2009.
- [31] J. Gregic, S. Xiao, J. Mork, A. Jauho and N. A. Mortensen, "Slow-light enhanced absorption in a hollow-core fiber," *Optics Express*, vol. 18, pp. 14270-14279, 2010.
- [32] W. Lai, S. Chakravarty, X. Wang, C. Lin and R. T. Chen, "On-chip methane sensing by near-IR absorption signatures in a photonic crystal slot waveguide," *Optics Letter*, vol. 36, pp. 984-986, 2011.
- [33] D. K. C. Wu, B. T. Kuhlmeier and B. J. Eggleton, "Ultrasensitive photonic crystal fiber refractive index sensor," *Optics Letter*, vol. 34, pp. 322-324, 2009.
- [34] H. Schmidt, D. Yin, J. P. Barber and A. Hawkins, "Hollow-Core Waveguide and 2-D Waveguide Arrays for Integrated Optics of Gases and Liquids," *selected topics of Quantum Electronics, IEEE journal of*, vol. 11, pp. 519-527, 2005.
- [35] J. A. Harrington, "A Review of IR Transmitting, Hollow Waveguides," *Fiber and Integrated Optics*, vol. 3, p. 19, 2000.
- [36] E. A. J. Marcatili and R. A. Schmeltzer, "Hollow Metallic and Dielectric Waveguides for Long Distance Optical Transmission and Lasers," *Bell system technology journal*, vol. 43, pp. 1783-1809, 1964.
- [37] J. N. McMullin, R. Narendra, C. R. James, "Hollow metallic waveguides in silicon V-grooves," *IEEE photonic technology letter*, vol. 5, p. 1080, 1993.
- [38] T. Miura, F. Koyama, Y. Aoki, A. Matsutani and Kenichi Iga, "Hollow Optical Waveguide for Temperature-Insensitive Photonic Integrated Circuits," *Japanese Journal of Applied Physics*, vol. 7A, p. 40, 2001.
- [39] Y. Sakurai and F. Koyama, "Control of group delay and chromatic dispersion in tunable hollow waveguide with highly reflective mirrors," *Japanese Journal of Applied Physics*, vol. 43, pp. 1091-1093, 2004.
- [40] P. J. Roberts, F. Couny, H. Sabert, B. J. Mangan, D. P. Williams, L. Farr, M. W. Mason, A. Tomlinson, T. A. Birks, J. C. Knight and P. St.J. Russell, "Ultimate low loss of hollow-core photonic crystal fibres," *Optics Express*, vol. 13, pp. 236-244, 2005.
- [41] T. Baba, "Slow light in photonic crystal," *Nature Photonics*, vol. 2, pp. 465-473, 2008.

- [42] R. W. Boyd, D. J. Gauthier, A. L. Gaeta and A. E. Willner, "Maximum time delay achievable on propagation through a slow-light medium," *Physical Review A*, vol. 71, p. 023801, 2005.
- [43] W. Zhou, etc. "Demonstration of a slow-light high contrast metastructure cage waveguide," Proc. SPIE 863, High Contrast Metastructure II, 863305 (15 March 2013)
- [44] J. Wang, etc, "Electrochemical biosensors: towards point-of-care cancer diagnostics," *Biosensors and Bioelectron*, vol. 21, pp. 1887-92, 2006.
- [45] E. Thrush, etc, "Monolithically integrated semiconductor fluorescence sensor for microfluidic applications," *Sensor and Actuator B: Chemical*, vol. 105, pp. 393-399, 2005.
- [46] A. F. Coskun, etc., "Lensfree optofluidic plasmonic sensor for real-time and label-free monitoring of molecular binding events over a wide field of view," *Scientific Review*, vol. 4, p. 6789, 2014.
- [47] Y. Cui, etc, "Nanowire biosensor for highly sensitive and selective detection of biological and chemical species," *Science*, vol. 293, pp. 1289-92, 2001.
- [48] B. Fan, etc, "Integrated refractive index sensor based on hybrid coupler with short range surface plasmon polariton and dielectric waveguide," *Sensor and Actuator B: Chemical*, vol. 186, pp. 495-505, 2013.
- [49] S. Kita, etc, "Refractive index sensing utilizing a cw photonic crystal nanolaser and its array configuration," *Optics Express*, vol. 16, pp. 8174-8180, 2008.
- [50] H. Shaflee, etc, "Nanostructured optical photonic crystal biosensor for HIV viral load measurement," *Scientific Reports*, vol. 4, p. 4116, 2014.
- [51] F. Vollmer, and S. Arnold, "Whispering-gallery-mode biosensing: label free detection down to single molecules," *Nature Methods*, vol. 5, p. 591, 2008.
- [52] T.Y. Chang, etc, "Large-scale plasmonic microarrays for label-free high-throughput screening," *Lab on Chip*, vol. 11, pp. 3596-602, 2011.
- [53] P. Von Lode, etc., "Point-of-care immunotesting: approaching the analytical performance of central laboratory methods," *Clinical Biochemistry*, vol. 38, pp. 591-606, 2005.
- [54] K. Wang, etc, "The complex Exogenous RNA Spectra in Human Plasma: An Interface with Human Gut Biota?," *Plos One*, vol. 7, p. 51009, 2012.
- [55] T. Reichlin, etc, "Early Diagnosis of Myocardial Infarction with Sensitive Cardiac Troponin Assay," *New England Journal of Medicine*, vol. 361, pp. 858-867, 2009.
- [56] A. L. Straface, etc, "A rapid point-of-care cardiac marker testing strategy facilitates the rapid diagnosis and management of chest pain patients in the emergency department," *American journal of Clinical Pathology*, vol. 129, pp. 788-95, 2008.
- [57] S.-S. Antonio and M. Girvent, "Catheter-related bloodstream infections," *World journal of surgery*, vol. 23, no. 6, pp. 589-595, 1999.
- [58] D. Klonidis, C. T. Politi, R. Nejaabati, M. J. O'Mahony, and D. Simeonidou, "OPSnet: design and demonstration of an asynchronous high-speed optical

- packet switch," *Journal of Lightwave Technology*, vol. 23, pp. 2914-2925, 2005.
- [59] J. Ma, and C. Jiang, "Design and analysis of all-optical switches based on fiber parametric devices," *Optics Communication*, vol. 281, pp. 2605-2613, 2008.
- [60] K. Kawase, J. Shikata, K. Imai, and H. Ito, "Transform-limited, narrow-linewidth, terahertz-wave parametric generator," *Applied Physics Letter*, vol. 78, pp. 2819-2821, 2001.
- [61] K. J. Vahala, "Optical microcavities," *Nature*, vol. 424, pp. 839-846, 2003.
- [62] R. Salem, M. A. Foster, A. C. Turner, D. F. Geraghty, M. Lipson, and A. L. Gaeta, "Signal regeneration using low-power four-wave mixing on silicon chip," *Nature Photonics*, vol. 2, pp. 35-38, 2008.
- [63] H. Fukuda, K. Yamada, T. Shoji, M. Takahashi, T. Tsuchizawa, T. Watanabe, J. Takahashi, and S. Itabashi, "Four-wave mixing in silicon wire waveguides," *Optics Express*, vol. 13, pp. 4269-4637, 2005.
- [64] R. Espinola, J. Dadap, R. Osgood, S. McNab, and Y. Vlasov, "C-band wavelength conversion in silicon photonic wire waveguides," *Optics Express*, vol. 13, pp. 4341-4329, 2005.
- [65] M. A. Foster, A. C. Turner, J. E. Sharping, B. S. Schmidt, M. Lipson, and A. L. Gaeta, "Broad-band optical parametric gain on a silicon photonic chip," *Nature*, vol. 441, pp. 960-963, 2006.
- [66] M. Shinkawa, N. Ishikura, Y. Hama, K. Suzuki, and T. Baba, "Nonlinear enhancement in photonic crystal slow light waveguides fabricated using CMOS compatible process," *Optics Express*, vol. 19, pp. 22208-22218, 2011.
- [67] C. Monat, M. Ebnali-Heidari, C. Grillet, B. Corcoran, B. J. Eggleton, T. P. White, L. O'Faolain, J. Li and T. F. Krauss, "Four-wave mixing in slow light engineered silicon photonic crystal waveguides," *Optics Express*, vol. 18, pp. 22915-22927, 2010.
- [68] J. Li, L. O'Faolain, I. H. Rey and T. F. Krauss, "Four-wave mixing in photonic crystal waveguides: slow light enhancement and limitations," *Optics Express*, vol. 19, pp. 4458-4463, 2011.
- [69] D. Taillaert, F. Van Laere, M. Ayre, W. Bogaerts, D. Van Thourhout, P. Bienstman and R. Baets, "Grating couplers for coupling between optical fibers and nanophotonic waveguides," *Japanese Journal of Applied Physics*, vol. 45, pp. 6071-6077, 2006.
- [70] O. Mitomi, K. Kasaya and H. Miyazawa, "Design of a single-mode tapered waveguide for low-loss chip-to-fiber coupling," *Journal of Quantum Electron*, vol. 30, pp. 1787-1793, 1994.
- [71] T. Gu, N. Petrone, J. F. McMillan, A. Van Der Zande, M. Yu, G. Q. Lo, D. L. Kwong, J. Hone and C. W. Wong, "Regenerative oscillation and four-wave mixing in graphene optoelectronics," *Nature Photonics*, vol. 6, pp. 554-559, 2012.

- [72] S.L. Portalupi, M. Galli, C. Reardon, T. F. Krauss, L. O'Faolain, L. C. Andreani, and D. Gerace, "Planer photonic crystal cavities with far-field optimization for high coupling efficiency and quality factor," *Optics Express*, vol. 18, pp. 16064-16073, 2010.
- [73] M. Ferrera, D. Duchesne, L. Razzari, M. Peccianti, R. Morandotti, P. Cheben, S. Janz, D. -X. Xu, B. E. Little, S. Chu and D. J. Moss, "Low power four wave mixing in an integrated micro-ring resonator with $Q = 1.2$ million," *Optics Express*, vol. 17, pp. 14098-14103, 2009.
- [74] U. Krishnamoorthy, K. Li, K. Yu, D. Lee, J. P. Heritage, and O. Solgaard, "Dual-mode micromirrors for optical phased array applications," *Sensors and Actuators A*, vol. 21, pp. 97-98, 2002.
- [75] P. F. Van Kessel, L. J. Hornbeck, R. E. Meier, and M. R. Douglass, "A MEMS-based projection display," *Proceedings of the IEEE*, vol. 86, pp. 1687-1704, 1998.
- [76] P. F. McManamon, T. A. Dorschner, D. L. Corkum, L. J. Friedman, D. S. Hobbs, M. Holz, S. Liberman, H. Q. Nguyen, D. P. Resler, R. C. Sharp, and E. A. Watson, "Optical phased array technology," *Proceedings of the IEEE*, vol. 84, pp. 268-298, 1996.
- [77] J. K. Doylend, M. J. R. Heck, J. T. Bovington, J. D. Peters, L. A. Coldren, and J. E. Bowers, "Two-dimensional free-space beam steering with an optical phased array on silicon-on-insulator," *Optics Express*, vol. 19, pp. 21595-21604, 2011.
- [78] J. Sun, E. Timurdogan, A. Yaacobi, E. S. Hosseini, and M. R. Watts, "Large-scale nanophotonic phased array," *Nature*, vol. 493, pp. 195-199, 2013.
- [79] B. Wang, G. Zhang, A. Glushchenko, J. L. West, P. J. Bos, and P. F. McManamon, "Stressed liquid-crystal optical phased array for fast tip-tilt waveform correction," *Applied Optics*, vol. 44, pp. 7754-7759, 2005.
- [80] D. Engstrom, M. J. O'Callaghan, C. Walker, and M. A. Handschy, "Fast beam steering with a ferroelectric-liquid-crystal optical phased array," *Applied Optics*, vol. 48, pp. 1721-1726, 2009.
- [81] K. Goossen, J. Walker, and S. Arney, "Silicon modulator based on mechanically-active anti-reflection layer with 1 Mbit/sec capability for fiber-in-the-loop applications," *IEEE Photonic Technology Letter*, vol. 6, pp. 1119-1121, 1994.
- [82] C. Madsen and G. Lenz, "Optical all-pass filters for phase response design with applications for dispersion compensation," *IEEE Photonic Technology Letter*, vol. 17, pp. 994-996, 1998.
- [83] G. Lenz and C. K. Madsen, "General optical all-pass filter structures for dispersion control in WDM systems," *Journal of Lightwave Technology*, vol. 17, pp. 1248-1254, 1999.
- [84] C. K. Madsen, J. A. Walker, J. E. Ford, K. W. Goossen, T. N. Nielsen, and G. Lenz, "A tunable dispersion compensating MEMS all-pass filter," *Photonic Technology Letter*, vol. 12, pp. 651-653, 2000.

- [85] N.C. Singer, W.P. Seering, "Preshaping command inputs to reduce system vibration," *ASME Journal of Dynamic System, Measurement, and Control*, vol. 112, pp. 76-82, 1990.
- [86] J. Vaughan, A. Yano and W. Singhose, "Robust negative input shapers for vibration suppression," *ASME Journal of Dynamic System, Measurement, and Control*, vol. 131, p. 031014, 2009.
- [87] T. K. Chan, M. Megens, B.-W. Yoo, J. Wyras, C. J. Chang-Hasnain, M. C. Wu, and D. A. Horsley, "Optical beamsteering using an 8×8 MEMS phased array with closed-loop interferometric phase control," *Optics Express*, vol. 21, pp. 2807-2815, 2013.
- [88] S. Boutami, B. B. Bakir, H. Hattori, X. Letartre, J. -L. Leclercq, P. Rojo-Romeo, M. Garrigues, C. Seassal, and P. Viktorovitch, "Broadband and compact 2-D photonic crystal reflectors with controllable polarization dependence," *IEEE Photonic Technology Letter*, vol. 18, pp. 835-837, 2006.
- [89] H. Yang, D. Zhao, J.-H. Seo, S. Chuwongin, S. Kim, J. A. Rogers, Z. Ma, and W. Zhou, "Broadband membrane reflectors on glass," *IEEE Photonic Technology Letter*, vol. 24, pp. 476-478, 2012.
- [90] M. Liu, etc, "A graphene-based broadband optical modulator," *Nature*, vol. 474, pp. 64-67, 2011.
- [91] M. Liu, etc, "Double-Layer Graphene Optical Modulator," *Nano Letters*, vol. 12, pp. 1482-1485, 2012.
- [92] A. Majumdar, etc., "Electrical Control of Silicon Photonic Crystal Cavity by Graphene," *Nano Letters*, vol. 13, pp. 515-518, 2012.